

**LOADING POLYMER COATED MAGNETITE NANOPARTICLES ON NYLON 6  
NANOMEMBRANES BY THREE METHODS**

A Thesis

Presented to the Faculty of the Graduate School

of Cornell University

in Partial Fulfillment of the Requirements for the Degree of

Master of Science

by

Nidia Kimberly Trejo

January 2015

© 2015 Nidia Kimberly Trejo

## ABSTRACT

In this study carboxylic acid coated magnetite nanoparticles (CA-Fe<sub>3</sub>O<sub>4</sub> NPs) were applied to mechanically robust, Nylon 6 nanomembranes by three different techniques; 1) simultaneous electrospraying-electrospinning, 2) layer-by-layer (LbL) assembly, and 3) chemical grafting of NPs onto Nylon 6. The aim of this study was to evaluate the NP treatment homogeneity by the three methods and examine the durability on the membranes for potential wastewater treatment applications. The carboxylic acid polymeric coating on the NPs facilitated loading by all methods to display differing chemical bonding pathways: hydrogen bonding, ionic bonding, and covalent bonding. Electrospinning the fibers while simultaneously electrospraying is a simple method to incorporate NPs within fibers independent of polymer-particle solvent compatibilities. LbL assembly can allow for the number of NP layers to be controlled. The grafting method can allow for the formation of a durable, covalent bond between the carboxylate groups of the NPs and amine end groups on Nylon 6. Main characterization techniques included electron microscopy, CIELAB spectrophotometry, and ICP-AES analysis. Results reveal that electrospinning-electrospraying and chemical grafting methods produced a homogeneous NP dispersion on the membranes. ICP-AES results indicate that the durability of the treatments is pH dependent and driven by electrostatic interactions. These surface treatment methods have not been previously attempted with Nylon 6 fibers and polymer coated Fe<sub>3</sub>O<sub>4</sub> NPs. Additionally, few studies evaluate the durability of NP treatments on fibers although it is an issue of high concern and the NP treatment should be long lasting for the intended end-use.

## **BIOGRAPHICAL SKETCH**

Nidia Kimberly Trejo was born in Los Angeles, CA May of 1990 with a twin sister. Her parents, Rene and Milagro Trejo, both migrated to L.A. as teenagers in the mid-1980s from El Salvador to flee civil unrest from guerrilla warfare and unite with their families in the United States. Currently, her father is a self-employed tile setter. Her mother is a Medicaid eligibility worker for Los Angeles County. Her parents instilled the value of education at a young age. Nidia observed her mother work full-time and attend school part-time to earn a Bachelor's Degree in Public Administration from California State University, Dominguez Hills. Prior to entering college, Nidia attended seven primary schools as her parents sought to get her into schools with other intellectually motivated students in Los Angeles.

She graduated from Downtown Magnets High School in 2008 and entered the University of California, Davis (UCD) to pursue undergraduate studies. Along the way she participated in college preparatory programs including University of Southern California's SummerTIME writing program and UCD's Ronald E. McNair Post-Baccalaureate Achievement Program. From UCD she received a Bachelor of Arts in Design with an emphasis in fashion design and a Bachelor of Science in Textiles & Clothing with an emphasis in textile science. Nidia originally dreamt of being a fashion designer, however, she became fascinated with textile chemistry at UCD. She was further encouraged to pursue graduate studies in textile chemistry by her undergraduate research mentor, Dr. Gang Sun. In 2012 Nidia received the UCD Cal Aggie Alumni Association Outstanding Senior Award in special recognition from the Department of Textiles & Clothing for her research contributions and high GPA. In August 2012 she began her Master's research and will continue for doctoral studies at Cornell University in Fiber Science.

## ACKNOWLEDGEMENTS

Dr. Margaret Frey in the Department of Fiber Science & Apparel Design was very encouraging and helped me improve my experimental protocols throughout my Master's project. Dr. Lara Estroff from the Department of Material Science & Engineering served on my graduate committee and provided thoughtful guidance. A research associate in my group, Stephane Corgie, and group member, Catherine Reyes, helped me grow as a researcher in every aspect. I would also like to thank Xia Zeng, the lab manager, in the Department of Fiber Science & Apparel Design who trained me on analytical instrumentation within the department.

This work made use of the Cornell Center for Materials Research Shared Facilities, which are supported through the NSF MRSEC program (DMR-1120296). I am grateful for the help I received from John Hunt, John Grazul, and Malcolm Thomas. From these lab technicians I learned more about analytical methods and improved my instrumentation techniques in the Cornell Center for Materials Research (CCMR).

Additional facilities I would like to acknowledge are the Nanobiotechnology Center (NBTC) and the Cornell Nutrient Analysis Laboratory (CNAL).

Throughout my Master's thesis my twin sister, Helen, and my parents gave me their unconditional support and motivation. Other ethnic minorities who are also graduate students at Cornell provided moral support during my thesis project. They are members of the Black Graduate and Professional Student Association (BGPSA), Society for Asian American Graduate Affairs (SAAGA), the Latino Graduate Student Coalition (LGSC), and the Indigenous Graduate Student Association (IGSA).

## TABLE OF CONTENTS

BIOGRAPHICAL SKETCH.....	iii
ACKNOWLEDGEMENTS.....	iv
LIST OF FIGURES.....	v
LIST OF TABLES AND EQUATIONS.....	vii
LIST OF ABBREVIATIONS AND SYMBOLS.....	viii
PREFACE.....	xii
CHAPTER	
1. LITERATURE REVIEW	
Electrospinning	
Historical Overview.....	1
Nanofiber Production Techniques.....	1
Description of Electrospinning Process.....	2
Parameters that Effect Electrospinning of Nanofibers.....	2
Review of Composite Nanofibers.....	4
Review on Methods for Nanoparticle Incorporation	
Electrospraying.....	6
Layer-by-Layer Assembly.....	8
Chemical Grafting Reaction.....	10
Evaluating NP Treatment Durability.....	15
Polymer Coated Iron Oxide Nanoparticles	
Water Treatment Property.....	16
Magnetic Property.....	17
Basic Characterization Techniques	
Scanning Electron Microscopy.....	19
Transmission Electron Microscopy.....	20
2. EXPERIMENTAL PROCEDURE	
Materials.....	23
Electrospinning Conditions.....	23
Buffer Solution Preparation.....	25
Electrospraying Conditions.....	26
Layer-by-Layer Assembly Conditions.....	28
Chemical Grafting Conditions.....	28
Direct Addition of Nanoparticles to Spinning Dope.....	30
Washing Protocol.....	30
Characterization	
Polymer Solution Viscosity.....	31
Surface Tension Measurements.....	32
Scanning Electron Microscopy (SEM).....	32
Field Emission Scanning Electron Microscopy (FESEM).....	32
Transmission Electron Microscopy (TEM).....	33
Fourier Transform Infrared Spectroscopy (FTIR).....	33
Thermogravimetric Analysis (TGA/DTG).....	34
CIELAB Color System.....	34
Zeta Potential.....	35

UV-Vis Spectrometry.....	35
3. RESULTS & DISCUSSION	
Optimization of Upscaled Electrospinning Set-Up.....	36
Electrospinning Pristine Nanofibers	
Fiber Morphology.....	38
Nanoparticle Characterization	
Nanoparticle Morphology.....	41
EDX Analysis.....	42
FTIR Analysis.....	43
TGA/DTG Analysis.....	44
Initial characterization - Electrospayed NPs on Fibers	
Optimization of Electro Spray System.....	45
Initial characterization - LbL Assembly of NPs on Fibers	
Zeta Potential.....	48
UV-Vis Results.....	49
Initial Characterization - Chemical Grafting of Nanoparticles on Fibers	
FTIR Results.....	51
CIELAB Control Studies	
Nanoparticle Physical Adsorption Control Studies.....	52
Comparative Results From Three Methods	
Fiber Morphology	
Electrospray Method.....	53
Layer-by-Layer Assembly.....	55
Chemical Grafting Reaction.....	55
CIELAB Results	
Electrospray, LbL, Grafting Methods.....	56
Post-Washing Results via ICP-AES Evaluation	
Electrospray Method.....	58
Layer-by-Layer Method.....	59
Chemical Grafting Method.....	60
Post-Washing Results via FESEM Image Evaluation	
Electrospray Method.....	61
Layer-by-Layer Method.....	62
Chemical Grafting Method.....	63
Post-Washing Results via CIELAB evaluation	
Electrospray, LbL, Grafting Methods.....	64
TGA/DTG results.....	67
4. CONCLUSIONS.....	70
5. FUTURE WORK	
Examine Magnetic Properties of CA-Fe <sub>3</sub> O <sub>4</sub> Treated Membranes.....	71
Confirm Covalent Bonding in Chemical Grafting Reaction.....	71
Wastewater Treatment Performance & Potential Recyclability/Reuse of Composite Nanomembranes.....	72
Green Route to NP Synthesis.....	73
6. REFERENCES.....	75
7. APPENDIX	

Upscaled Electrospinning System – Before and After.....	81
Additional Grafting Reaction Data	
FTIR Data.....	82
XPS Data.....	82
Fiber Morphology.....	84
CIELAB Values for Post-Washed Membranes.....	85
CIELAB Measurement Standards.....	85

## LIST OF FIGURES

Figure 1.1 Basic electrospinning set-up.....	2
Figure 1.2 Overview of composite nanofiber membrane applications.....	5
Figure 1.3 TiO <sub>2</sub> nanoparticles loaded on PVC nanofibers via electrospaying.....	7
Figure 1.4 CCD camera image of TiO <sub>2</sub> nanoparticles spraying toward collector forming a cone jet.....	8
Figure 1.5 Schematic of general layer-by-layer assembly.....	8
Figure 1.6 Proposed amidization mechanism with EDC.....	12
Figure 1.7 High resolution XPS scan of C1s band for a) pristine NY66 film, b) PAA-g-NY66 film, c) hexylamine-g-PAA-g-NY66 film.....	14
Figure 1.8 Adsorption of dyes overtime in a C/C <sub>0</sub> plot and photograph of magnetic separation, modified graphic.....	17
Figure 1.9 Representative hysteresis curves for magnetic materials.....	19
Figure 1.10 Diagram of scanning electron microscope.....	20
Figure 1.11 Diagram of transmission electron microscope, adapted.....	21
Figure 2.1 Arial view of large scale electrospinning set-up. Zoom-in on side view of needle/solution reservoir set-up for electrospinning.....	25
Figure 2.2 Side view of needle/solution reservoir set-up for electrospaying.....	28
Figure 2.3 Amidization of a carboxylic acid with an amine using EDC/sulfo-NHS coupling agents.....	30
Figure 2.4 TEM nanofiber preparation on oyster grid.....	33
Figure 2.5 CIELAB 3D color coordinate system.....	35
Figure 3.1 25 wt% Nylon 6 nanofibers before adjustments 1.....	37
Figure 3.2 25 wt% Nylon 6 nanofibers before adjustments 2.....	37
Figure 3.3 20 wt% pristine Nylon 6 nanofibers at 10 cm T-to-C distance.....	39
Figure 3.4 25 wt% pristine Nylon 6 nanofibers at 15 cm T-to-C distance.....	39
Figure 3.5 Average nanofiber diameters based on varying T-to-C distances.....	40
Figure 3.6 TEM image of CA-Fe <sub>3</sub> O <sub>4</sub> nanoparticles dispersed in DI-H <sub>2</sub> O.....	41
Figure 3.7 Distribution histogram displaying average particle diameter of CA-Fe <sub>3</sub> O <sub>4</sub> NPs.....	42
Figure 3.8 Dark Field image and EDX scan of NPs.....	42
Figure 3.9 ATR-FTIR spectra of CA-Fe <sub>3</sub> O <sub>4</sub> NPs.....	43
Figure 3.10 TGA curve of raw CA-Fe <sub>3</sub> O <sub>4</sub> NPs.....	44
Figure 3.11 DTG curve of raw CA-Fe <sub>3</sub> O <sub>4</sub> NPs.....	45
Figure 3.12 Flow rate trials set at 0.4 ml/min. Solution above the needles for electrospaying.....	46
Figure 3.13 Photograph of homogeneous solvent dispersion on nanomembrane with multi-jet electrospay system.....	46
Figure 3.14 Conductivity of CA-Fe <sub>3</sub> O <sub>4</sub> NPs immersed in varied solvents.....	48
Figure 3.15 Zeta potential of CA-Fe <sub>3</sub> O <sub>4</sub> NPs and 0.8 wt/vol% PEI at various pH ranges.....	49
Figure 3.16 UV-Vis spectra and photograph of NP solutions after each bilayer dip.....	50
Figure 3.17 FTIR of sulfo-NHS and sulfo-NHS activated NPs.....	52
Figure 3.18 TEM image of 5 wt% CA-Fe <sub>3</sub> O <sub>4</sub> NPs sprayed on Nylon 6.....	54
Figure 3.19 Zoomed out TEM image of electrospayed particles on Nylon 6.....	54

Figure 3.20 5 wt% CA-Fe <sub>3</sub> O <sub>4</sub> NPs deposited via LbL assembly on Nylon 6.....	55
Figure 3.21 3 wt% CA-Fe <sub>3</sub> O <sub>4</sub> NPs grafted to Nylon 6 nanofibers.....	56
Figure 3.22 ICP-AES results of Fe released from 5 wt% electrospayed membranes washed in varied pH baths.....	59
Figure 3.23 ICP-AES results of Fe released from layer-by-layer treated membranes washed in varied pH baths.....	60
Figure 3.24 ICP-AES results of Fe released from grafted membranes in varied pH baths.....	61
Figure 3.25 Post-washed electrospayed Nylon 6.....	62
Figure 3.26 Post-washed LbL treated Nylon 6.....	63
Figure 3.27 Post-washed grafted Nylon 6.....	64
Figure 3.28 Electrospayed membranes with highest Fe release before/after washed.....	65
Figure 3.29 LbL membranes with highest Fe release before/after washed.....	66
Figure 3.30 Grafted membranes with highest Fe release before/after washed.....	66
Figure 3.31 DTG graph of pristine Nylon 6 and CA-Fe <sub>3</sub> O <sub>4</sub> NP treated Nylon 6 membranes.....	68
Figure 3.32 TGA curves of pristine Nylon 6 and CA-Fe <sub>3</sub> O <sub>4</sub> NP treated Nylon 6 membranes.....	69
Figure 7.1 Photograph of electrospinning system in Frey lab before adjustments (top) and after (bottom).....	81
Figure 7.2 ATR-FTIR spectra of pristine EDC powder/ester-activated NPs.....	82
Figure 7.3 XPS spectra of nanoparticle drop cast samples.....	83
Figure 7.4 XPS spectra of Nylon 6 nanomembranes treated via the grafting method for extended time.....	84
Figure 7.5 FESEM image of representative fiber morphology/NP distribution by grafting conditions.....	85

## LIST OF TABLES

Table 1.1 Variable electrospinning parameters.....	3
Table 1.2 Experimental conditions for amidization reaction.....	13
Table 1.3 Adapted table of varied molar ratios of EDC and NHS to graft PAA to NY66 films.....	15
Table 2.1 Quantities for 20 and 25 weight % Nylon 6 polymer solution for electrospinning.....	23
Table 2.2 Quantities of nanoparticle solutions for electrospaying.....	26
Table 2.3 CA-Fe <sub>3</sub> O <sub>4</sub> NP dispersion performance.....	27
Table 2.4 Viscosity values of Nylon 6 polymer solutions.....	31
Table 2.5 Surface tensions of polymer solutions.....	32
Table 3.1 Electrospinning conditions along the path to optimization.....	36
Table 3.2 Physical properties of solvents.....	47
Table 3.3 Color coordinates of 20 wt% Nylon 6 dipped in controlled baths for various time intervals.....	53
Table 3.4 Color coordinates of NP treated membranes via electrospaying, LbL, and chemically grafted.....	57
Table 7.1 Color coordinates of post-washed electrospayed, LbL, and grafted membranes.....	85
Table 7.2 CIELAB values of Pantone color cards.....	86

## EQUATIONS

Equation 1.1 Calculation to estimate the fraction of surface covered by PAA.....	14
Equation 2.1 Weight % equation for polymer concentration.....	23

## LIST OF ABBREVIATIONS AND SYMBOLS

Ag	silver
Al	aluminum
Al <sub>2</sub> O <sub>3</sub>	aluminum oxide
A/m	amperes per meter
ATR-FTIR	attenuated total reflectance-fourier transform infrared spectroscopy
Au	gold
Au-Pd	gold-palladium
B <sub>p</sub>	boiling point
°C	degree centigrade
C	carbon
CA- Fe <sub>3</sub> O <sub>4</sub>	carboxylic acid coated iron oxide
CCD camera	charge-coupled device camera
-CH <sub>x</sub>	alkyl groups
CH <sub>3</sub> OH	methanol
CIE	the French International Commission on Illumination
CIELAB or CIE L*a*b*	color space defined by the CIE
cm <sup>(2)</sup>	(square) centimeter
-C=O	carbonyl functional group
-COO <sup>-</sup> or CO <sub>2</sub>	carboxylate ion
-CONH	amide functional group
-COOH	carboxylic acid functional group
CPS	counts per second
CRT	cathode ray tube; vacuum tube holding electron gun(s)
Cu	copper
CuO	copper oxide
C13-NMR	carbon-13 nuclear magnetic resonance
DC	direct current
DI-H <sub>2</sub> O	deionized water
DTG	differential thermal gravimetry
dyne/cm or mN/m	dyne per centimeter; milliNewton per meter; standard unit for surface tension
D65	standard illuminant defined by the CIE
EDC	1-ethyl-3-(3-dimethylaminopropyl)carbodiimide
EDX spectroscopy	energy-dispersive X-ray spectroscopy
EELS spectroscopy	electron energy loss spectroscopy
emu/g	magnetization by mass
eV	electron volt
et al	and others
FA	formic acid
Fe	iron
Fe <sub>3</sub> O <sub>4</sub>	iron oxide
FESEM	field emission scanning electron microscopy
FTIR spectroscopy	fourier transform infrared spectroscopy
g	gram

-g-	grafted to
GO	graphene oxide
H <sub>a</sub>	external magnetic field
H <sub>c</sub>	coercivity; in units of Oe (oersted) or A/m (amperes per meter)
HCl	hydrochloric acid
hr(s)	hour(s)
ICP-AES	inductively coupled plasma atomic emission spectroscopy
ICP-OES	inductively coupled plasma optical emission spectroscopy
<i>in situ</i>	directly in the mixture
IR	infrared
J	intensity of magnetization
J <sub>r</sub>	remnant magnetization
J <sub>s</sub>	saturation magnetization
K	potassium
kDa	kiloDalton or kilogram/mol
keV	kiloelectron volt
KH <sub>2</sub> PO <sub>4</sub>	monopotassium phosphate
kV	kilovolt
LaB <sub>6</sub>	LaB <sub>6</sub> lanthanum hexaboride
LbL	layer-by-layer
mg	milligram
min	minute
mL	milliliter
mm	millimeter, 1 x 10 <sup>-3</sup> m
M	magnetization, in units of emu/g
mM or mmol/L	millimolar of solute per liter of solution
mol	mole, amount of a substance
mV	millivolt
M <sub>w</sub>	molecular weight
N	nitrogen
N	normality, equivalents of solute/liter of solution
NaH <sub>2</sub> PO <sub>4</sub>	sodium phosphate monobasic
NaOH	sodium hydroxide
NAOAc	sodium acetate
-NH <sub>2</sub>	amino functional group
NHS	N-hydroxysuccinimide
nm	nanometer, 1 x 10 <sup>-9</sup> meter
NP(s)	nanoparticle(s)
NY6	Nylon 6
O	oxygen
-OH	hydroxyl functional group
Pa	Pascal, unit of pressure
pA	picoampere
PAA	poly(acrylic acid)
PAH	poly(allylamine hydrochloride)
PAN	polyacrylonitrile

PDADMAC	poly(diallyldimethylammonium chloride)
PEI	polyethyleneimine
PEO	polyethylene oxide
PET	polyethylene terephthalate
pH	negative decadic logarithm of H <sup>+</sup> ion concentration; measures acidity/basicity of solution
PLGA	poly(lactic-co-glycolic) acid
PP	polypropylene
ppm	parts per million, (mass of solute/mass of solution) x 10 <sup>6</sup>
PSS	poly(sodium 4-styrenesulfonate)
PVC	polyvinyl chloride
PVS	poly(sodium vinylsulfonate)
rpm	rotations per minute
s or sec	second
S	sulfur
SDS	sodium dodecyl sulfate
SE	secondary electrons
SEM	scanning electron microscopy
SnO <sub>2</sub>	tin dioxide
sp <sup>3</sup> hybridization	mixing of orbitals with one 2s-orbital and three 2p-orbitals of a carbon
C	carbon
sulfo-NHS	N-hydroxysulfosuccinimide
-S=O	sulfonyl functional group
T <sub>d</sub>	degradation temperature
TEM	transmission electron microscopy
TGA	thermogravimetric analysis
TiO <sub>2</sub>	titanium dioxide
Torr	unit of pressure
T-to-C distance	tip to collector distance
μm	micrometer, 1 x 10 <sup>-6</sup>
μS	microSiemen
U.S. EPA	United States Environmental Protection Agency
UV	ultraviolet (light/radiation); wavelengths in range 10 -400 nm
V	volt
vis	visible
vol	volume
wt	weight
XPS	X-ray photoelectron spectroscopy
ZnO	zinc oxide
1s	s atomic orbital
2p	p atomic orbital
3d	d atomic orbital
3D	three dimensional
%	percent
~	approximately equal to
→	yields

”	inch
⊕	positive charge
⊖	negative charge
°	degree
$\lambda$	wavelength
$\epsilon$	dielectric constant
$\gamma$	surface tension
$\Delta$	difference
$\Delta L^*$	color indicator; positive = lightening; negative = darkening
$\Delta a^*$	color indicator; positive = red; negative = green
$\Delta b^*$	color indicator; positive = yellow; negative = blue
$\leq$	less than or equal to
$\geq$	greater than or equal to
$\pm$	plus or minus

## PREFACE

Magnetite ( $\text{Fe}_3\text{O}_4$ ) nanoparticles incorporated into fibers can serve for various applications. Some include water treatment<sup>1</sup>, biomedical<sup>2-3</sup>, lithium-ion battery<sup>4</sup>, and anti-counterfeiting applications.<sup>5</sup> For potential wastewater treatment applications, these particles are intriguing because of the superparamagnetic and adsorption property they can introduce to the nanofibers. Since the full impact of metal oxide nanoparticles to the environment is unknown and they are known to induce toxic and inflammatory effects to human endothelial cells it is significant to study a durable binding strategy.<sup>6-7</sup>

This thesis focuses on the development of three techniques for nanoparticle loading on Nylon 6 nanomembraes. The composite membranes are evaluated for treatment homogeneity and durability. Chapter 1 describes the literature on the electrospinning process, background on the three different methods-1) electro-spinning/spraying 2) Layer-by-Layer assembly, 3) chemical grafting, and properties of the nanoparticles that are useful for the intended application.

Chapter 2 presents the experimental procedures applied in this study. Optimization of the upscaled, multi-jet electrospinning system to obtain a high through-put nanofiber membrane is discussed as well as the process conditions for the three methods and the washing protocol that was developed to examine treatment durability. Common material characterization techniques, such as electron microscopy and thermal gravimetric analysis are described. Less common techniques are also discussed, like CIELAB color value analysis, zeta potential to measure surface charges, and ICP-AES to quantify the amount of trace metals in solutions.

In Chapter 3 we describe the results from this study. This section is divided into three parts. The first part discusses characterization results of the pristine nanofibers and nanoparticles, the second part discusses the results that helped inform the optimization conditions of each

method, and the third part is a comparative study on the composite membranes for treatment homogeneity and durability. Conclusions and future work is presented in Chapter 4 and 5. Chapter 7 is an appendix of supplemental data that supports conclusions drawn from this study.

## **CHAPTER 1: LITERATURE REVIEW**

### **Electrospinning**

#### *Historical Overview*

The intriguing characteristics of nano-size fibers, such as large surface to volume ratios, small diameters, high porosity, high permeability, and high aspect ratios have led to their use in several applications. An application of interest for this study is for wastewater treatment. The fundamental ideas for electrospinning a viscoelastic polymer to form long, thin continuous filaments by the use of an electrostatic force dates back to patents filed in the 1930s-1940s by Formhals.<sup>8</sup> During the 1990s Reneker's group stimulated world-wide interest in electrospinning by demonstrating it is a simple, rapid method to produce fibers with diameters in the size range of 100-1000 nm from a variety of polymers.<sup>9-10</sup> These fibers are hundreds of times thinner than a human hair and one to two orders of magnitude finer than micron-sized, conventional fibers.

#### *Nanofiber Production Techniques*

Other nanofiber production techniques include melt extrusion,<sup>11-12</sup> melt spinning,<sup>13</sup> melt blowing,<sup>14</sup> and island in the sea.<sup>15-16</sup> To help increase high mass throughput centrifugal force spinning,<sup>17-18</sup> electroblowing<sup>19-20</sup> as well as multi-jet,<sup>19,21-22</sup> edge or bowl,<sup>23</sup> and needleless<sup>24</sup> electrospinning have been developed. In this study, fibers were produced via electrospinning because it is an efficient method to spin various polymer types out of solution, continuous fibers can be produced, little or no solvent waste is generated in the fiber production process since the solvents used have fast evaporation rates, it does not require high temperature conditions or complex instrumentation. The nanofibers were produced on a multi-jet set up and collected on a large rotating drum to overcome low throughput, reduce production time and obtain membranes of homogeneous fiber density.

### *Description of Electrospinning Process*

The electrospinning setup has three key features: a syringe and needle, a DC power supply, and a grounded, conductive collector as shown in Figure 1.1. A syringe pump is connected to the end of the syringe. It can control the flow rate of the polymer solution through the needle. When voltage is applied, the droplet at the tip of the needle forms a Taylor cone from the repulsive charges of the polymer solution and Coulombic forces from the applied electric field. In 1964 Taylor mathematically demonstrated that the charged droplet deforms into a stable conical configuration at a semi-vertical angle.<sup>25</sup> At high voltages (15–30 kV) the electrostatic forces of the field are strong enough to overcome the surface tension of the polymer solution to force the liquid out as a jet. The jet spins out toward the conductive collector to form thin, long all-over oriented fibers. The solvent evaporates as the polymer solution travels from the needle tip to the collector.<sup>9, 10, 26</sup>

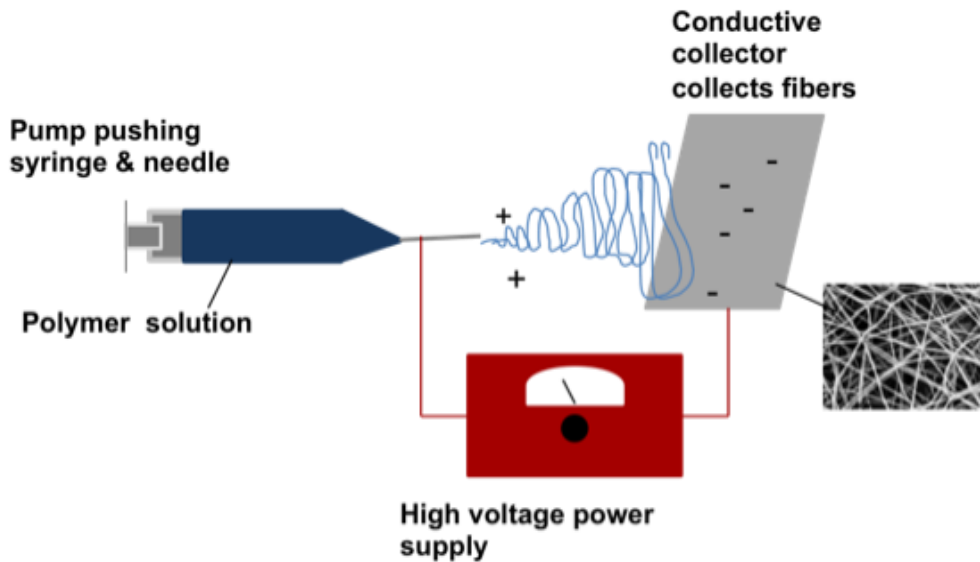


**Figure 1.1 Basic electrospinning set-up**

### *Parameters that Effect Electrospinning of Nanofibers*

The electrospinning and solution parameters, such as the voltage, flow rate, the distance between the needle tip to the collector, the polymer concentration, the viscosity and solution

conductivity can be varied to control fiber morphology and diameter size. The effect of adjusting these parameters for fiber formation is shown in Table 1.1 based on general trends observed.<sup>23, 26, 27-28</sup> The specific parameters to achieve fiber uniformity and a particular fiber size may vary from general trends based on the particular polymer-solvent system. The parameters also have upper and lower limits for successful electrospinning.

Fiber uniformity is defined by the round, cylindrical shape a fiber can acquire. Non-uniform fibers are characterized by having an inconsistent fiber diameter in the longitudinal direction with beads. Fibers at the nanoscale can fall within the size range of 50 nm to 1000 nm.

**Table 1.1 Variable electrospinning parameters<sup>27-28</sup>**

Parameter	Fiber Uniformity	Fiber Diameter Size
↑ Polymer concentration/viscosity	↑	↑
↑ Polymer solution conductivity	↑	↓
↑ Applied Voltage	↑	↓
↑ Flow Rate	↓	↑
↑ Tip to Collector Distance	↑	↓

--- Polymer-solvent system parameters

--- Electrospinning process parameters

The characteristics of the polymer and its solvent system play a significant role for fiber formation via electrospinning. The viscosity of the solution is determined by the polymer concentration and the molecular weight. Nylon 6 nanofibers of a weight % between 10% - 25 % can yield fibers.<sup>29-30</sup> High molecular weight polymers can offer good chain entanglement for fiber formation at low weight %, but also introduce high viscosity as the polymer concentration increases. Droplets sprayed on the collector indicate that the viscosity and polymer concentration are too low. A polymer solution is too viscous if it resists deformation and struggles to form a Taylor cone with applied voltage. Increasing the solution conductivity can help reduce surface tension and Rayleigh instability during electrospinning to promote fiber elongation and

uniformity. The conductivity of the solution can be enhanced by modifying the solvent system,<sup>31</sup> the addition of salts<sup>32</sup> or conductive nanoparticles.<sup>4,33</sup> These additives can act as charge carriers.

Closely monitoring the electrospinning process parameters is necessary to produce fibers with good morphology. As applied voltage increases, typically 15 kV to 30 kV for Nylon 6, greater fiber uniformity is observed due to the increased field strength. The field strength may be too low if the polymer solution is not forming a Taylor cone. A higher voltage would be required for highly viscous solutions since it would take stronger electrostatic forces to obtain a Taylor cone jet. A proper flow rate would not produce excessive solution dripping and the solution would slowly flow out the needle tip before voltage is applied. As the flow rate is reduced the fiber uniformity increases because the solvent has more time to evaporate and the fibers have more time to elongate into thinner fibers. The tip-to-collector (T-to-C) distance should be a distance far enough to allow fibers enough time to elongate for uniformity and sufficient time for solvent evaporation.

### *Review of Composite Nanofibers*

Composite nanomaterials have been extensively researched to achieve enhanced chemical and physical properties for various functional applications as shown in Figure 1.2.<sup>33-34</sup> These applications include filtration, energy, biotechnology, sensor devices, and smart materials. Composite fibers are a combination of a fiber forming polymer and at least one other chemical compound.<sup>34</sup> Typically, the additional compounds can be mixed into the polymer solution prior to electrospinning, precursor solutions can be prepared separately and integrated together during electrospinning to form core/shell structured fibers, or the additional compounds can be incorporated as a post treatment on the electrospun materials. The next few paragraphs will discuss applications of metal oxides and the type of polymers they have been incorporated into.

Semiconductor metal oxides, such as ZnO, TiO<sub>2</sub>, CuO, Al<sub>2</sub>O<sub>3</sub>, SnO<sub>2</sub>, Fe<sub>3</sub>O<sub>4</sub> can introduce several functionalities to fibers, including UV protection<sup>35</sup>, superhydrophobicity,<sup>36</sup> self-detoxification and filtration of organic pollutants,<sup>1,37-38</sup> photoelectrode functionality for dye synthesized solar cells<sup>33</sup>, and chemical sensing capabilities<sup>39-40</sup>. Typically, for energy storage or detection applications the metal oxides are incorporated with mechanically robust and chemically inert polymers, such as carbon and its precursor, polyacrylonitrile (PAN). The UV protective and superhydrophobic properties are useful for apparel, so the treatment is common for cotton and polyester fibers.

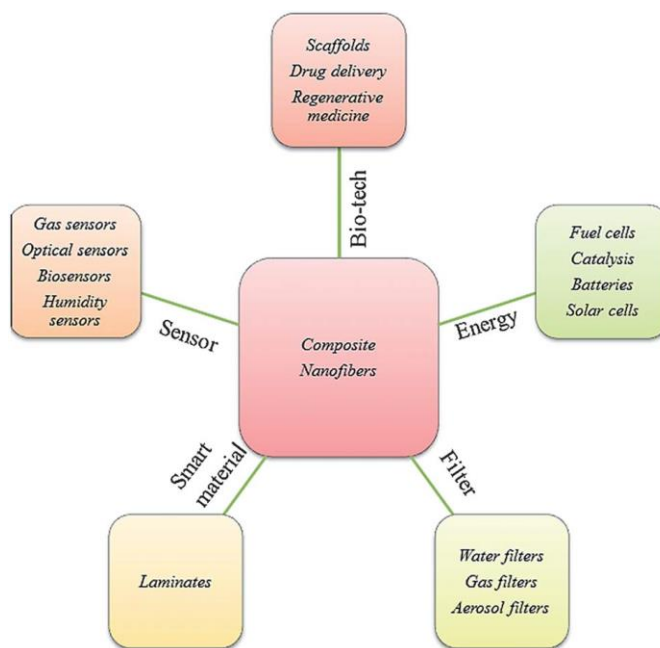


**Figure 1.2 Overview of composite nanofiber membrane applications<sup>34</sup>**

On a narrower focus, researchers have prepared composite nanofibers of Fe<sub>3</sub>O<sub>4</sub> NPs with polymers, such as PAN,<sup>1,27</sup> carbon,<sup>4</sup> polyethylene oxide (PEO),<sup>5</sup> poly(lactic-co-glycolic) acid (PLGA),<sup>2-3</sup> and polyethylene terephthalate (PET)<sup>41</sup> by adding the particles directly into the spinning dope or as a post treatment. PAN and carbon fibers are appealing because they offer superior strength, are super lightweight, and are chemically inert. PET fibers also offer good mechanical properties. The PEO polymer offers good solvent compatibility with ferrofluids.

Nylon 6 nanofibers will be prepared in this study since they have superior mechanical properties with high tensile strength, good abrasion resistance, and chemical resistivity comparable to PAN fibers.<sup>42</sup>

## **Review on Methods for Nanoparticle Incorporation**

### *Electrospraying*

Electrospraying, also known as electrohydrodynamic atomization follows a similar concept to electrospinning. The fundamental idea of applying electrostatic forces to a liquid solution to form an aerosol spray from the tip of a glass capillary was first observed by Bose in 1745.<sup>43</sup> Electro spray droplet behavior was further studied and photographed by Zeleny in 1917.<sup>44</sup> When an electric field is applied to a liquid solution, a cone forms at the apex and the liquid destabilizes into fines droplets travelling toward a grounded collector as multiple jets. The jets destabilize into droplets due to varicose and kink instabilities. These instabilities develop when the charge surpasses the Rayleigh limit. The Rayleigh limit is a theoretical and experimentally confirmed estimation of the maximum amount of charge a liquid can hold.<sup>45-46</sup> The droplet size can vary from nm to  $\mu\text{m}$  depending on the needle gauge, solution conductivity, flow rate, voltage, and solvent. The applied voltage is critical for the control and motion of the droplets. Electrospaying is typically used for thin film deposition,<sup>47</sup> tissue regeneration,<sup>48</sup> and particle encapsulation for controlled release toward catalysis and drug delivery applications.<sup>49, 50</sup>

Electrospraying is a facile route to incorporate NPs within fibers, independent of polymer-particle solvent compatibilities. The simultaneous electro-spinning/spraying method allows particles to become physically trapped within the fiber matrix. Additionally, this process does not disrupt homogenous fiber formation. Using electricity to deposit the NPs can be an efficient process because the droplets can self-disperse in space from the inherent repulsion.

Jaworek et al reported electrospaying various metal oxides on polymeric fibers with methanol as the particle solvent. The electrospaying was completed by three approaches: 1. electrospaying while simultaneously electrospinning, 2. electrospinning first, then electrospaying, and 3. electrospinning on a collector that is at room temperature, then transferring it to a heated table for electrospaying. Figure 1.3 displays TiO<sub>2</sub> NPs loaded on PVC nanofibers.<sup>51</sup> Figure 1.4 shows a particle solution dispersing from the needle tip with an applied electric field toward the collector.<sup>52</sup> The simultaneous electrospinning/electrospaying process resulted in a homogeneous distribution of particles between the layers. The other two processes provided a denser nanoparticle coating directly on the surface of the nanomembranes.

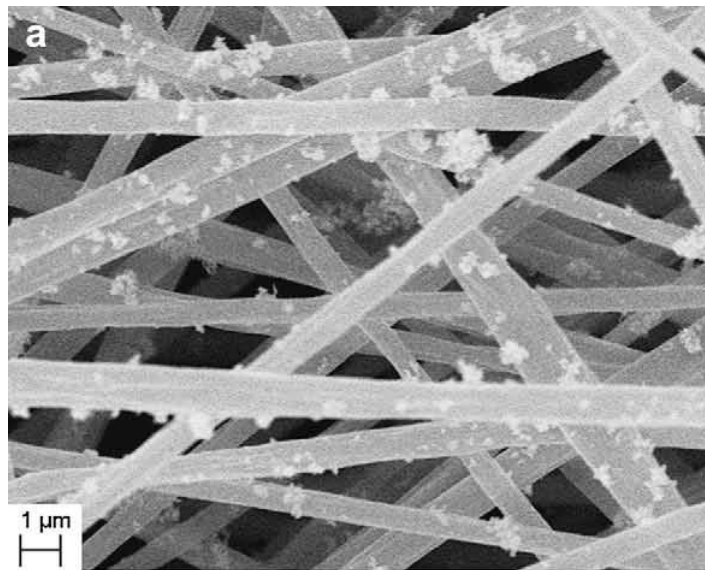


Figure 1.3 TiO<sub>2</sub> NPs loaded on PVC nanofibers via electrospaying<sup>51</sup>



Figure 1.4 CCD camera image of TiO<sub>2</sub> NPs spraying toward collector forming a cone jet<sup>52</sup>

### *Layer-by-Layer Assembly*

Layer-by-layer (LbL) assembly can be used to form electrostatic interactions between positively and negatively charged compounds, such as polymers and particles. LbL is a method that involves immersing a charged substrate into a polyelectrolyte bath that is oppositely charged to allow for adsorption of the desired compounds on the surface (Figure 1.5).<sup>53</sup> The technique can be repeated to form multiple layers on the surface with rinses of water in between.

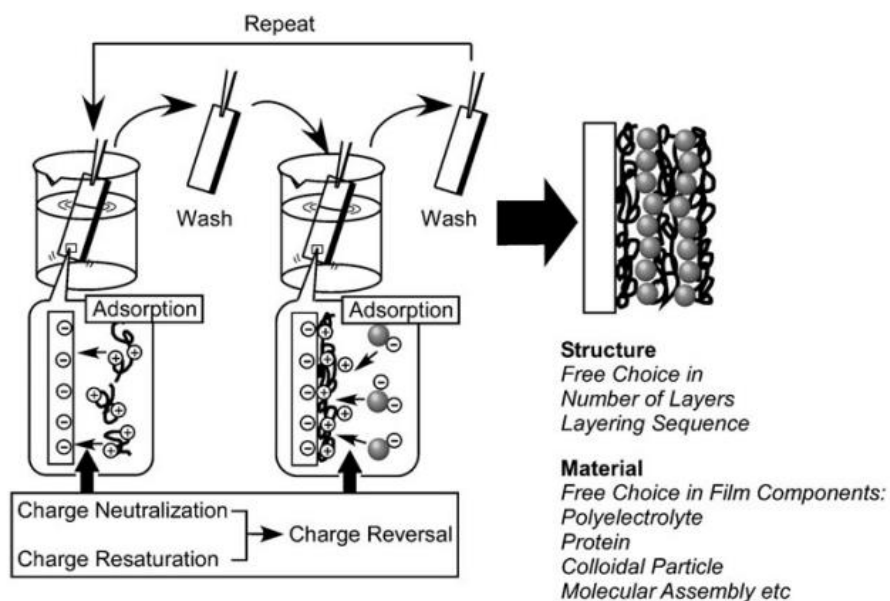


Figure 1.5 Schematic of general layer-by-layer assembly<sup>53</sup>

Polyelectrolytes are polymers that have a charged functional group on each repeating unit. They can be classified as cationic or anionic and strong or weak. Common cationic polymers include poly(diallyldimethylammonium chloride) (PDADMAC), poly(ethyleneimine) (PEI), and poly(allylamine hydrochloride) (PAH). Examples of anionic polyelectrolytes include, poly(acrylic acid) (PAA), poly(sodium styrenesulfonate) (PSS), poly(sodium vinylsulfonate) (PVS). Depending on how well the polyelectrolytes dissociate in aqueous solution they can be further distinguished as weak or strong. The charge of weak polyelectrolytes can be optimized by altering the ionic strength with the buffer concentration or pH environment for good adsorption to a material.<sup>53</sup>

The adsorption behavior of a charged compound can be attributed to solvent compatibility, pH environment, and ionic strength. In order for new ion pairs to form between oppositely charged compounds counter ions must dissociate away from the charged compounds to allow these new pairs to develop. In good solvents, polyelectrolytes form compact globular conformations and have a reduced charge overall. The solvent molecules screen the charged repeat units of the polymer to stabilize the electrostatic forces between them. The charged polymer itself experiences less repulsive forces because of screening effect from solvent to form a compact structure. In poor solvents the charged polymer takes a looser, more linear conformation because of less effective screening between the repeating units and electrostatic repulsion.<sup>54, 55</sup> Dobrynin et al suggest the ideal polymer conformation is a necklace structure, which can allow for uniform polymer distribution.<sup>56</sup> The ionic strength in an aqueous solution can also have a similar screening effect. For uniformity on the substrate, low ionic strength is preferred because it has a low screening effect on the polymer to minimize repulsion and produces a looser conformation.<sup>55</sup>

A few researchers have reported LbL assembly using NPs and fibrous polymers. Dubas et al reported on the LbL assembly of cationic, poly(diallyldimethylammonium chloride) (PDADMAC) and anionic, polymethylacrylic acid coated silver NPs (PMAcapAg NPs) on micron-sized Nylon 6 fabrics.<sup>57</sup> Polymer coated Ag NPs were directly incorporated in the LbL assembly at pH = 7 using 1mM sodium acetate (NaOAc) buffer solution. Park et al reported on the LbL assembly of anionic, poly(sodium 4-styrenesulfonate) (PSS,  $M_w \sim 70$  kDa) and cationic, poly(allyamine hydrochloride) (PAH) with polyethyleneimine (PEI) as the first layer on electrospun Nylon 6 nanofiber membranes.<sup>58</sup> In both studies the activating layers were sufficient to produce the desired functionality on the fibrous substrates. Characterization techniques included UV-Vis, monitoring K/S values, and electron microscopy.

#### *Chemical Grafting Reaction*

EDC/NHS chemistry has demonstrated to be a viable method for functionalizing fibrous materials. 1-ethyl-3-(3-dimethylaminopropyl)carbodiimide (EDC) is a highly reactive, water soluble carbodiimide often used as a coupling agent. Under an inert atmosphere, it activates carboxylate ions to react with primary amines for amidization. It is often paired with N-hydroxysuccinimide (NHS) to introduce stability to a key intermediate in the reaction by the formation of an ester functional group, preventing hydrolysis. EDC/NHS chemistry is widely used for chemical grafting of polysaccharides,<sup>59</sup> conjugation of peptide synthesis, and conjugation to NPs.<sup>60, 61-62</sup>

In 1995 Nakajima et al proposed a potential mechanism for the reaction between carboxylate ions and amines with EDC in aqueous solution (Figure 1.6). EDC (1) can follow one of two pathways. If the reaction is not carried out in buffer solution and in an inert atmosphere EDC can easily hydrolyze to form a stable, unreactive urea intermediate (2). If EDC is under the

proper environmental conditions it can react with a carboxylate ion to form O-acylisourea (3). The O-acylisourea intermediate is significant for amidization and it can potentially take four different routes. Firstly, it can be reprotonated at the Schiff base site to form a carbocation (4). The Schiff base site is a functional group composed of a carbon-nitrogen double bond attached to an alkyl group. Carboxylate anions may form as by-products and rapidly react with one another to produce carboxylic anhydrides (8) if the carboxyl group is cyclic. If the carboxyl group is not cyclic then the carbon center of O-acylisourea can react with a nucleophilic amine group to form an amide bond (7), which is the desired reaction. O-acylisourea may also react with oxygen atoms of water in the solution, which can yield re-formed carboxlates (6) or isoureas, inactivating EDC.<sup>60</sup> If excess EDC is present it can react with O-acylisourea to form a stable, N-acylurea intermediate.<sup>63</sup> To minimize the risk of EDC hydrolysis and its inactivation, NHS can be used as an additional coupling agent. NHS esters hydrolyze slowly in water and can rapidly react with nucleophilic amine groups to improve the coupling efficiency.<sup>60</sup>

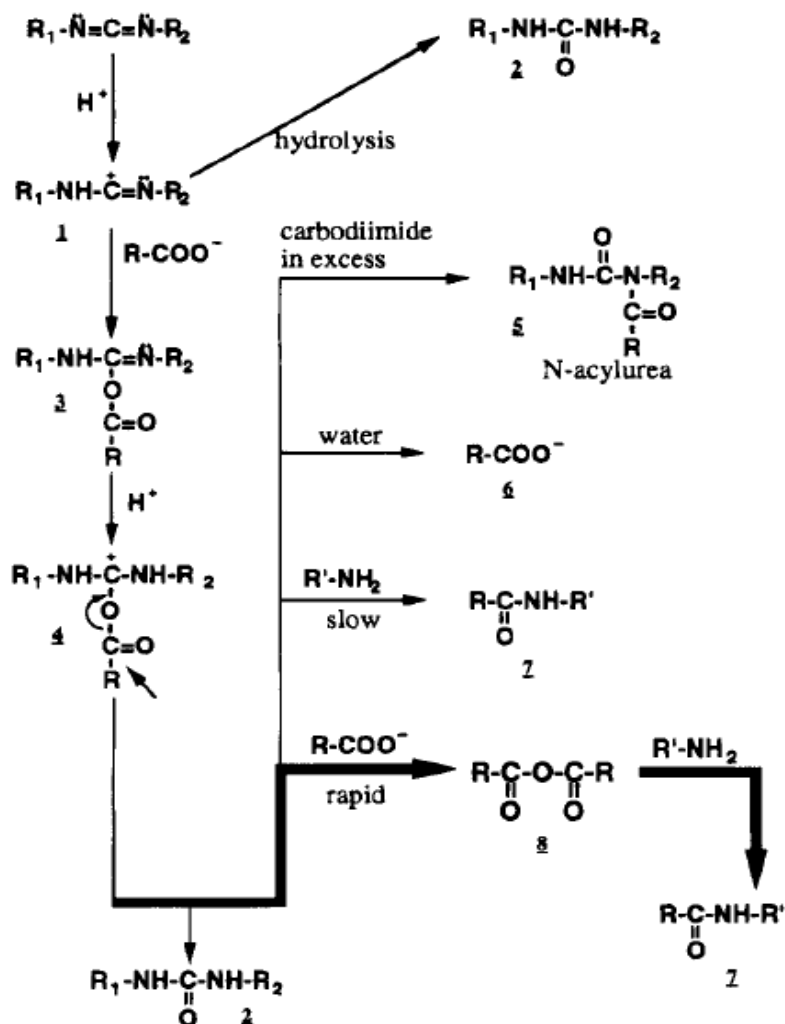


Figure 1.6 Proposed amidization mechanism with EDC<sup>63</sup>

Parameters that are typically considered for the reaction are the EDC/NHS ratio relative to one another, the available carboxylate ions and amine groups, the pH environment, the buffer type/concentration, reaction time allowed between the EDC/NHS activated carboxyl groups and amine groups, and temperature. Table 1.2 displays the experimental conditions from researchers who utilized EDC/NHS chemistry for amidization. It is significant to note the different conditions that were determined to optimize the reaction. In some studies EDC is only used while in others EDC is combined with NHS. An environment with a pH of 5 to 9, a buffer concentration  $\leq 10$  mM, and various buffer types have been used. A reaction time of 30 min is generally accepted, but it can be lengthened to 24 hrs. The washing protocol to remove excess

EDC, NHS, or by-products can be water, a buffer, or polar solvents. Nakajima et al suggested that the optimal condition to facilitate the reaction is at pH = 5, however, the coupling reaction can still proceed at a higher pH.

**Table 1.2 Experimental conditions for amidization reaction**

<b>Parameter</b>	<b>Conditions from literature</b>
EDC/NHS ratio	<ul style="list-style-type: none"> <li>▪ 1:4<sup>64-65</sup></li> <li>▪ 1:0,<sup>63-65</sup></li> <li>▪ 1:2<sup>60</sup></li> </ul>
pH environment	<ul style="list-style-type: none"> <li>▪ ~5.0<sup>63, 64</sup></li> <li>▪ 9.0<sup>60</sup></li> </ul>
Buffer type and concentration	<ul style="list-style-type: none"> <li>▪ 10 mM NAOAc<sup>64</sup></li> <li>▪ DI-H<sub>2</sub>O<sup>65</sup></li> <li>▪ 10 mM and 7.5 mM sodium borate<sup>60</sup></li> <li>▪ 100 mM NaH<sub>2</sub>PO<sub>4</sub>/acetic acid<sup>63</sup></li> </ul>
Amidization reaction time (NHS activated -COO <sup>-</sup> + -NH <sub>2</sub> )	<ul style="list-style-type: none"> <li>▪ 20 min<sup>64</sup></li> <li>▪ 30 min<sup>63-65</sup></li> <li>▪ 24 hrs<sup>60</sup></li> </ul>
Temperature	<ul style="list-style-type: none"> <li>▪ 21°C<sup>60, 64-65</sup></li> <li>▪ 25°C<sup>63</sup></li> </ul>
Washing off excess/unreacted compounds	<ul style="list-style-type: none"> <li>▪ NAOAc<sup>64</sup></li> <li>▪ DI-H<sub>2</sub>O/CH<sub>3</sub>OH<sup>65</sup></li> <li>▪ tris-borate-EDTA<sup>60</sup></li> </ul>
Confirmation of bonding (direct and indirect)	<ul style="list-style-type: none"> <li>▪ XPS<sup>64-65</sup></li> <li>▪ gel electrophoresis<sup>60</sup></li> <li>▪ FTIR<sup>63</sup></li> <li>▪ C13-NMR<sup>63</sup></li> </ul>

Tobiesen et al demonstrated how EDC/NHS chemistry can be utilized to increase the surface functionality of synthetic polymers that typically have few reactive groups, such as Nylon 66. The presence of 250 kDa poly(acrylic acid) (PAA) on Nylon 66 films was confirmed via XPS analysis of the new C-O groups belonging to PAA.<sup>65</sup> To demonstrate that the PAA activated films gained higher reactive sites, the films were subsequently treated with hexylamine. At a 10 nm depth into the surface of the film, a high resolution scan of the C1s band demonstrated the presence of PAA with an increase in the width of the band and toward higher binding energy compared to the pristine NY66 film (Figure 1.7). The presence of electronegative

groups causes a shift toward higher binding energies. The  $\text{CH}_x$  bands shifted and had a binding energy of 281.5 eV while  $\underline{\text{C}}\text{-CO}_2$  and  $\underline{\text{C}}\text{O}_2$  had binding energy increases by 0.7 eV and 4 eV respectively. Neither the specific band shifts nor detection of the new  $\underline{\text{C}}\text{ONH-}$  bond were discussed. However, the N/C and O/C molar ratios of the samples as well as the molar ratios of EDC and NHS to the carboxylate functional groups of PAA were determined based on XPS analysis. Calculations revealed that the N/C and O/C molar ratios on pristine PAA would be N/C = 0 and O/C = 0.167 if PAA completely and uniformly covers the surface of the film. To estimate the actual coverage of PAA on the surface Equation 1.1 was used.

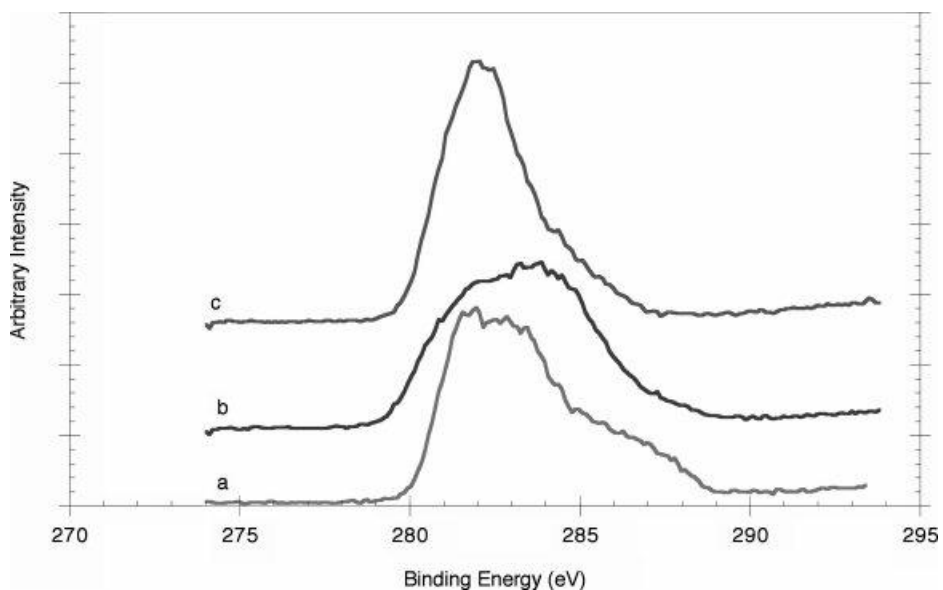


Figure 1.7 High resolution XPS scan of C1s band for a) pristine NY66 film, b) PAA-g-NY66 film, c) hexylamine-g-PAA-g-NY66 film<sup>65</sup>

Equation 1.1 Calculation to estimate the fraction of surface covered by PAA<sup>65</sup>

$$x_{PAA} = \frac{\left(\frac{O}{C} - \frac{N}{C}\right)}{0.67}$$

Table 1.3 displays a few representative examples of the N/C and O/C mol/mol ratios of the grafting reaction. In a control sample without any coupling agent, the addition of PAA caused the ratio of N/C to decrease and the O/C ratio remained unchanged. This indicates some

physical adsorption. With the addition of the coupling agents, ratios of N/C and O/C both increase suggesting that new –CONH bonds are forming and the surface of the film is being covered by PAA with the coupling agents.

**Table 1.3 Adapted table of varied molar ratios of EDC and NHS to graft PAA to NY66 films<sup>65</sup>**

Sample	NHS/COO (mol/mol)	EDC/COO (mol/mol)	N/C (mol/mol)	O/C (mol/mol)	Fraction PAA
Pristine NY66	---	---	0.14	0.16	0
Pristine PAA	0	0	0.08	0.15	0.10
PAA-g- ( $x = 0.39$ )	0	0.9	0.27	0.27	
PAA-g- ( $x = 0.31$ )	2.3	0.05	0.35	0.45	

PAA-g- = 250 kDa polyacrylic acid grafted to Nylon 66

### *Evaluating NP Treatment Durability*

To compare the three treatment methods it is significant to review washing protocols for NP durability on fibers. Benn et al studied the release of nano-Ag from four commercially available sock fabrics in ultra pure wash water under agitation. After one 24 hr cycle the NP release was measured with ICP-OES. The NP release ranged from approximately 0 – 0.400 ppm with the range dependent on the preparation method of the composite fibers. The samples were immersed in new baths for each cycle. After four 24 hr consecutive cycles the NP release ranged from 0.038 – 3.600 ppm. These results indicate that the physical NP durability on fibers can be evaluated simply with water immersion and agitation.<sup>66</sup>

Geranio et al studied Ag NP release on nine different textile fibers under conventional laundering conditions. The samples contained Ag NPs prepared via direct bonding, entrapped inside the fibers, and incorporated with a binder.<sup>67</sup> The washing conditions considered pH environment, surfactant, and oxidizing agent under agitation. The samples were immersed in a buffer solution at pH = 10 with a surfactant, sodium dodecyl sulfate (SDS), and an oxidizing agent, peracetic acid, was introduced into the solution after 100 minutes. Four of the nine samples containing NPs either directly inside the fiber or applied with a binder did not release Ag or released Ag below the detection limit (< 0.00864 ppm) of the ICP-OES instrument. Ag

release was detected from five fabric samples that were prepared by direct bonding, a surface coating, and directly inside the fiber. The samples displayed rapid initial release within 30 minutes, then the quantity reached saturation. After approximately 100 minutes in a pH=10/SDS washing environment, the five samples released Ag within the range of 0.0108 – 1.08 ppm. Introduction of the oxidizing agent generally led to an increase in Ag release, particularly significant for Ag deposited on fabrics via a coating method. These results indicate that a basic washing environment and additional chemicals can affect NP durability for composite fibers prepared by various methods.

For wastewater treatment applications, the NP release from the membranes should be none or very minimal from the fibers developed in this study.

### **Polymer Coated Iron Oxide Nanoparticles**

#### *Water Treatment Property*

Some current methods of treating heavy metals and cationic/anionic dye pollutants present in water include reverse osmosis,<sup>68</sup> ion exchange,<sup>69</sup> electrochemical,<sup>70-71</sup> and sorption.<sup>72</sup> Other material composites explored for their adsorption property in water treatment include chitosan,<sup>72</sup> a highly abundant natural polymer, additionally, 1D graphene and 2D graphene oxide have generated substantial attention as emerging water treatment materials.<sup>73-74</sup> In general, the use of nanomaterials for water treatment is being researched as an alternative to current technologies because of the multifunctional properties they can introduce to the systems.<sup>75</sup>

Several researchers have explored the adsorption ability of polymer coated Fe<sub>3</sub>O<sub>4</sub> NPs for water treatment of heavy metal pollutants. The surface coating on the NPs can act as a chelator to initiate a high and rapid pick-up rate of the metal ions in water. NPs coated with imines,<sup>76</sup> thiols,<sup>77-78</sup> carboxylic acid,<sup>79</sup> and amine<sup>80</sup> functional groups have all demonstrated efficient

adsorption of metal pollutants and recyclability due to the NPs magnetic property. Zhang et al prepared PAA/GO/Fe<sub>3</sub>O<sub>4</sub> composite NPs for adsorption of Cu<sup>2+</sup>, Cd<sup>2+</sup>, and Pb<sup>2+</sup> ions with over 85% pick-up.<sup>79</sup> The NP functional group would determine the optimal environmental conditions for adsorption and conditions for recyclability.

To our knowledge, one paper has been published that exploits the magnetic and adsorption properties of Fe<sub>3</sub>O<sub>4</sub> NPs on nanofiber membranes. Si et al developed mesoporous polybenzoxazine-based Fe<sub>3</sub>O<sub>4</sub> carbon nanofiber membranes prepared *in-situ*. The coordination complex that can form between Fe particles and the cationic dyes allowed for effective, rapid adsorption and removal of methylene blue (MB) and rhodamine B (RhB) from solution (Figure 1.8). The magnetic property allowed for simple separation of the composite membrane containing the active particles and pollutants.<sup>1</sup> However, the authors mentioned that separation of the adsorbed dyes is an issue for re-useability.

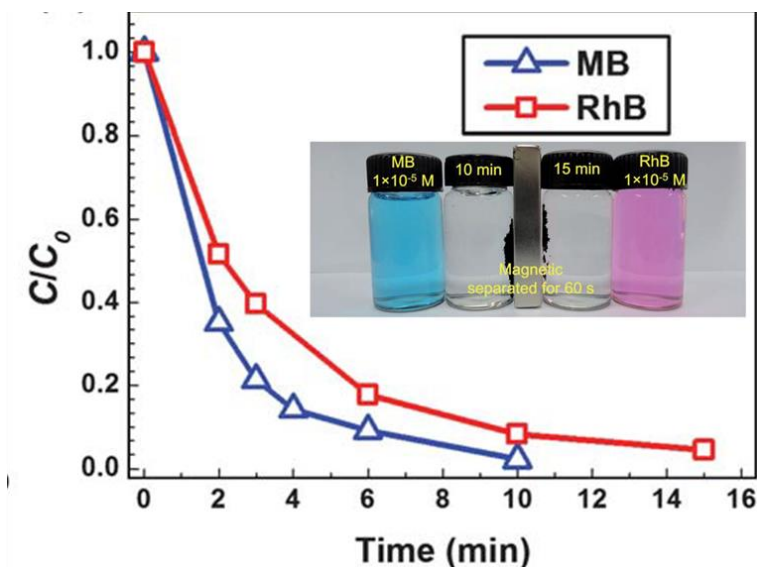


Figure 1.8 Adsorption of dyes overtime in a C/C<sub>0</sub> plot and photograph of magnetic separation, modified graphic<sup>1</sup>

### Magnetic Property

The unpaired electrons in the 3d atomic orbital of iron introduce its magnetic characteristics. Fe<sub>3</sub>O<sub>4</sub> in bulk form displays ferromagnetic behavior. Ferromagnetism is strong

magnetization due to permanent, parallel alignment of electron pairs independent of an external magnetic field.<sup>81</sup>

The magnetic performance of materials depends on permeability, coercivity, and hysteresis. Permeability is the magnitude of magnetization a material can gain. Coercivity ( $H_c$ ) is the magnitude of magnetization required to demagnetize a ferromagnetic material. A hysteresis curve can provide information about the type of magnetization and the history of the material.<sup>81</sup>

At the nanoscale, iron particles display superparamagnetic properties unobserved in bulk form because of magnetic anisotropy. Superparamagnetism occurs when the unpaired electrons flip from a random state into alignment along a crystallographic axis of the nanoparticle. The electron flips largely depend on the blocking temperature and Neel relaxation time, which have equations that consider NP energy barriers that must be overcome for magnetization.<sup>81</sup>  $Fe_3O_4$  NPs between the critical size of 8 - 20 nm are paramagnetic displaying temporary magnetization in the presence of an applied magnetic field.<sup>3,41</sup>

As mentioned earlier, the magnetic property of materials can be measured with a hysteresis loop (Figure 1.9). The measurement is taken with an external magnetic field ( $H_a$ ) as a function of magnetization ( $J$ ). If the material is not magnetized the data collection begins at (0, 0) and there is a rapid increase in magnetization as the field strength increases (curve NC). Saturation magnetization ( $J_s$ ) is observed once all the magnetic moments in the material orient parallel to the magnetic field. For paramagnetic materials the magnetization should return to zero when  $H_a = 0$ . A permanently magnetized material displays a hysteresis loop with reversal of the field because it cannot demagnetize,  $H_a \neq 0$ , and there is remnant magnetization ( $J_r$ ).  $H_c$  is the point in which there is no magnetization in the material with an applied magnetic field. Generally, ferromagnetic materials display a hysteresis loop, high coercivity, permeability, and

remnant magnetization. Super paramagnetic materials display low coercivity, no remnant magnetization, and no hysteresis loop.<sup>82</sup>

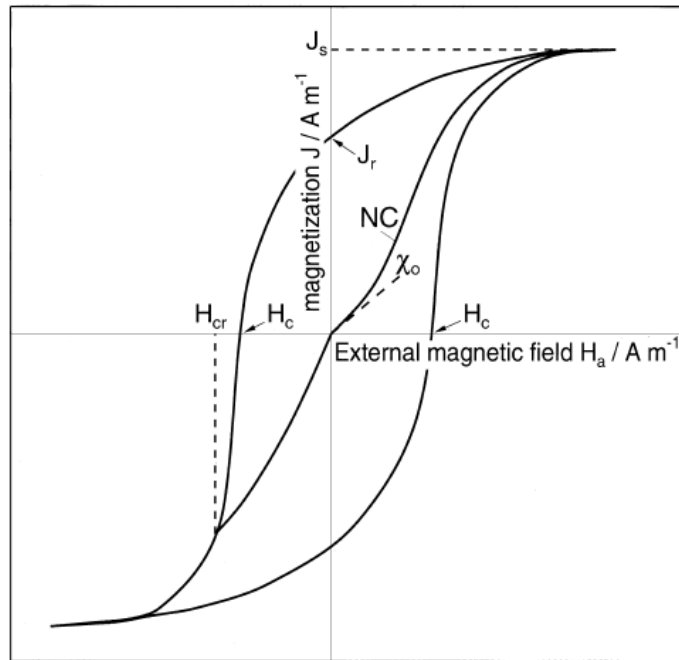


Figure 1.9 Representative hysteresis curves for magnetic materials<sup>82</sup>

## Basic Characterization Techniques

### *Scanning Electron Microscopy*

Scanning electron microscopy (SEM) allows for the analysis of the surface topography and composition of bulk samples at high magnification. Figure 1.10 shows the general diagram of a SEM. The electron gun operates with a tungsten filament, field emission tip or a LaB6 emitter at a high accelerating voltage (max 30 kV). It contains condenser and objective lenses, which focus the beam. The fine electron beam (nano-sized) is scanned in a horizontal, raster pattern above the sample by the scan coils. The electron from the beam excite atoms on the sample to emit secondary electrons (SE). The amount of SE emitted depends on the sample tilt. SE signals allow for analysis of the sample's surface features. SEMs may also detect high energy, backscattered electrons for elemental analysis of samples. The scan signals can be

transformed into an image by CRT display or, common today, digitally.<sup>83</sup> the system is under vacuum the whole time.

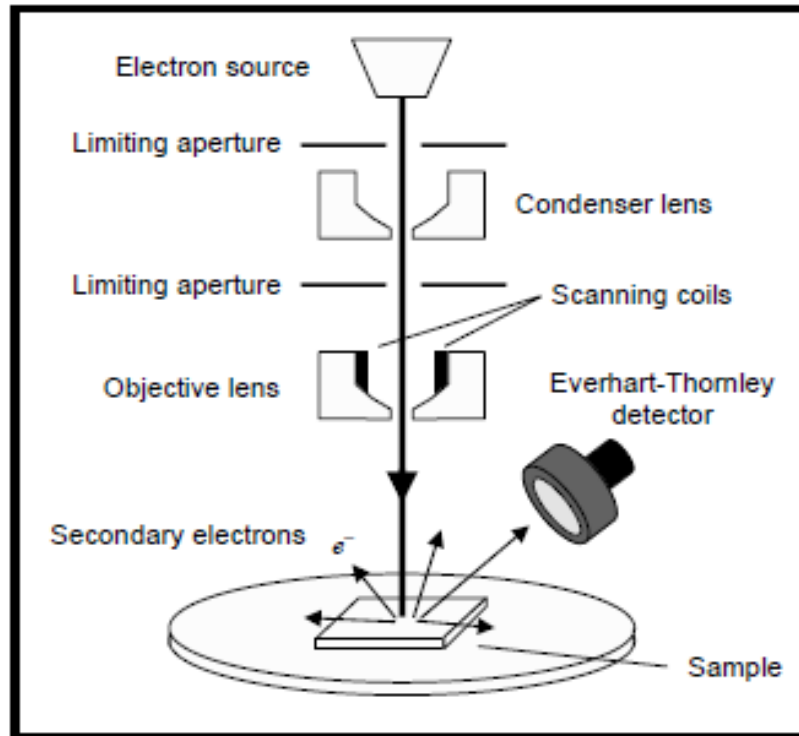


Figure 1.10 Diagram of scanning electron microscope<sup>84</sup>

### *Transmission Electron Microscopy*

Transmission electron microscopy is a technique in which electrons are transmitted through a thin sample to generate an image. TEM can examine the form, crystal structure, atomic composition, and electronic structure of the samples under vacuum.

As shown in Figure 1.11, the TEM operates with a beam of electrons provided by an electron gun that pass through many magnetic lenses along the column. The TEM has a few key features, which includes the illumination system, the sample stage, and the imaging system. The illumination system consists of the electron gun and the condenser lens. The electron gun supplies a micron-sized, static electron beam and can contain either a LaB<sub>6</sub> thermoionic or field emission source, which differ in illumination, beam coherence, and current density.<sup>85</sup> The

condenser lenses are significant to shape, size, and focus the electron beam to interact with the sample. The sample stage is where the sample holder is locked in place and it is important that adjustments in the x, y, and z directions can be made to determine the structural features of the nanomaterials.<sup>83</sup> The objective and magnification lenses (intermediate and projector) are arranged for atomic resolution imaging at high magnification.<sup>86</sup> The image recording system includes a fluorescent screen projector for the user to directly observe the area analyzed before the CCD camera is inserted for imaging. The samples must be electron transparent for imaging.<sup>85, 86</sup>

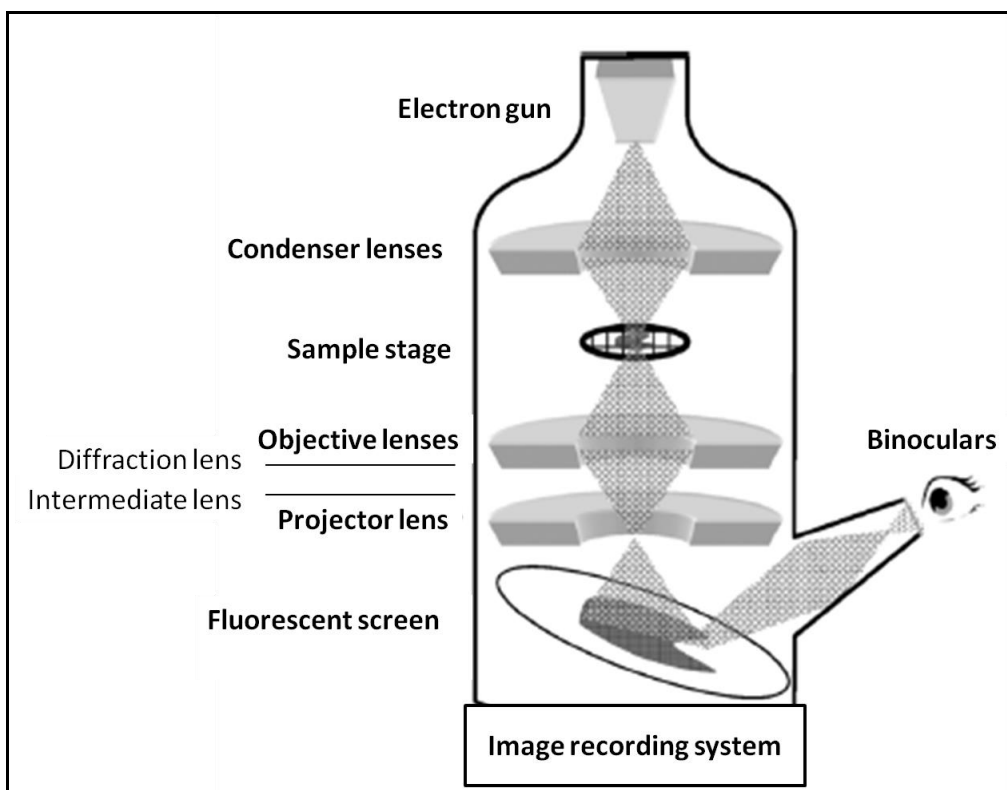


Figure 1.11 Diagram of transmission electron microscope, adapted<sup>87</sup>

TEMs may also have built in chemical analysis techniques, including energy-dispersive X-ray spectroscopy (EDX) and electron energy loss spectroscopy (EELS). EDX can determine the elemental composition of the sample. Each element has a specific atomic structure, which produces a distinct X-ray count when the sample is penetrated by the electron beam. EELS

measures the energy loss of electrons that penetrate the sample to provide insight to the electronic structure of the sample, such as valence and conduction bands, electron density, nearest neighbor interactions to list a few.<sup>86</sup>

## CHAPTER 2: EXPERIMENTAL PROCEDURE

### Materials

Nylon 6 pellets (10 kDa), 1-ethyl-3-(3-dimethylaminopropyl) carbodiimide hydrochloride (EDC), polyethyleneimine (PEI, 750 kDa), sodium phosphate monobasic (NaH<sub>2</sub>PO<sub>4</sub>) were purchased from Sigma-Aldrich (St. Louis, MO). Sodium hydroxide pellets (NaOH), 88% formic acid, hydrochloric acid (HCl) solution, acetone, and methanol were purchased from VWR International, LLC (Randor, Pennsylvania). 15 nm sized CA-Fe<sub>3</sub>O<sub>4</sub> NPs dispersed in DI-H<sub>2</sub>O (5 mg/mL) and soluble in polar solvents were supplied by Ocean NanoTech LLC (Springdale, AR). N-hydroxysulfosuccinimide (sulfo-NHS) was purchased from ProteoChem Inc (Loves Park, IL). DI H<sub>2</sub>O was used to prepare aqueous solutions.

### Electrospinning Conditions

25 and 20 weight % of Nylon 6 pellets (3mm) were dissolved in 88% formic acid and agitated with a wrist-action shaker for 24 hrs at room temperature to produce a polymer solution suitable for electrospinning. The weight % was calculated based on Equation 2.1 (Table 2.1).

**Equation 2.1 Weight % equation for polymer concentration**

$$\text{Weight \%} = \frac{x}{x+y} * 100$$

$x$  = material

$y$  = solvent

**Table 2.1 Quantities for 20 and 25 weight% Nylon 6 polymer solutions for electrospinning**

<b>Sample of Nylon 6 (wt%)</b>	<b>Nylon 6 pellets (g)</b>	<b>Formic Acid (g)</b>
20	3.00	12.00
25	3.75	11.25

The set-up developed for electrospinning was optimized for upscaled production (Figure 2.1). The system consists of a large rotating drum and two needle stands with six needles at each side. It was designed to eliminate stray fiber formation in areas beyond the grounded collector, reduce material waste, and produce homogeneous membranes on the collector. An insulation box

made of ¼” thick polypropylene (PP) sheets was built to surround the electrospinning system. To reduce material waste of polymer solution and plastic tubing, the polymer solution was set-up directly beside the needle stands instead of in a syringe. This revised setup helped reduce solution waste by 75% and decreased tubing use by 97%. The addition of an actuator, a motor that provides motion, allowed the drum to move along in the horizontal direction while rotating vertically. This addition helped eliminate large stripe formation from the stationary needles, increase membrane homogeneity and robustness.

20 wt% and 25 wt% nanofibers were produced at 25 kV applied voltage. 20 mL plastic syringes placed on the syringe pump (Harvard Apparatus) were filled with air and guided the solutions out of 22 gauge needle tips at a flow rate of 0.2 ml/hr. The T-to-C distance suitable for fiber formation was between 10 to 12.5 cm for 20 wt% and 15 cm for 25 wt%. Heavy duty aluminum (Al) foil was used as a collector (6 x 35 in<sup>2</sup>).

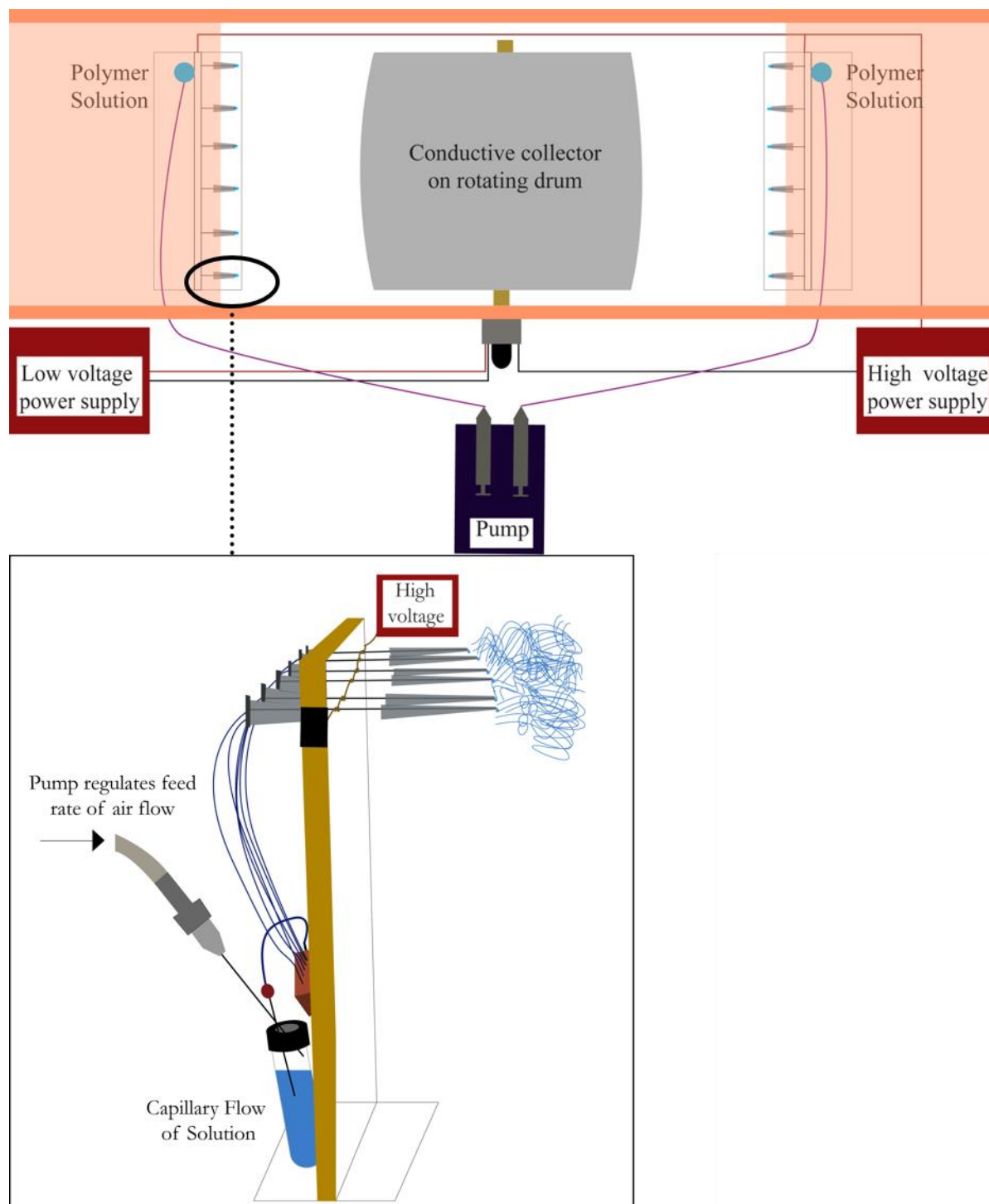


Figure 2.1 Aerial view of large scale electrospinning set-up. Zoom-in on side view of needle/solution reservoir set-up for electrospinning

### Buffer Solution Preparation

Buffer solutions were used extensively in the experiments, so the preparation will be briefly discussed.  $\text{NaH}_2\text{PO}_4$  was weighed out and dissolved in deionized water with a total

concentration of 5mM. NaOH or HCl were added to adjust the pH of the buffers to pH = 4, 7, 8, and 10 before the total volume was reached. These buffers were used for LbL assembly, the grafting reaction, and the washing protocol. The buffer solutions will be expressed as 5 mM NaH<sub>2</sub>PO<sub>4</sub>/H<sub>2</sub>O + NaOH/HCl.

### Electrospraying Conditions

1, 3, and 5 weight % CA-Fe<sub>3</sub>O<sub>4</sub> NP solutions dispersed in methanol were prepared for electrospaying and sonicated for 30 seconds. The quantities of NP solution/methanol added to prepare the solutions are shown in Table 2.2. A 20 wt% Nylon 6 polymer solution was used for the simultaneous electrospinning/electrospraying process.

**Table 2.2 Quantities of nanoparticle solutions for electrospaying**

<b>Sample of NP solution (wt%)</b>	<b>CA-Fe<sub>3</sub>O<sub>4</sub> NP (g)</b>	<b>CH<sub>3</sub>OH (g)</b>
1 wt%	0.2	16.4
3 wt%	0.495	16.5
5 wt%	0.825	16.5

Several experimental conditions were varied to observe homogeneous dispersion of the solutions on the collector with the multi-jet system. The initial trials did not contain NP solution. Deionized water doped with food colorant helped determine a suitable flow rate. The food colorant was a visual indicator of droplet behavior. A workable voltage, T-to-C distance, and needle gauge were determined using two volatile solvents, methanol and acetone, doped with food colorant while electrospaying. These solvents were selected from a few tested for dispersion (Table 2.3). They were also previously evaluated for electrospaying performance in the literature due to fast evaporation rates.<sup>49</sup>

**Table 2.3 CA-Fe<sub>3</sub>O<sub>4</sub> NP dispersion performance**

<b>NP Solvent Systems (100%)</b>	<b>Dispersion</b>
<b>Methanol</b>	✓
<b>Ethanol</b>	✓
<b>H<sub>2</sub>O</b>	✓
<b>Acetone</b>	✓
<b>Formic Acid</b>	X

The same applied voltage as electrospinning, 25 kV worked effectively for electrospaying when tested in a range of 7 to 25 kV. A T-to-C distance of 10 cm allowed for proper solvent evaporation and the charged droplets maintained stability directly toward the collector compared to a distance of 15 cm. 25 gauge needles were preferred over 20 gauge to produce droplets with smaller diameters. Methanol was selected as the optimal solvent because it produced homogeneous droplet dispersion during electrospaying.

The flow rate was optimized to increase spray time and solution dispersion between layers that build up on the membrane. The flow rate experiments consisted of the needle/solution reservoir set-up (Figure 2.2) with six 20 mL vials placed directly below the needle tips. The solution reservoir was placed above the height of the needles, similar to how IV bags are positioned for patients in hospitals for gravity to have greater influence on continuous and consistent flow of the non-viscous solution. To measure consistent solution flow through all six needles, the vials were weighed before and after flow rate trials. A 7 ml/min flow rate was initially set to allow equal and consistent pressure distribution along the six needles and it was quickly adjusted to slower flow rates. Flow rate ranges were between 0.08 to 1 ml/min in 0.2 ml/min increments. The lowest, consistent flow rate was 0.4 ml/min without applied voltage and 0.2 ml/min with applied voltage. The total operation time of the system was 4.5 hours (3 hrs electrospinning on one side, 1.5 hrs simultaneous electrospinning/electrospaying from alternate sides).

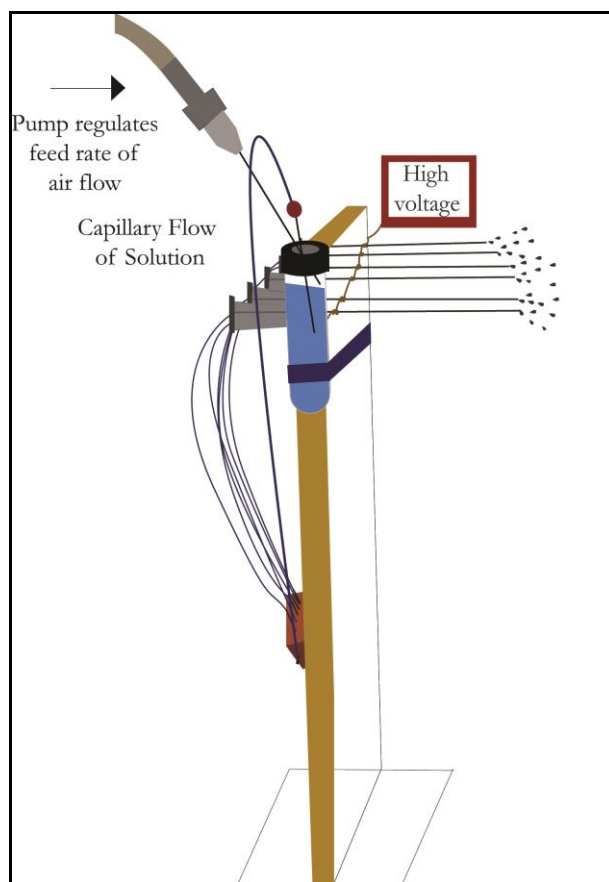


Figure 2.2 Side view of needle/solution reservoir set-up for electrospaying

### Layer-by-Layer Assembly Conditions

20 wt% Nylon 6 nanomembranes were cut into rectangular samples  $5 \times \frac{1}{2} \text{ cm}^2$  in size. The membranes were dipped in 0.08 wt/vol% polyethyleneimine (PEI, 750 kDa) and alternatively in 5 wt% CA-Fe<sub>3</sub>O<sub>4</sub> NP solution at pH = 7 for five minutes to produce a total of five bilayers. The concentration of PEI was within a range that would be useful for further characterization. The samples were rinsed in deionized water between each dip to remove excess and unreacted compounds. PEI, a weak polyelectrolyte was chosen for this study in place of PDADMAC, a strong polyelectrolyte because PDADMAC is incompatible with iron particles.

### Chemical Grafting Conditions

20 wt% Nylon 6 nanomembranes were cut into  $5 \times \frac{1}{2} \text{ cm}^2$  samples and presoaked in pH = 8 buffer solution for 15 minutes prior to reacting with the activated NPs. 5 mg of EDC and 5 mg

of sulfo-NHS were mixed in 1 mL of 5 mM  $\text{NaH}_2\text{PO}_4/\text{H}_2\text{O} + \text{NaOH}/\text{HCl}$  at  $\text{pH} = 8$  and immediately reacted with 5 mL of 3 wt% CA- $\text{Fe}_3\text{O}_4$  NP solution. If NP agglomeration occurred the solution was sonicated to improve dispersion. The mixture was agitated on a wrist-action-shaker for 20 min and the Nylon 6 membranes were subsequently immersed in the NP solution for 40 minutes. The reaction was carried out in an inert atmosphere. Unbound NPs were removed by washing the membranes in  $\text{CH}_3\text{OH}/\text{DI-H}_2\text{O}$  for 5 hrs. The time allowed to remove excess chemicals was limited to prevent physical decomposition of the nanomembrane. The amidization mechanism is depicted in Figure 2.3.

To confirm that the coupling agents reacted with the NPs, the functionalized particles were analyzed via ATR-FTIR. The NPs agglomerated with the addition of EDC and sulfo-NHS, which allowed for purification with a centrifuge. The solution was centrifuged for 30 sec at 6000 rpm. The supernatant solution was replaced by acetone two times and the particles were redispersed in solution by sonication for 5 - 10 seconds.

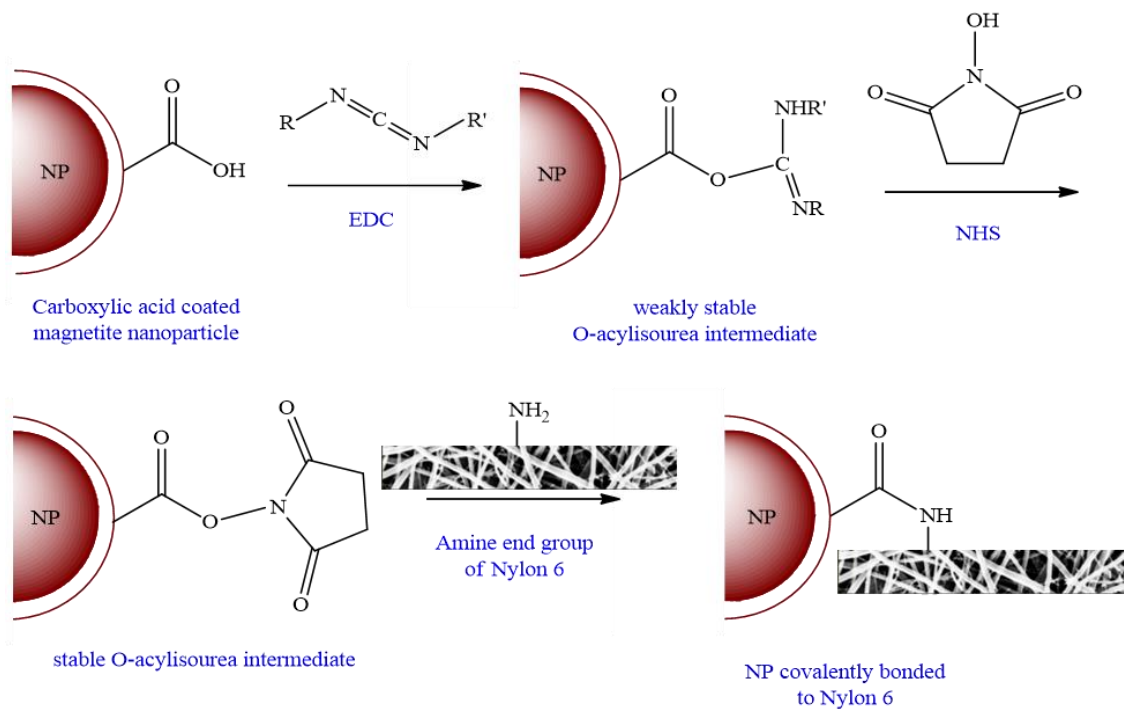


Figure 2.3 Amidization of a carboxylic acid with an amine using EDC/NHS coupling agents

### Direct Addition of Nanoparticles to Spinning Dope

The simple method of directly adding the NPs to the spinning dope of Nylon 6 was attempted as an initial method, however, formic acid caused NP agglomeration and instability due to the solvent's strong acidity. This solvent incompatibility motivated the electrospaying method.

### Washing Protocol

Six to seven milligrams of the nanomembranes treated with the NPs by the three methods were immersed in 15 mL baths. The composite membranes were immersed in varied pH baths (4, 7, 10) each with a buffer concentration of 5 mM NaH<sub>2</sub>PO<sub>4</sub>/ H<sub>2</sub>O + HCl/NaOH. The vials were agitated on a wrist-action-shaker for 10, 30, and 60 minutes. The washings were completed at room temperature and in two trials.

Aliquots of 5 mL were taken from each bath to determine Fe content in the solution per allotted time using inductively coupled plasma atomic emission spectroscopy (ICP-AES) (Spectro Analytical Instruments, INC). ICP-AES is capable of detecting and quantifying trace metals in aqueous solutions in parts per million (ppm). A matrix solution of high purity water standard was run prior to the samples. The lowest detectable amount of Fe in the samples was 0.004 ppm. The samples that released the highest amount of CA-Fe<sub>3</sub>O<sub>4</sub> NPs at 60 minutes according to ICP-AES results were dried at 21°C to examine the fiber morphology and evaluate nanoparticle presence via FESEM imaging and CIELAB.

## **Characterization**

### *Polymer Solution Viscosity*

The viscosity of 20 and 25 wt% Nylon 6 polymer solutions were measured with a TA Instruments Rheometrics AR 2000 rheometer. The data was analyzed by the Rheology Instrument Control software for the solutions as Newtonian fluids (Table 2.4). Measurements were conducted at a temperature of 25°C, with a continuous ramp step, a shear rate from 0-90 s<sup>-1</sup>. A 20 mm 4° steel cone with a truncation gap of 108 μm was used for all measurements. The duration of each experiment was 4 minutes. The average viscosities of the polymer solutions were calculated by shear rate vs. shear stress and standard error values are reported. Results indicate that ramping up the shear rate did not affect the viscosity. The viscosity of the solution increased with an increase in the weight % of the Nylon 6 polymer.

**Table 2.4 Viscosity values of Nylon 6 polymer solutions**

<b>Sample</b>	<b>Viscosity (Pa.s)</b>
<b>20 wt% Nylon 6 solution</b>	1.10 ± 0.101
<b>25 wt% Nylon 6 solution</b>	2.65 ± 0.179

### *Surface Tension Measurements*

The surface tension of the Nylon 6 polymer solutions were measured using the Sigma 701 Tensiometer (KSV Instruments). A micro-roughened platinum Wilhelmy plate was mechanically immersed in the polymer solution at 20 mm/min to the wetting depth of 6 mm. The polymer solution was poured into a glass beaker that was approximately 50 x 35 mm (diameter x height). During the experiments the surface tension is measured based on the maximum force required to lift the plate out of the solution. The maximum force is proportional to the surface tension of the solutions. Ten measurements were taken per experimental run and the surface tension values were averaged and analyzed with the KSV Sigma Software. The measurements occurred in a conditioning room at 22.2°C with a relative humidity of 66°C. The surface tensions of the 20 wt% and 25 wt% polymer solutions were not significantly different (Table 2.5).

**Table 2.5 Surface tensions of polymer solutions**

<b>Sample</b>	<b>Mean Surface Tension (mN/m)</b>
<b>20 wt% Nylon 6 solution</b>	40.92 ± 0.242
<b>25 wt% Nylon 6 solution</b>	42.53 ± 0.796

### *Scanning Electron Microscopy (SEM)*

A Leica 440 Scanning Electron Microscope was used to study the morphology of the fibers. The pristine 20 and 25 wt% Nylon 6 nanomembranes were mounted on Al stubs (Electron Microscopy Sciences) with carbon tape. They were coated with gold-palladium using Au-Pd sputter coater for 30 seconds since the samples must be electrically conductive for SEM imaging. The coating prevented charging on the insulative, fiber samples. All samples were imaged at an accelerating voltage of 25 kV, an electric current of 500 pA, and 6 mm working distance.

### *Field Emission Scanning Electron Microscopy (FESEM)*

A LEO-1550-FESEM (Keck-SEM) was used to confirm that the NPs were present on the nanomembranes by the three methods to study the particle dispersion and homogeneity. The

nanofiber samples were mounted on Al stubs (Electron Microscopy Sciences) with carbon tape and coated with carbon approximately 10 nm thick using a carbon coater for 15 seconds. All samples were imaged at low accelerating voltages varying between 3 - 4 kV with a working distance of 6 - 7 mm.

### *Transmission Electron Microscopy (TEM)*

A FEI-T12-TEM-STEM was used to examine the nanoparticle morphology and how the NPs are dispersed throughout the nanofibers. A Nikon SMZ-U Zoom 1: 10 light microscope was used to help prepare the samples for TEM analysis. A few nanofibers taken from the membrane were sandwiched between an oyster copper grid (Electron Microscopy Sciences) and secured in place with the clasp (Figure 2.4). For nanoparticle morphology observations, a few drops of the NPs dispersed in water were collected and dried on a copper grid with a carbon backing. The average particle diameter was measured directly with the line tool on the TIA/iTEM software of the FEI-T12-TEM-STEM instrument. The accelerating voltage was maintained at 120 kV.

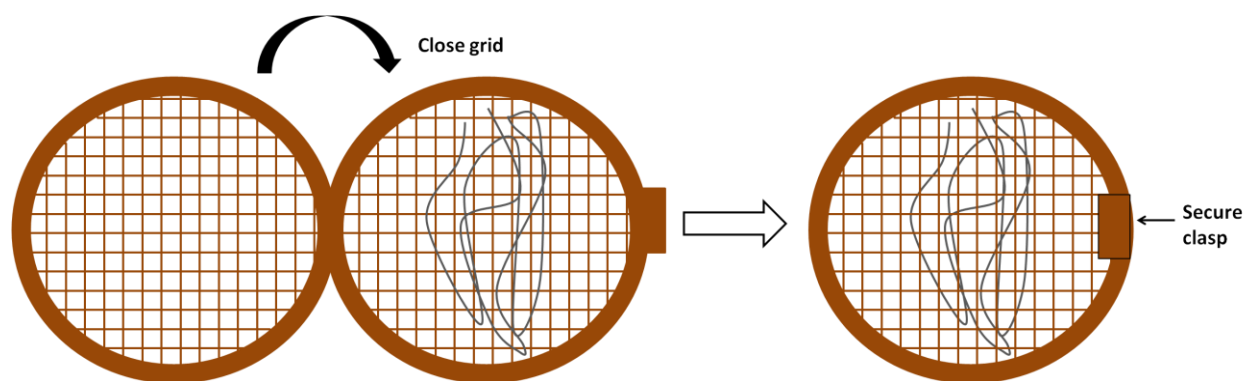


**Figure 2.4 TEM nanofiber preparation on oyster grid**

### *Fourier Transform Infrared Spectroscopy (FTIR)*

A Nicolet Magna 560 FTIR spectrometer confirmed the presence of the coupling agent on the NPs for the grafting reaction. A background was measured prior to analysis of each sample. The spectra range was  $4000\text{-}530\text{ cm}^{-1}$ , with 64 scans per run, a resolution of  $4\text{ cm}^{-1}$  and

analysis was conducted in attenuated total reflectance-Fourier transform infrared (ATR-FTIR) mode.

#### *Thermogravimetric Analysis (TGA/DTG)*

TGA was used to study how the NPs affect the thermal degradation behavior of the treated nanofibers and to confirm the presence of a polymer coating on the Fe<sub>3</sub>O<sub>4</sub> NPs. 1-4 mg fiber samples were placed on an aluminum pan, then on a platinum pan. A disposable aluminum pan was used because of the difficulty in removing metal oxide residue from platinum pans. TGA was performed with a heating rate of 10°C/min from a temperature of 30°C to 500°C for the nanoparticle treated nanomembranes and up to 550 °C with the raw nanoparticle samples. The nitrogen flow rate was set at 40 ml/min. Each sample was run at least two times for reproducibility.

#### *CIELAB Color System*

The MacBeth Color Eye 2020+ spectrophotometer was used to quantitatively measure the nanoparticle uptake by color change on the nanofiber membranes for the electrospray, layer-by-layer, and grafting treatments. It uses the CIELAB 3D color coordinate system with a standard daylight source D65 (Figure 2.5). The scale can model color perception of human vision. L\* values range from 0 (black) to 100 (white) representing the lightness/darkness of a material. The a\* axis represents red in the positive direction and green in the negative direction. The b\* axis represents yellow in the positive direction and blue in the negative direction. Color change interpretation was based on the  $\Delta L^* \Delta a^* \Delta b^*$  values of the treated samples. A negative  $\Delta L^*$  signifies darkening, positive  $\Delta a^*$  signifies more redness, and positive  $\Delta b^*$  signifies more yellowness. The magnitude of color change on membranes treated with CA-Fe<sub>3</sub>O<sub>4</sub> NPs was

measured with respect to a pristine 20 wt% Nylon 6 sample. At least two areas of the membranes were evaluated for the three methods for reproducibility of results.

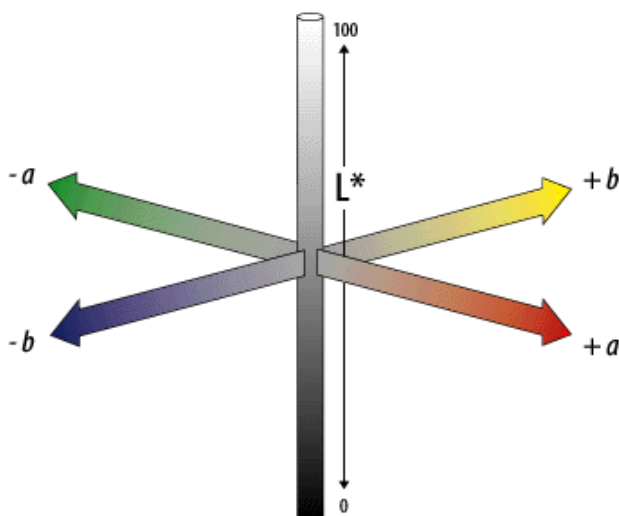


Figure 2.5 CIELAB 3D color coordinate system<sup>88</sup>

### *Zeta Potential*

Zeta potential charge measurements were taken of the CA-Fe<sub>3</sub>O<sub>4</sub> NPs and PEI from pH = 5 to pH = 8 with the Malvern Nano ZS zetasizer. Temperature was maintained at 25°C, a disposable folded capillary cell (DTS1060) was used, the dispersant was 5 mM NaH<sub>2</sub>PO<sub>4</sub>/H<sub>2</sub>O + NaOH/HCl for all samples, effective voltage ranged from 146 - 148 mV, the Smoluchowski approximation automatically calculated electrophoretic mobility of the solutions to produce zeta potential values. Three trials were conducted per sample.

### *UV-Vis Spectrometry*

The UV-Vis Lambda 35 spectrometer (Perkin-Elmer) was useful to evaluate the nanoparticle uptake on the nanomembranes with the layer-by-layer method. After each dipping cycle 2 mL aliquots of NP solution for UV-Vis analysis. Agglomerated samples were redispersed by sonication.

## CHAPTER 3: RESULTS & DISCUSSION

### Optimization of Upscaled Electrospinning Set-Up

The fiber morphology was monitored as adjustments were made to the electrospinning system. The electrospinning conditions and major adjustments that were made are shown in Table 3.1. SEM images display the fiber morphology of 25 wt% Nylon 6 nanomembranes. Before any modifications were made to the system the nanofibers produced were round, extremely curly, and semi-uniform with diameter sizes of  $453 \pm 110$  nm (Figure 3.1). Figure 3.2 shows nanofibers spun with some adjustments, such as the switch to heavy duty Al foil, the voltage was increased to 25 kV, and the use of the revised needle stand. The actuator and the insulating box had not been added yet. The fiber morphology became ribbon-like and flat with fiber diameters of  $373 \pm 56$  nm. The nanofiber diameter and its size distribution was reduced.

**Table 3.1 Electrospinning conditions along the path to optimization**

<b>Electrospinning Conditions</b>	
Voltage	17 kV (Figure 3.1) 25 kV (Figure 3.2)
Tip to Collector Distance	15 cm
Flow Rate	0.01 ml/min (Figure 3.1) 2 ml/hr (Figure 3.2)
Collector	Copper (Figure 3.1) Heavy duty Al foil (Figure 3.2)

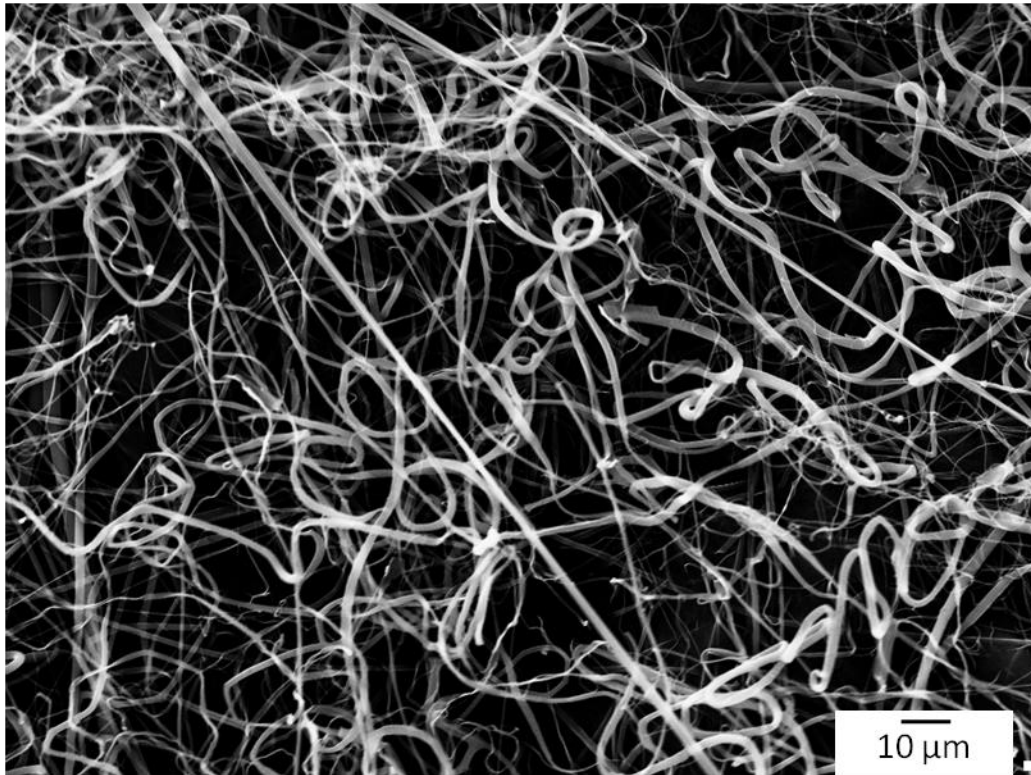


Figure 3.1 25 wt% Nylon 6 nanofibers before adjustments 1

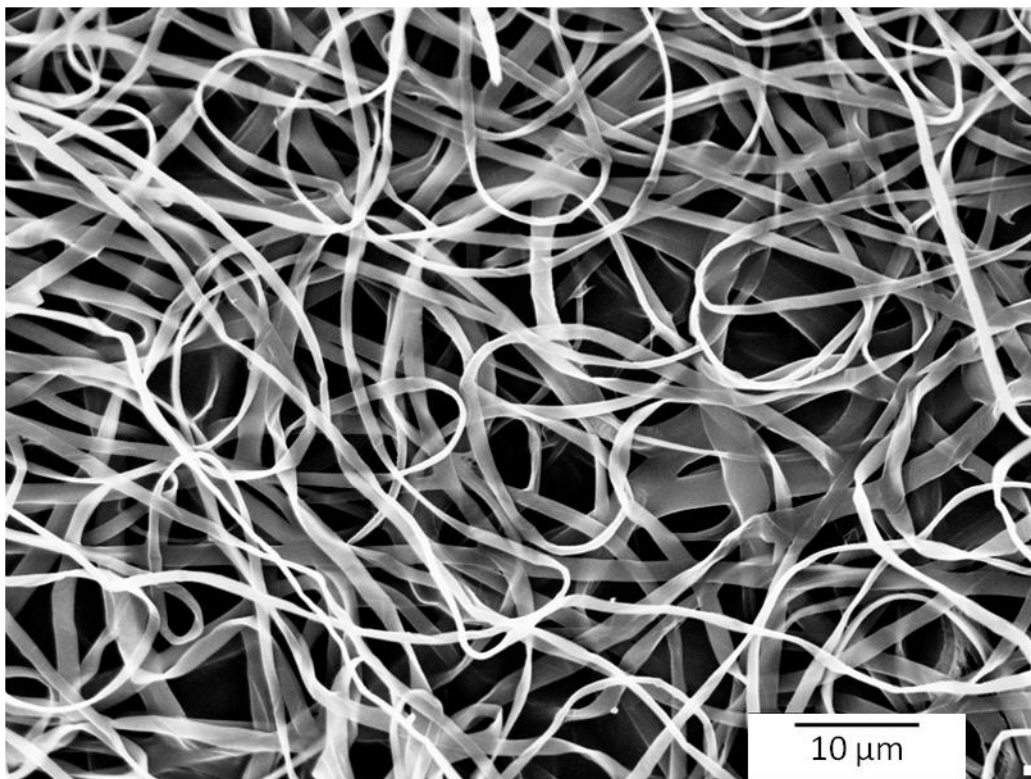


Figure 3.2 25 wt% Nylon 6 nanofibers before adjustments 2

## **Electrospinning Pristine Nanofibers**

### *Fiber Morphology*

SEM images of 20 and 25 wt% Nylon 6 with the final optimized system display smooth, round, uniform fibers with low standard error ( $\pm 5$ -10 nm depending on the polymer concentration) (Figure 3.3, Figure 3.4).

20 wt% Nylon 6 nanofibers had an average fiber diameter of  $\sim 150 \pm 5$  nm at both distances while 25 wt% Nylon 6 nanofibers had an average fiber diameter of  $300 \pm 10$  nm at 10 cm and  $400 \pm 10$  nm at 15 cm (Figure 3.5). The experimental parameter that was most sensitive in the set-up was the T-to-C distance, particularly for the lower weight % polymer solution. If the distance was too short the solvent did not have enough time to evaporate and the fibers meshed together instead of forming individual fibers. When the T-to-C distance was too far, throughput decreased as more fibers scattered in the insulation box rather than landing on the collector. 20 wt% nanofibers were used in this study since they are in a comparable size range with the NPs. No clear relationship could be made between the T-to-C distance and the final fiber diameters.

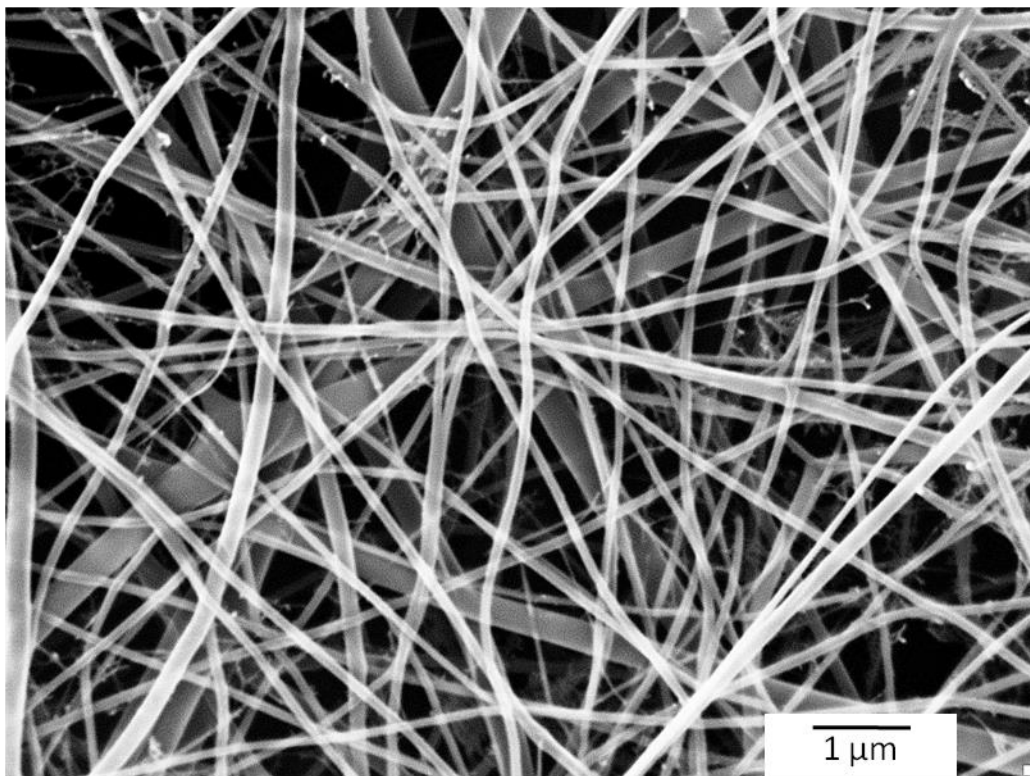


Figure 3.3 20 wt% pristine Nylon 6 nanofibers at 10 cm T-to-C distance

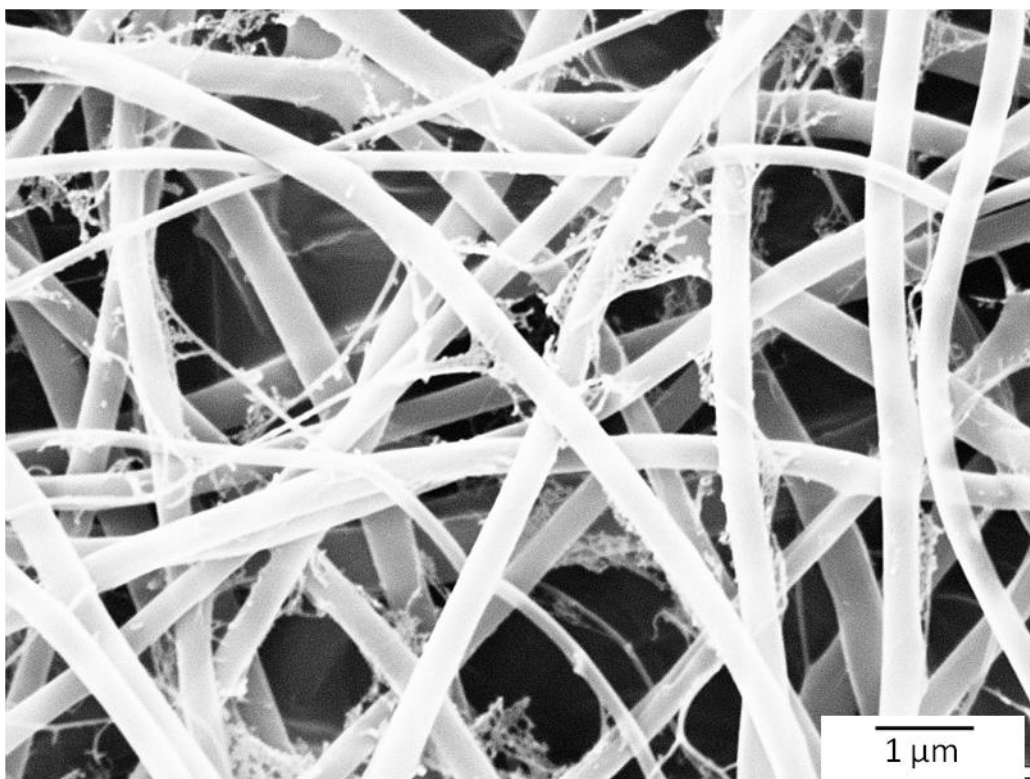
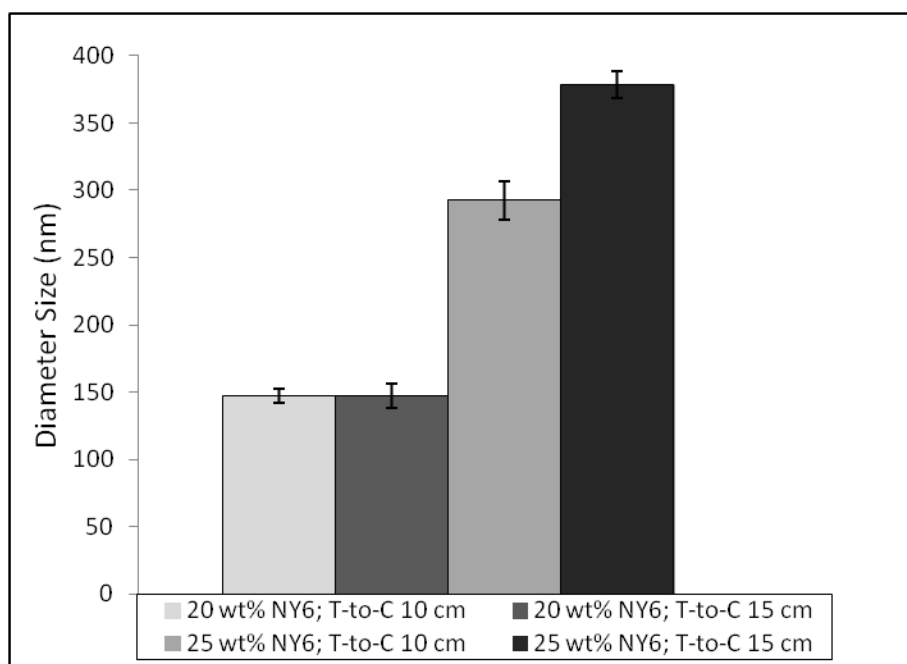


Figure 3.4 25 wt% pristine Nylon 6 nanofibers at 15 cm T-to-C distance



**Figure 3.5 Average nanofiber diameters based on varying T-to-C distances**

Spider-like, nanonet networks appear throughout the morphology of Nylon 6 nanomembranes. These networks have been observed with the Nylon 6 polymer as well as other polymers in previous studies.<sup>89</sup> Briefly, there are three proposed mechanisms for nanonet formation. The first is that the charged polymer droplets phase separate. Electrostatic and Coulombic forces cause the droplet to deform into a thin film as it approaches the collector. The thin film may contain an uneven distribution of polymer and solvent, so in the areas of concentrated solvent, evaporation rapidly occurs and the pores form resulting in the nanonet substructure.<sup>29</sup> Tsou et al suggests a second mechanism in which smaller jets simultaneously bind and intertwine with the dominant whipping jet as it approaches the collector during electrospinning. The pores characteristic of the nanonet network form once the solvent evaporates.<sup>30</sup> The third proposed explanation suggests that nanonets form due to intermolecular hydrogen bonding between protonated  $-NH_2$  and  $C=O$  groups in Nylon 6 nanonets and the nanofibers.<sup>90-91</sup> The low boiling point and high dielectric constant properties of formic acid also make it a good solvent for fine nanonet formation.<sup>92</sup>

## Nanoparticle Characterization

### *Nanoparticle Morphology*

TEM confirmed the colloidal shape and monodispersity of the CA-Fe<sub>3</sub>O<sub>4</sub> NPs (Figure 3.6). The average particle sizes were found to be  $15.18 \pm 0.95$  nm. The nanoparticle size distribution was determined based on a sample size of 200 (Figure 3.7).

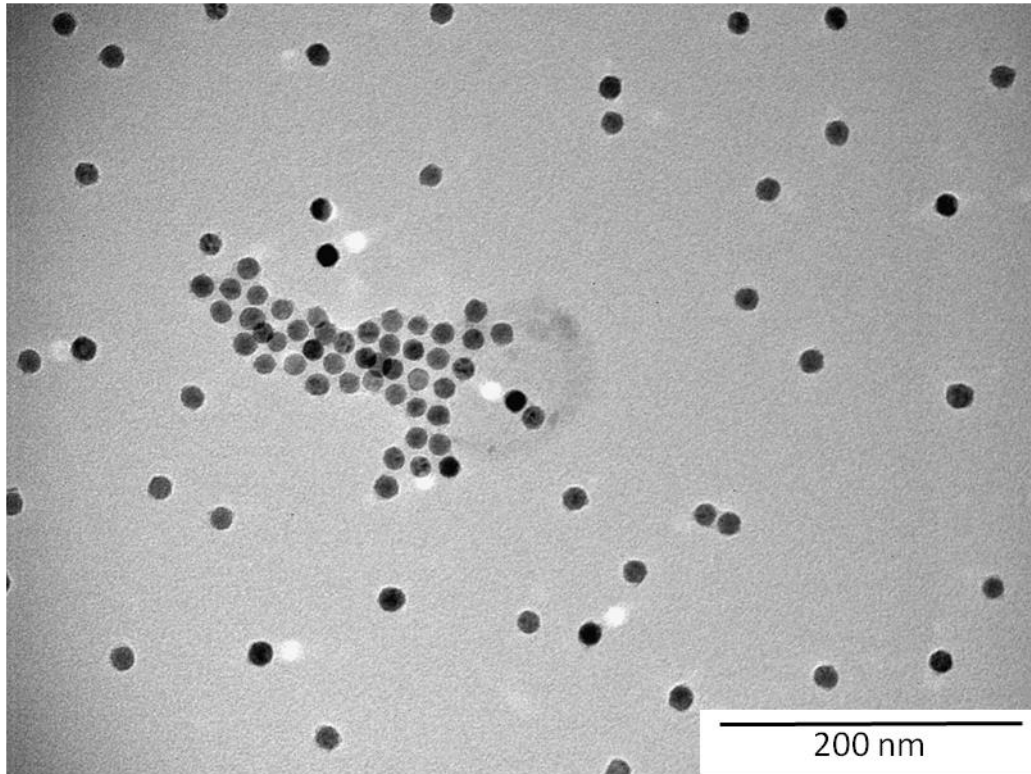


**Figure 3.6** TEM image of CA-Fe<sub>3</sub>O<sub>4</sub> NPs dispersed in DI-H<sub>2</sub>O

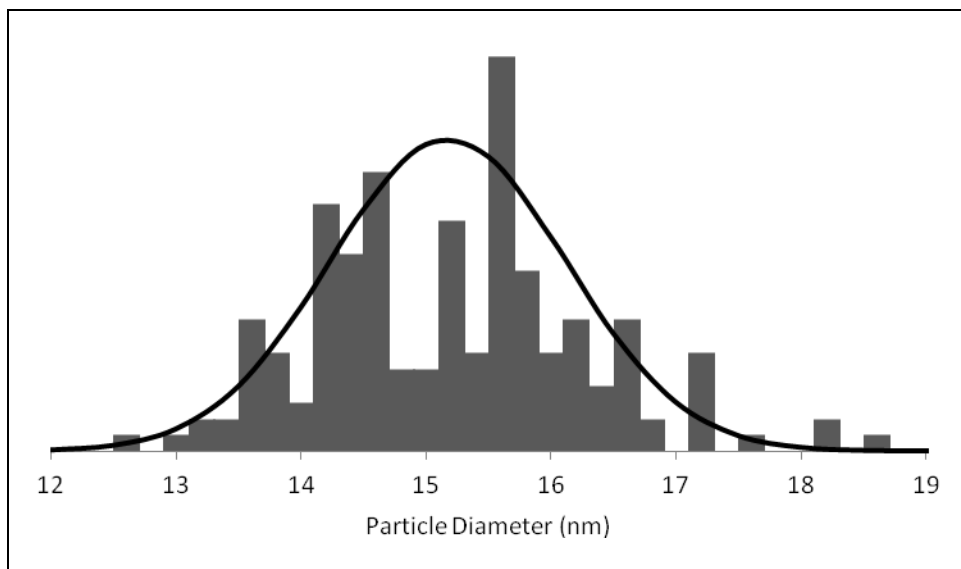


**Figure 3.7** Distribution histogram displaying average particle diameter of CA-Fe<sub>3</sub>O<sub>4</sub> NPs

### *EDX Analysis*

EDX confirmed that the NPs are composed of iron (Figure 3.8). Characteristic X-ray emissions of iron were detected at 0.7 keV from L alpha, 6.4 keV from K alpha, and at 7.1 keV from K beta X-rays. L and K represent inner shells in which electrons have been lost and replaced by electrons from outer shells (higher energy electrons into lower energy shells;  $M > L > K$ ). The presence of copper in the scan is attributed to the grid used for sample preparation and the silicon peak was from an impurity already in the system.

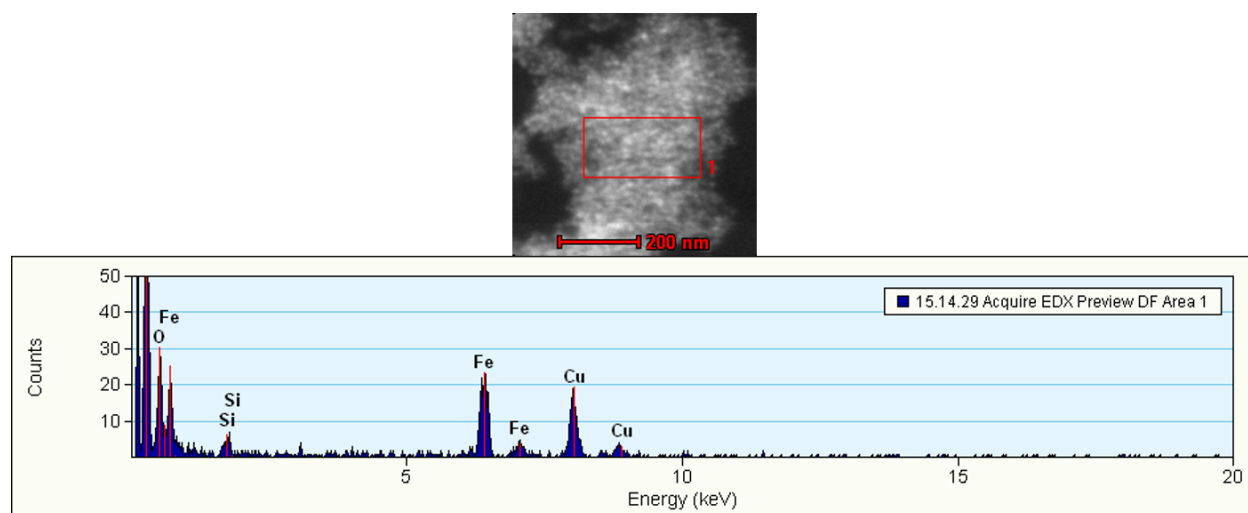


**Figure 3.8** Dark field image and EDX scan of NPs

### FTIR Analysis

FTIR analysis confirmed the carboxylic acid functional groups on the magnetite NPs (Figure 3.9). The sample displayed absorbance in the regions 3380, 2920, 2850, 1690, 1540, 1400 and 575  $\text{cm}^{-1}$ . The broad IR band at 3380  $\text{cm}^{-1}$  is attributed to  $-\text{OH}$  stretching from the organic coatings on the particles. Sharp alkyl C-H stretches ( $\text{sp}^3$ ) appear at 2920 and 2850  $\text{cm}^{-1}$ .<sup>93</sup> 1680  $\text{cm}^{-1}$  is assigned to the carboxylic acid carbonyl stretch from the polymeric coating on the particles. A shift toward a lower wavenumber for the carbonyl stretch indicates chemical bonding between the nanoparticle surface and the organic layers.<sup>27, 94</sup> At approximately 1400  $\text{cm}^{-1}$  and 1540  $\text{cm}^{-1}$  vibrations from asymmetric and symmetric stretching vibrations of  $\text{COO}^-$  are apparent.<sup>95</sup> Metal-oxygen vibrations are common in the fingerprint region. The sharp band at 575  $\text{cm}^{-1}$  corresponds to Fe-O stretching vibrations at the tetrahedral sites of Fe cations.<sup>96-97</sup>

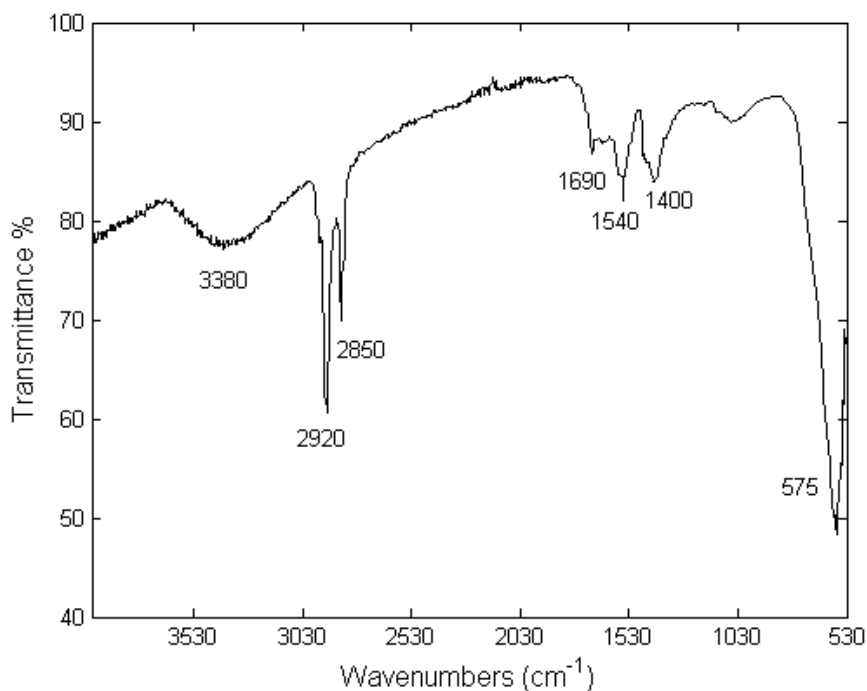


**Figure 3.9** ATR-FTIR spectra of CA-Fe<sub>3</sub>O<sub>4</sub> NPs

### TGA/DTG Analysis

The thermal degradation behavior of the organic coatings on the NPs was studied by TGA analysis. Degradation occurred in a two stages suggesting a bilayer organic structure on the particles (Figure 3.10). The NPs displayed the most significant weight loss of 1.22% at 309°C and a second weight loss of 0.58% at 399°C. The total weight loss from the organic coating on the NPs was 1.80%. Three trials were taken with similar degradation temperatures observed though the area of the derivative peaks varied.

Compounds that are directly bound to the particle surface have high binding strength and tend to desorb at higher temperatures.<sup>98</sup> Zhang et al have shown that the degradation of –COOH polymeric compounds on nanoparticle surfaces undergo desorption in one step.<sup>79</sup> This suggests that two distinct coatings exist.<sup>79</sup> The 399°C degradation temperature may belong to the tightly bound surfactant, the oleic acid capping group, which was specified by Ocean NanoTech (Figure 3.11). The peak at 309°C can be attributed to the carboxylic acid polymer as the outermost layer having a lower binding strength to the metal core.

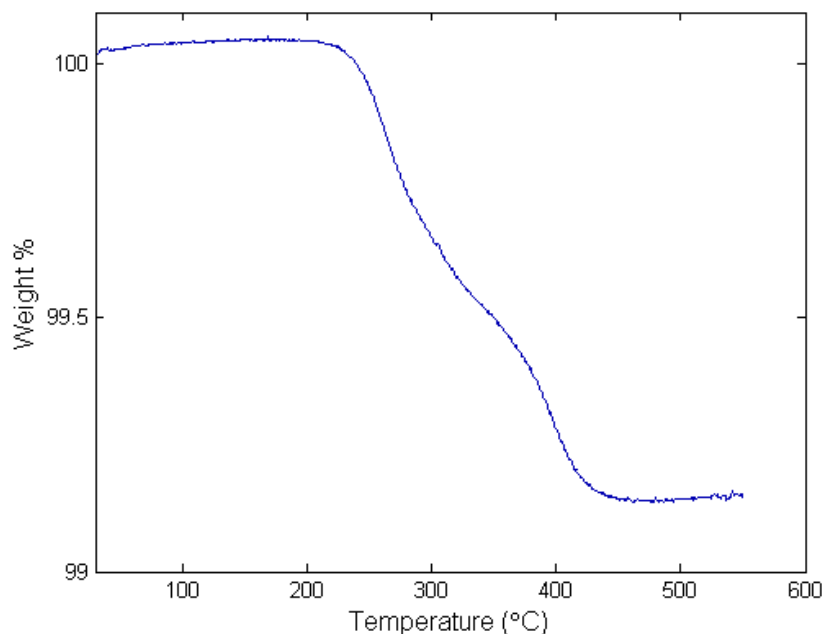


Figure 3.10 TGA curve of raw CA-Fe<sub>3</sub>O<sub>4</sub> NPs

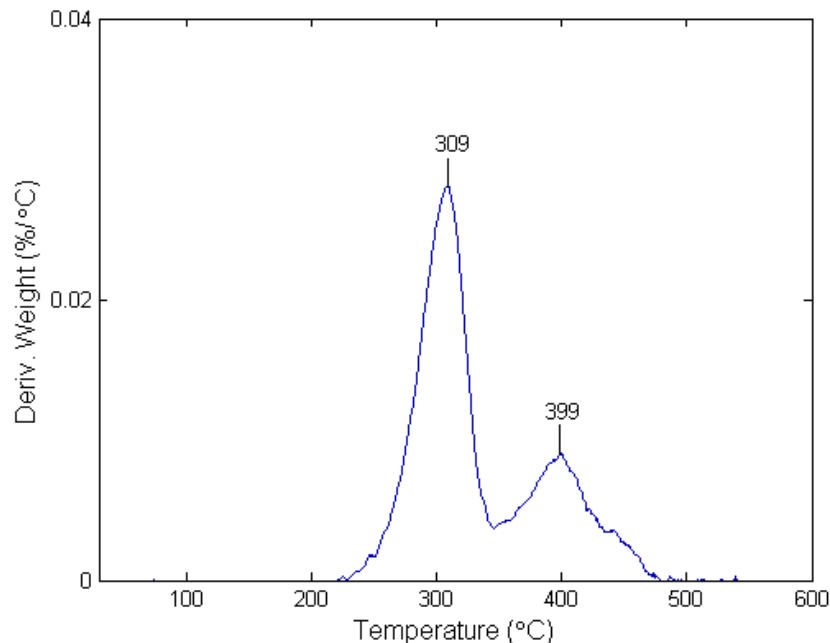
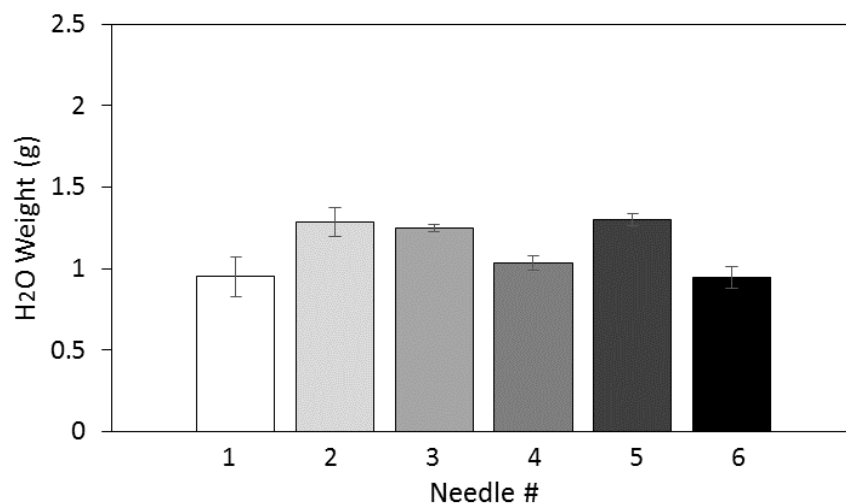


Figure 3.11 DTG curve of raw CA-Fe<sub>3</sub>O<sub>4</sub> NPs

### Initial characterization - Electrospayed NPs on fibers

#### *Optimization of Electrospay System*

Key results from the optimization of the electrospay system will be discussed. The flow rate of the solution was the most significant parameter to optimize for consistent and reliable electrospaying from the six needle system on one side of the collector. Figure 3.12 demonstrates that the water was able to flow from the six needles consistently at a flow rate of 0.4 ml/min. With applied voltage the solution was capable of flowing consistently at a lower flow rate of 0.2 ml/min, which helped increase spraying time.



**Figure 3.12** Flow rate trials set at 0.4 ml/min. Solution above the needles for electrospaying

Figure 3.13 demonstrates homogeneous droplet dispersion with methanol spraying for 5 - 10 seconds on a stationary collector.



**Figure 3.13** Photograph of homogeneous solvent dispersion on nanomembrane with multi-jet electrospay system

Methanol was the optimal solvent for electrospaying because it dispersed into smaller droplets and more homogeneously than acetone. Table 3.2 displays some physical properties that may influence the electrospay performance observed. During electrospinning and electrospaying the jet stability depends on two factors, the surface tension ( $\gamma$ ) of the solution and its surface charge repulsion.<sup>99</sup>

**Table 3.2 Physical properties of solvents<sup>100</sup>**

<b>Solvents</b>	<b>B<sub>p</sub> (°C)</b>	<b>ε (@ 20°C)</b>	<b>γ (@ 20°C dyn/cm)</b>	<b>Conductivity (μS/cm)</b>
<b>Methanol</b>	64	32.6	22.6	0.0015
<b>Acetone</b>	56	20.6	23.3	0.005
<b>Water</b>	100	79.7	72.7	5 x 10 <sup>5</sup>

The differences in the solvent droplet dispersion may be attributed to the degree of surface charge repulsion, which determines the bending instability of the jet. Sun et al demonstrated that the dielectric ( $\epsilon$ ) properties and the conductivity of solvents can affect bending instability of a jet. Solvents with low dielectric constants have less ‘free charge’ and low surface charge repulsion, so the jets become more stable and behave more linearly.<sup>99</sup> A jet with some bending instability is favorable for electrospraying. Methanol has a low dielectric constant, yet it is higher than acetone suggesting that methanol has the proper bending instability to produce homogeneous droplet dispersion.

The surface tensions of methanol and acetone are nearly equal in value, therefore, its influence on droplet dispersion behavior is negligible. The addition of CA-Fe<sub>3</sub>O<sub>4</sub> NPs in methanol increases conductivity (Traceable Conductivity Meter, Control Company, Friendswood, TX). The bending instability and efficient droplet dispersion can also be positively influenced by the addition of conductive, CA-Fe<sub>3</sub>O<sub>4</sub> NPs in methanol (Figure 3.14).

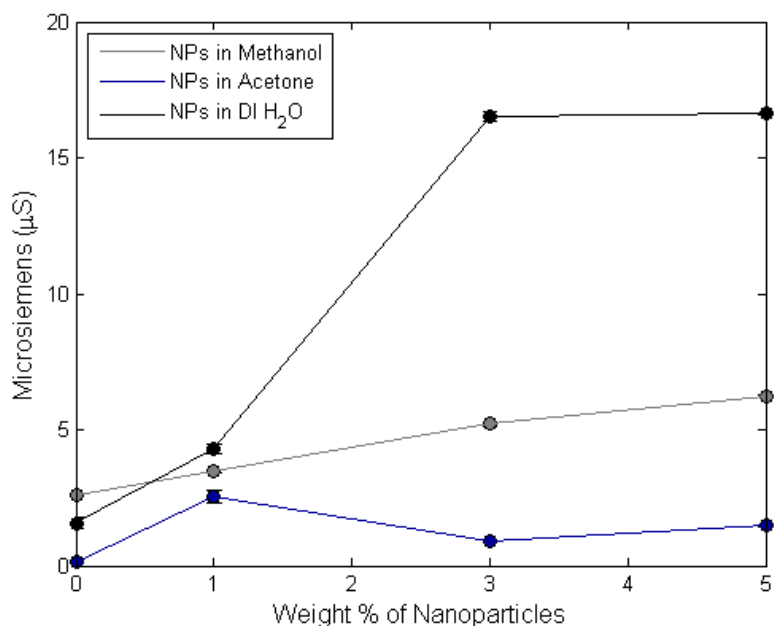


Figure 3.14 Conductivity of CA-Fe<sub>3</sub>O<sub>4</sub> NPs immersed in varied solvents

### Initial characterization - LbL Assembly of NPs on Fibers

#### *Zeta Potential*

The zeta potential of CA-Fe<sub>3</sub>O<sub>4</sub> NPs and PEI were measured to determine the pH conditions in which the alternating positive and negative surface charges were present (Figure 3.15). The NPs gain a negative charge at pH  $\geq 7$  suggesting that the optimal bath conditions for LbL assembly would lie within that pH range.

Studies conducted on 0.08 wt/vol% PEI reveal that under various pH conditions, the polymer maintains a positive charge. PEI reaches a plateau of cationic charge at a pH of 6 and 7. The zeta potential results from the NPs and PEI indicate that the desired alternating charge for LbL assembly can be achieved at pH = 7.

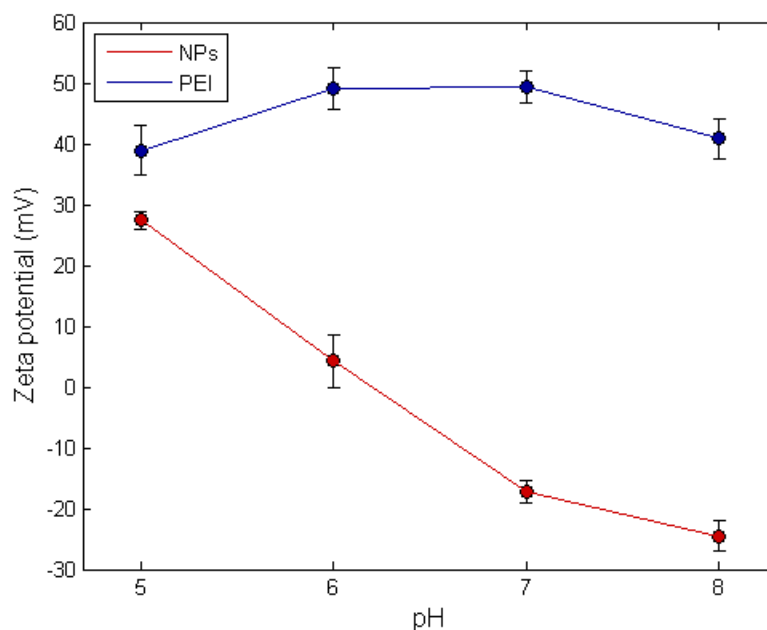


**Figure 3.15 Zeta potential of CA-Fe<sub>3</sub>O<sub>4</sub> NPs and 0.8 wt/vol% PEI at various pH ranges**

### *UV-Vis Results*

After each dipping cycle the NP uptake on the membranes was monitored from the NP solution bath by UV-Vis spectroscopy (Figure 3.16). The inset photograph shows samples taken from the NP solutions after each dipping cycle (1 – 5). Vial 0 was the control sample of 5 wt% NP solution. By visual comparison of vials 0 and 1, the most significant nanoparticle uptake appears to occur after the first layer of PEI was applied. Particle adsorption declined after cycle 1 in small increments.

Absorption bands appear in the UV region of the spectrum at 260 nm and a broad peak at 364 nm. One peak is characteristic of the size-dependent quantum effect of semiconductors below 100 nm in size (Figure 3.16). As the size of NPs decreases the HOMO-LUMO band gap increases, which causes the particles to become excited at higher energy levels and display absorption at shorter wavelengths.<sup>101-102</sup> The second peak can be attributed to conjugation from the carbonyl groups of the NP coating.

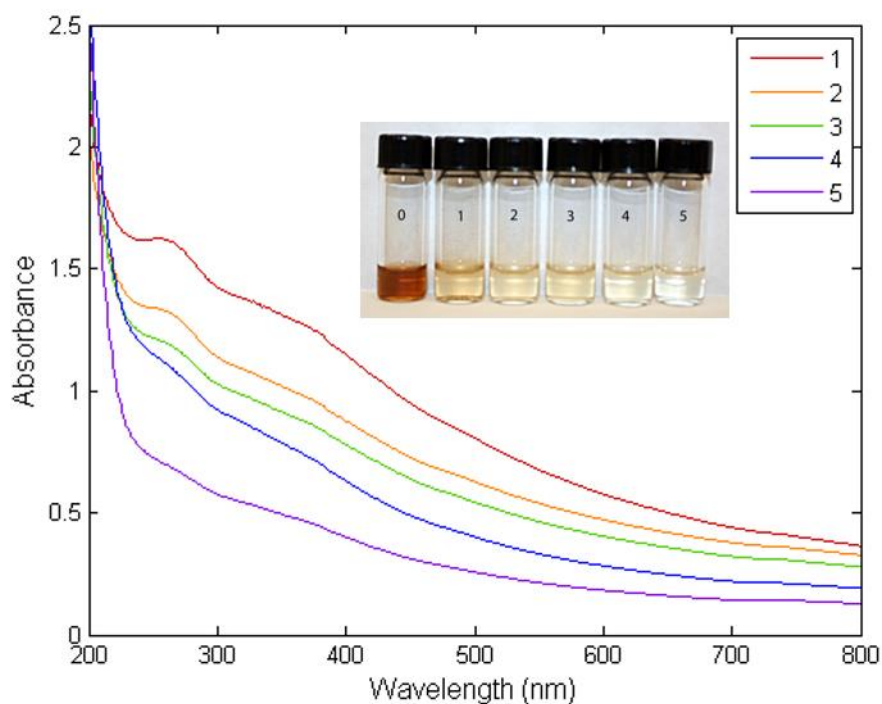


**Figure 3.16 UV-Vis spectra and photograph of NP solutions after each bilayer dip**

The lack of a continued high adsorption after the first bilayer may be caused by very low ionic strength, pH, and the combination of the bulky, branched PEI and the colloidal NPs. Other studies on multilayer growth using non-conventional polyelectrolytes, such as polysaccharides<sup>103</sup> and amino acid polymers<sup>104</sup> suggest the layer growth follows an exponential growth mechanism. The exponential growth mechanism is based on the concept that strong and weak bonds form within the films that both, hinder and introduce chain mobility. Strong bonds form at the surface of the film between oppositely charged compounds. Weak bonds form within the interior of the film that allow chains to diffuse out of the film and incoming oppositely charged chains to diffuse in.<sup>103-104</sup>

Elbakry et al who studied adsorption of PEI/DNA on Au NPs of various sizes, suggests that polymer adsorption is higher with smaller particle sizes within the size range of 20 nm to 80 nm.<sup>105</sup> Additionally, Zhou et al reported an uneven LbL assembly on dexamethasone NPs coated

with PDADMAC and PSS. TEM analysis demonstrated that a nonhomogeneous thickness is probable with linear polyelectrolytes.<sup>106</sup> The great affinity of polyelectrolytes toward NPs of smaller size can significantly affect the kinetics of the reaction and the branched/colloidal nature of the charged compounds both contribute to the nonhomogeneous distribution along the Nylon 6 nanomembrane in this study.

### **Initial characterization - Chemical Grafting of NPs on Fibers**

#### *FTIR Results*

FTIR analysis confirmed the presence of the coupling agent, sulfo-NHS, on the  $\text{Fe}_3\text{O}_4$  NPs for the grafting reaction at  $\text{pH} = 8$  (Figure 3.17). No major peaks belonging to EDC were detected. New peaks belonging to sulfo-NHS are highlighted, which match previously observed spectras.<sup>107</sup> The carbonyl stretch from sulfo-NHS appears at  $1770\text{ cm}^{-1}$  and broadens in comparison to the control. The  $1770\text{ cm}^{-1}$  peak is attributed to sulfo-NHS. Bands within the range of  $1250\text{-}1175\text{ cm}^{-1}$  correspond to the  $\text{-S=O}$  stretch and the peak at  $\sim 950\text{ cm}^{-1}$  is attributed to the  $\text{-S-O}$  stretch.  $1040\text{ cm}^{-1}$  corresponds to the amide III band of sulfo-NHS. The sample also displayed absorbance bands corresponding to prominent NP peaks discussed earlier in the regions  $3380$ ,  $2920$ ,  $2850$ , and  $575\text{ cm}^{-1}$ . This indicates that sulfo-NHS is on the surface of the NPs.

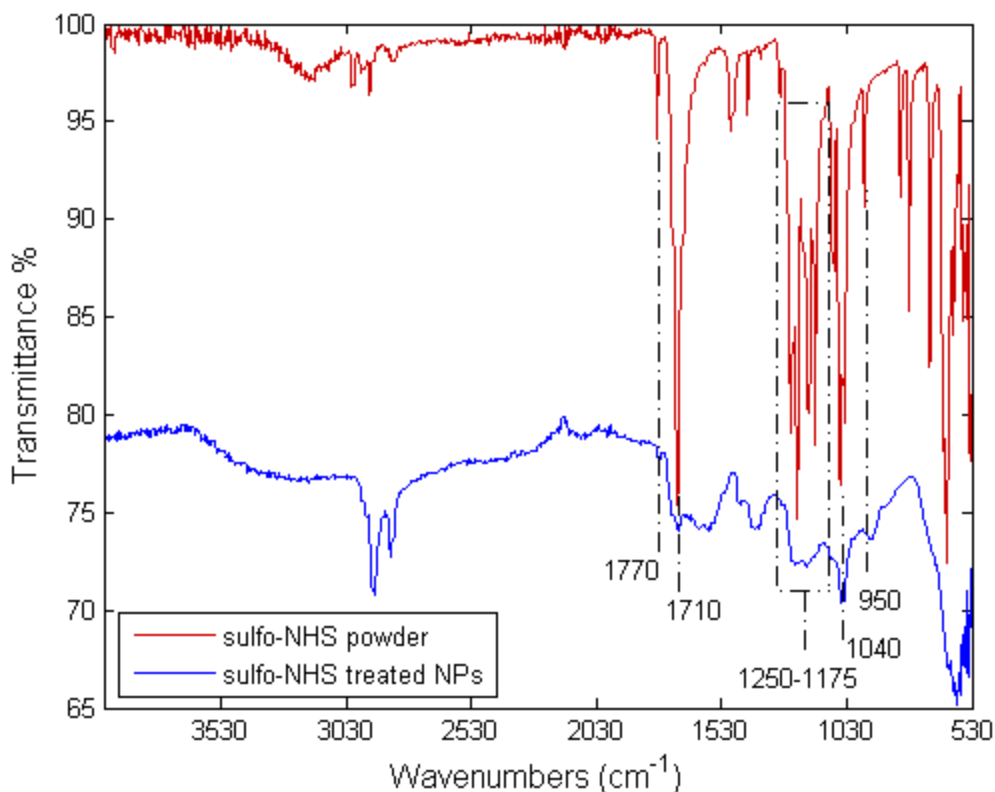


Figure 3.17 FTIR of sulfo-NHS and sulfo-NHS activated NPs

## CIELAB Control Studies

### *Nanoparticle Physical Adsorption Control Studies*

Control studies were taken to determine whether physical adsorption of the NPs on the fibers can be a competing factor in the LbL and chemical grafting reactions. 20 wt% Nylon 6 membranes were immersed and agitated in NP solutions containing 1) pure deionized water and 2) 5 mM  $\text{NaH}_2\text{PO}_4/\text{H}_2\text{O} + \text{NaOH}/\text{HCl}$  buffer solution at pH = 8.

CIELAB results reveal that physical adsorption of the NPs is time dependent. The membranes immersed, both, in DI- $\text{H}_2\text{O}$  and pH = 8 buffer did not show notable NP uptake after 10 minutes, but color change was observable after 30 and 60 minutes (Table 3.3). For all time intervals  $\Delta L^*$  became more negative,  $\Delta a^*$  became less negative, and  $\Delta b^*$  became more positive. From 10 to 60 minutes the  $\Delta L^*$  and  $\Delta a^*$  values changed by a magnitude of 1 and the  $\Delta b^*$  value

changed by a magnitude of 3. These color changes of darkening, redness, and yellowing of the samples match the tan color of the NP solutions.

**Table 3.3 Color coordinates of 20 wt% Nylon 6 dipped in control baths for various time intervals**

<b>Solution</b>	<b>Sample</b>	<b>L*</b>	<b>a*</b>	<b>b*</b>	<b>Δ L*</b>	<b>Δ a*</b>	<b>Δ b*</b>
NP/H <sub>2</sub> O	Pristine NY6	96.584	-0.250	-0.0915	n/a	n/a	n/a
	10 min	93.415	-0.4905	1.1025	-3.169	-0.2405	1.194
	30 min	92.226	-0.5165	1.538	-4.358	-0.2665	1.6295
	60 min	92.71	-0.3465	3.3895	-3.874	-0.0965	3.481
NP/pH=8 buffer	10 min	94.225	-0.564	1.837	-2.359	-0.314	1.9285
	30 min	92.745	-0.308	3.177	-3.839	-0.058	3.2685
	60 min	92.221	-0.3385	3.6435	-4.363	-0.0885	3.735

Physical adsorption of NPs would not be a significant factor for LbL assembly since the membranes are immersed in the nanoparticle solution for 5 minutes at a time. However, nanoparticle physical adhesion would be a competing factor for the grafting reaction since the minimal time allotted for the sulfo-NHS activated particles to react with the amine end groups is typically over 20 minutes.

### **Comparative Results from Three Methods**

#### ***Fiber Morphology***

##### *Electrospray Method*

TEM images of 5 wt% CA-Fe<sub>3</sub>O<sub>4</sub> NPs reveal high nanoparticle load along the length of the fibers (Figure 3.18, Figure 3.19). The electrospraying process allowed the NPs to disperse homogeneously out of solution onto the nanomembranes. Similar dispersion behavior was observed for 1 wt% and 3 wt% nanoparticle sprayed membranes.

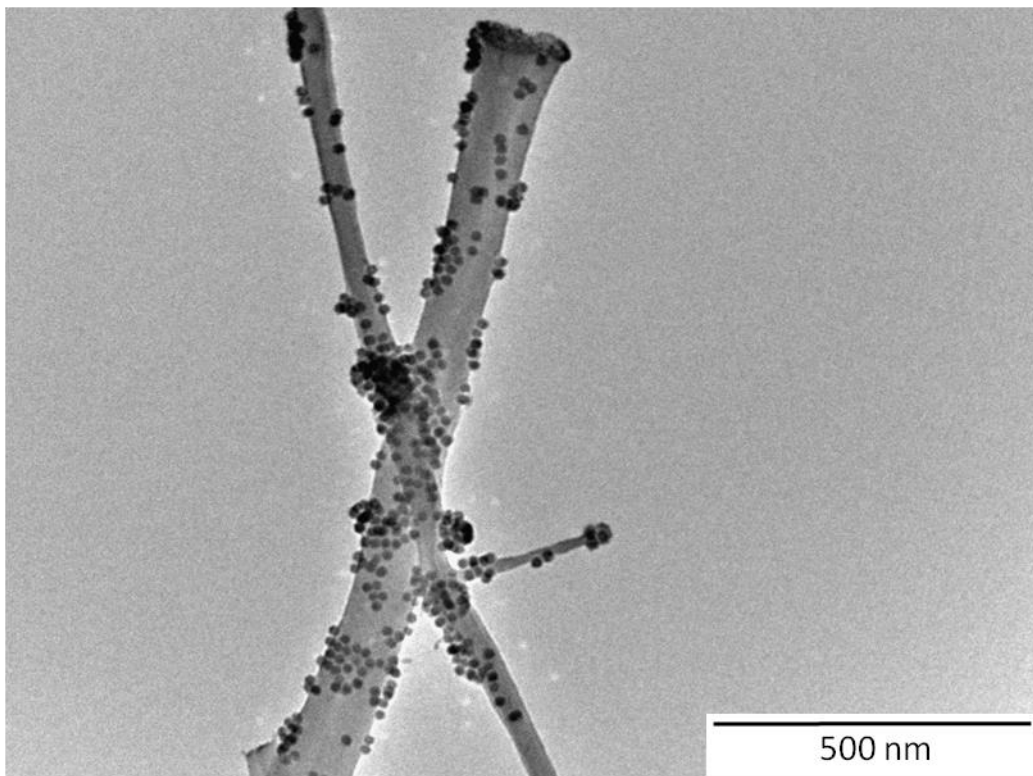


Figure 3.18 TEM image of 5 wt% CA-Fe<sub>3</sub>O<sub>4</sub> NPs sprayed on NY6

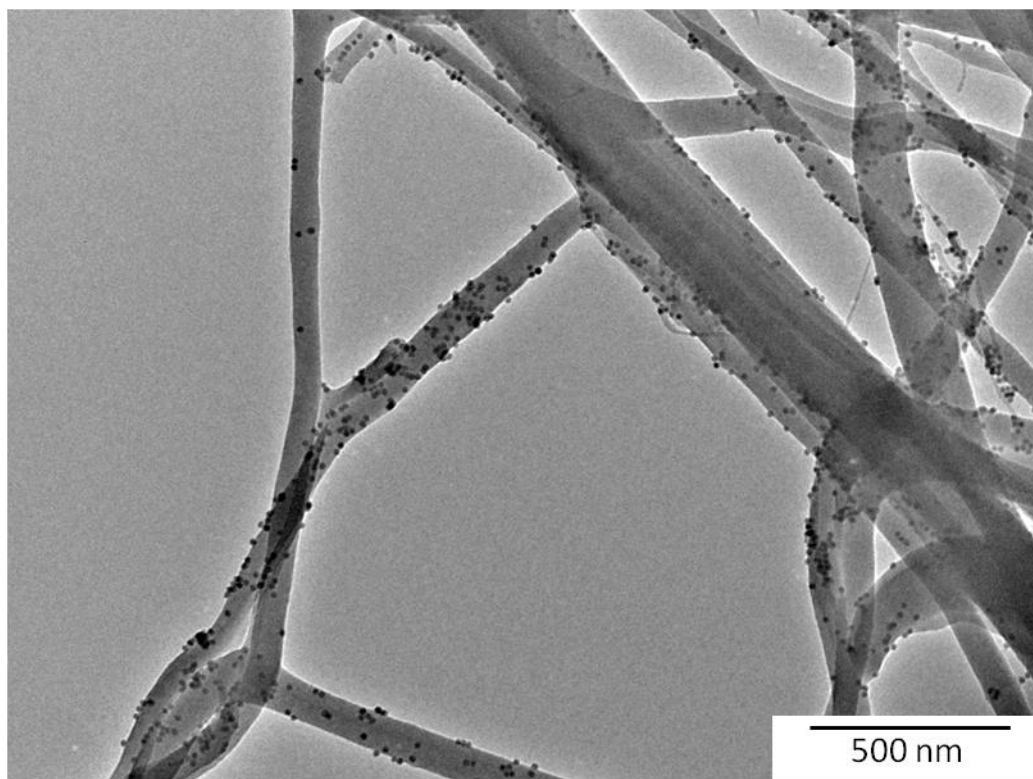


Figure 3.19 Zoomed out image of e-sprayed particles on NY6

### *Layer-by-Layer Assembly*

A SEM image of the nanomembranes treated with CA-Fe<sub>3</sub>O<sub>4</sub> NPs via the LbL method displays non-homogeneous dispersion of the NPs (Figure 3.20). The NPs concentrate in certain areas along the length of the fibers. Additionally, roughness appears in some regions of the fibers that may be an indication of PEI. The application of 5 bilayers did not introduce significant roughness to the fibers possibly because the PEI solution was very dilute and the ionic strength was very low producing very thin films. Several areas within the sample displayed similar nanoparticle behavior or absence of the NPs.



**Figure 3.20** SEM image of 5 wt% CA-Fe<sub>3</sub>O<sub>4</sub> NPs deposited via LbL assembly on Nylon 6

### *Chemical Grafting Reaction*

The FESEM image of nanofibers treated via the grafting method show homogeneous dispersion of the NPs and no aggregation (Figure 3.21). Although the nanoparticle weight % was

lower for this method the concentration did not appear to effect the total particle uptake on the fibers.

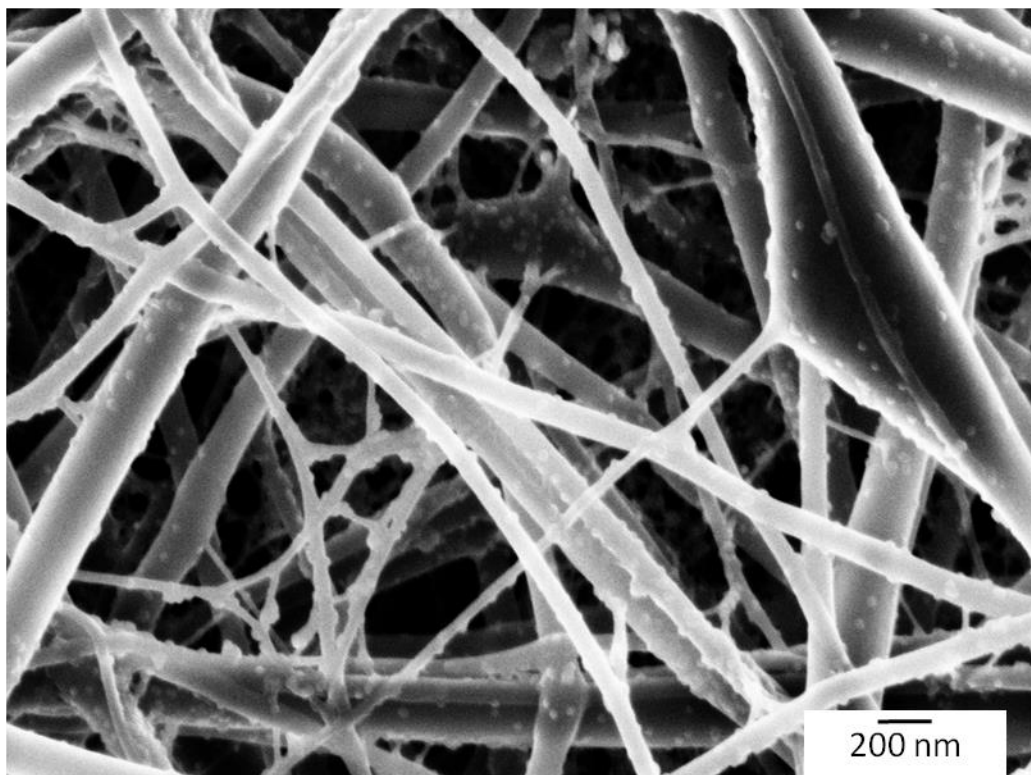


Figure 3.21 3 wt% CA-Fe<sub>3</sub>O<sub>4</sub> NPs grafted to Nylon 6 nanofibers

### ***CIELAB Results***

#### *Electrospray, LbL, and Grafting Method*

CIELAB studies were conducted to determine the homogeneity of each treatment over a larger sample area (1 x 0.5 cm<sup>2</sup>) to supplement SEM analysis at the micron scale (Table 3.4). The homogeneity of all treatment methods were evaluated in three areas of each sample.

Electrosprayed membranes with 1 wt%, 3 wt%, and 5 wt% CA-Fe<sub>3</sub>O<sub>4</sub> NPs were also examined. On the electrosprayed membranes an increase in the magnitude of color change was observed with increased NP concentration. The membranes treated via the electrospray and grafting methods displayed a similar trend. By these treatments the  $\Delta L^* \Delta a^* \Delta b^*$  values were consistent in the three areas examined, which indicates homogeneous NP dispersion on the

membranes. By the electrospray and grafting methods the samples  $\Delta L^*$  became more negative up to -6.00,  $\Delta a^*$  became slightly more positive, and  $\Delta b^*$  became significantly more positive between 7.00 and 8.00. The samples darkened, got slightly redder, and more yellow matching the tan color of the NPs.

With the grafting treatment the magnitude of color change increased nearly two-fold compared to values obtained from membranes immersed in the pH = 8 buffer solution. This suggests that a reaction occurred between the NPs and the membranes independent of the physically adsorbed NPs or ionic bonding from buffer-NP-fiber interactions.

CIELAB values for the LbL method reveal that the NP treatment was not homogeneous on the membranes. Firstly, pure PEI polymer deposited on Nylon 6 introduced a slightly darker, greener, and yellower color. On Area I the color became darker, redder, and yellower. The color change increased in magnitude on the other areas observed. For all three LbL areas examined  $\Delta L^* \Delta a^* \Delta b^*$  values were greater in magnitude than the values obtained for membranes immersed in the NP/DI-H<sub>2</sub>O control solution.

**Table 3.4 Color coordinates of NP treated membranes via electrospraying, LbL, and chemically grafted**

Treatment	Sample	L*	a*	b*	$\Delta L^*$	$\Delta a^*$	$\Delta b^*$
Electrosprayed Membranes	Pristine NY6	96.584	-0.250	-0.0915	n/a	n/a	n/a
	1wt% NP/NY6	91.4	-0.329	2.65	-5.184	-0.079	2.742
	3wt% NP/NY6	91.1	-0.336	5.07	-5.484	-0.086	5.162
	5wt% Area I	90.32	-0.082	8.80	-6.264	-0.168	8.892
	5 wt% Area II	90.758	-0.239	7.764	-5.826	0.011	7.8555
LbL membranes	5 wt% Area III	90.645	-0.216	8.078	-5.939	0.034	8.1695
	PEI on NY6	94.563	-0.285	0.1335	-2.021	-0.035	0.225
	Area I	91.299	0.330	4.313	-5.285	0.58	4.405
	Area II	88.910	0.908	6.097	-7.674	1.158	6.189
Grafted membranes	Area III	87.825	1.514	9.940	-8.759	1.764	10.032
	Area I	90.672	-0.14	7.24	-5.912	-0.236	7.3315
	Area II	89.482	1.054	8.449	-7.102	1.304	8.5405
	Area III	90.155	0.046	7.474	-6.429	0.296	7.5655

Although the CIELAB values of these methods are similar, the NPs were introduced to the membranes differently so this analytical technique cannot be used for NP load comparisons.

### ***Post-Washing Results via ICP-AES Evaluation***

#### *Electrospray Method*

The NPs deposited via the electrospraying method on the nanomembranes were affected by the washing conditions in varied pH baths (Figure 3.22). For the 10, 30, and 60 minute time intervals the lowest amount of Fe released from the fibers and into the bath occurred at pH = 4. The low release and stability of the particles on the membranes is attributed to electrostatic attractions between the fibers and particles. The Nylon 6 fibers carry a slightly electronegative charge from the amine end groups. The NPs, sprayed out of an acidic solution, may have stable carboxylic acid groups on the particle surface and carry a slight positive charge to gain electrostatic affinity to the fibers and good adherence during washing at pH = 4. At pH levels greater than 7, the amount of iron released from the membranes increases to a maximum of 0.06 ppm at 60 minutes. The carboxylic acid coated NPs become negatively charged at pH  $\geq 7$  as confirmed in zeta potential data. The formation of carboxylate groups on the particle surfaces may influence a loss of electrostatic attraction between fibers and particles at high pH to cause higher release rates into the bath overtime.

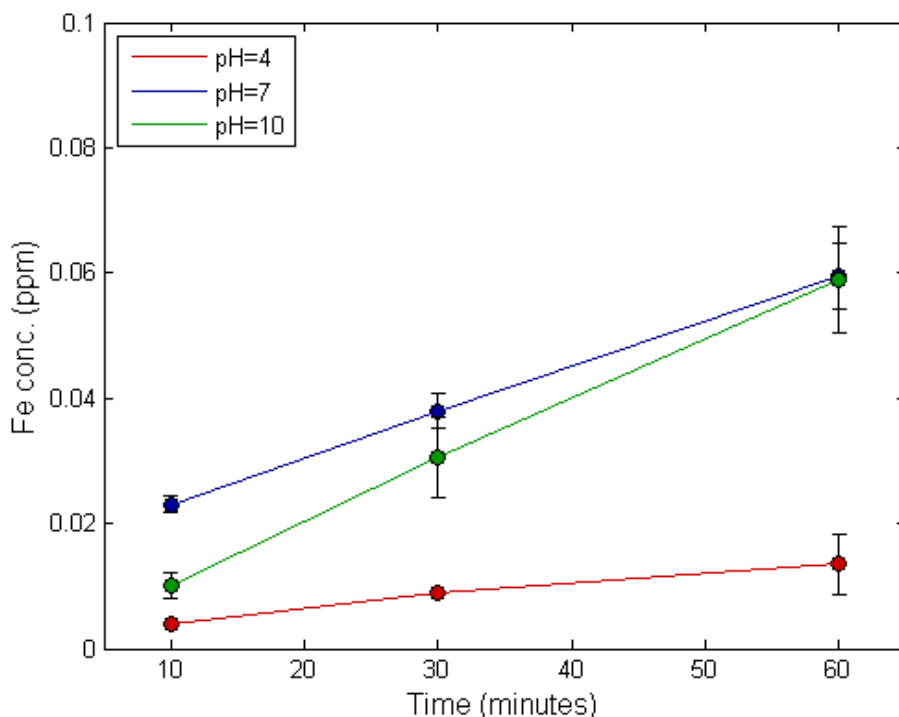


**Figure 3.22 ICP-AES results of Fe released from 5 wt% electrospayed membranes washed in varied pH baths**

#### *Layer-by-Layer Method*

ICP-AES results reveal that the different pH conditions affect the amount of NPs released overtime (Figure 3.23). A low release of Fe is observed for 10, 30, and 60 minutes at pH = 7 and pH = 10. Strong electrostatic forces can influence the good adherence of the negatively charge NPs on the membrane surfaces at high pH. Carboxylate groups on the nanoparticle surfaces remain stable and maintain strong adsorption to the cationic PEI polymer. At pH = 4 the amount of Fe released into the bath increases to a maximum of 0.08 ppm at 60 minutes. The greater release is due to protonation of the carboxylate groups on the nanoparticle surfaces and a net positive charge on the NPs at low pH. Due to a similar chemical environment between the NPs and PEI, the compounds begin repelling one another as reduce electrostatic affinity diminishes to initiate greater Fe particle release into the bath. The NP release reaches a plateau at pH  $\geq 7$  by 30 minutes.

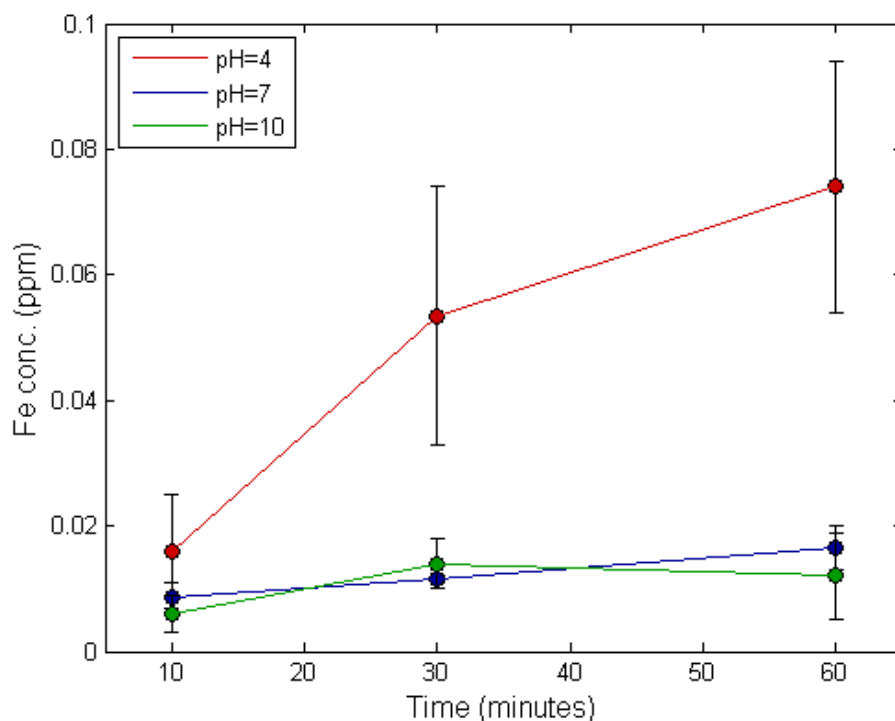


**Figure 3.23** ICP-AES results of Fe released from layer-by-layer treated membranes washed in varied pH baths

### *Chemical Grafting Method*

Results indicate nanoparticle release occurs under high pH conditions after washing the membranes prepared via the chemical grafting method (Figure 3.24). It is significant to mention that the amount of Fe released is up to three times more than LbL and electro spray methods at 60 minutes. Although the grafting conditions were optimized to minimize ionic bonding and hydrogen bonding between NP-to-NP and NPs-to-fibers these chemical bonds are still present under the pH = 8 buffer environment. High particle release can be due to various type of chemical bonds in addition to covalent bonding. However, ICP-AES results reveal lower particle release at pH = 4, an acidic environment, potentially due to induced dipole-dipole and hydrogen bonding between the carbonyl groups along the Nylon 6 polymer backbone and the sulfo-NHS ester activated NPs. The highest NP release was observed at pH = 10 because the non-covalently

bonded, oxygen-rich NPs gained repulsive forces against the Nylon 6 carbonyl groups to initiate release. The NP release plateaus at pH = 4 by 30 minutes.

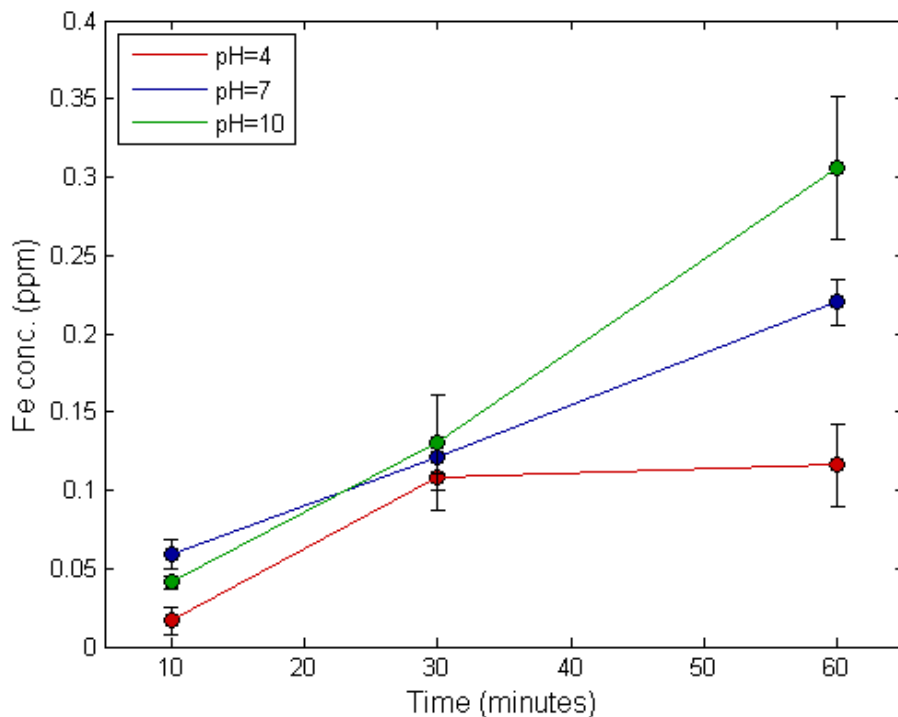
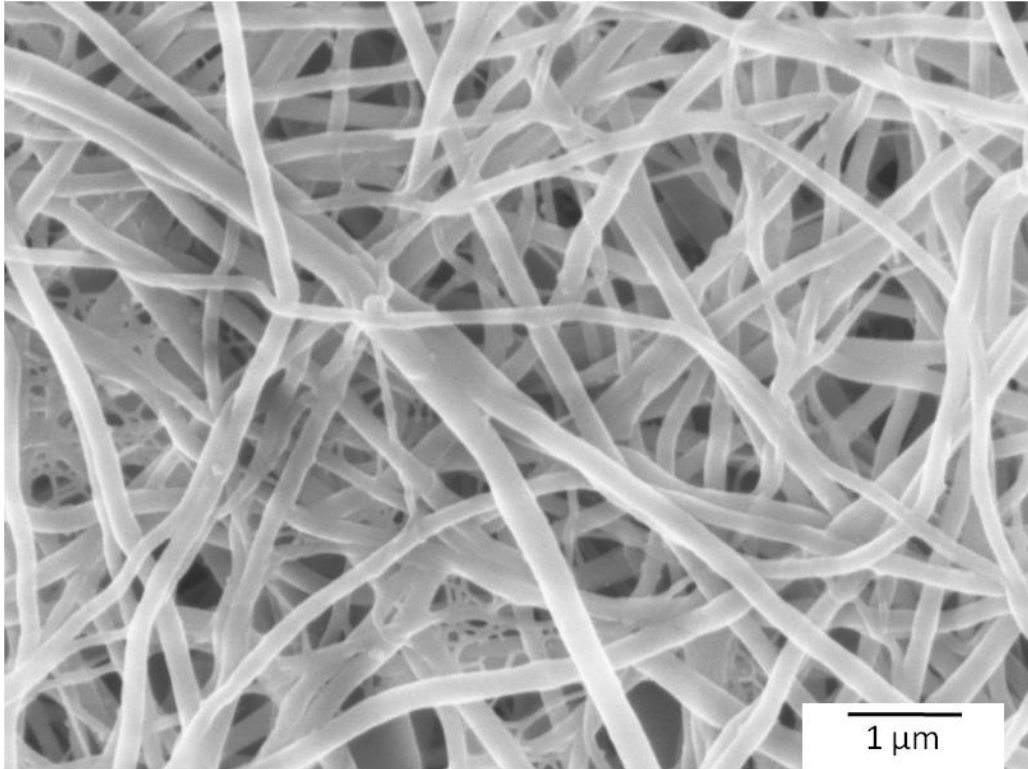


Figure 3.24 ICP-AES results of Fe released from grafted membranes in varied pH baths

### ***Post-Washing Results via FESEM Image Evaluation***

#### ***Electrospray Method***

The 5 wt% NP electrospayed membranes washed at  $\text{pH} \geq 7$  released the highest amount of Fe, therefore, samples immersed in  $\text{pH} = 10$  baths for 60 minutes were examined. The FESEM image reveals that the fibers maintain a round, uniform morphology at a pH level of 10 (Figure 3.25). Upon closer observation some NPs can be observed. The presence of NPs was further evaluated by CIELAB.



**Figure 3.25 Post-washed electrospun Nylon 6**

#### *Layer-by-Layer Method*

The membranes washed at  $\text{pH} = 4$  released the greatest amount of Fe via the LbL method, therefore, samples immersed in  $\text{pH} = 4$  baths for 60 minutes were examined. The FESEM image shows that the fiber morphology remains intact after washing (Figure 3.26). Additionally, NPs are present throughout the sample.

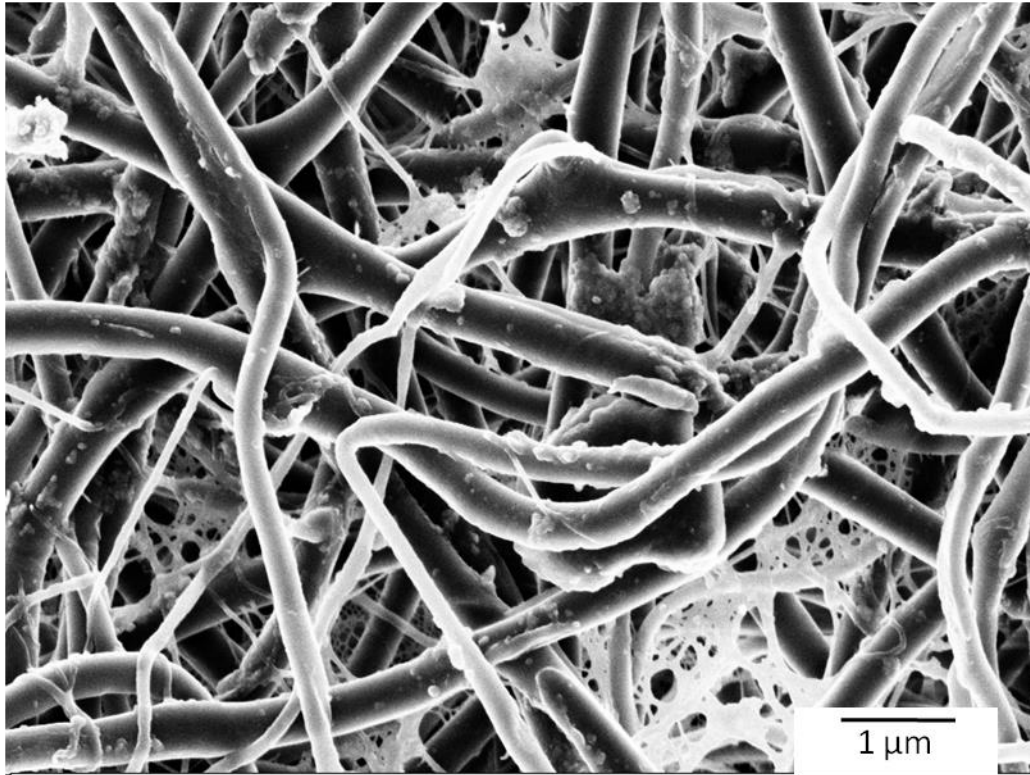
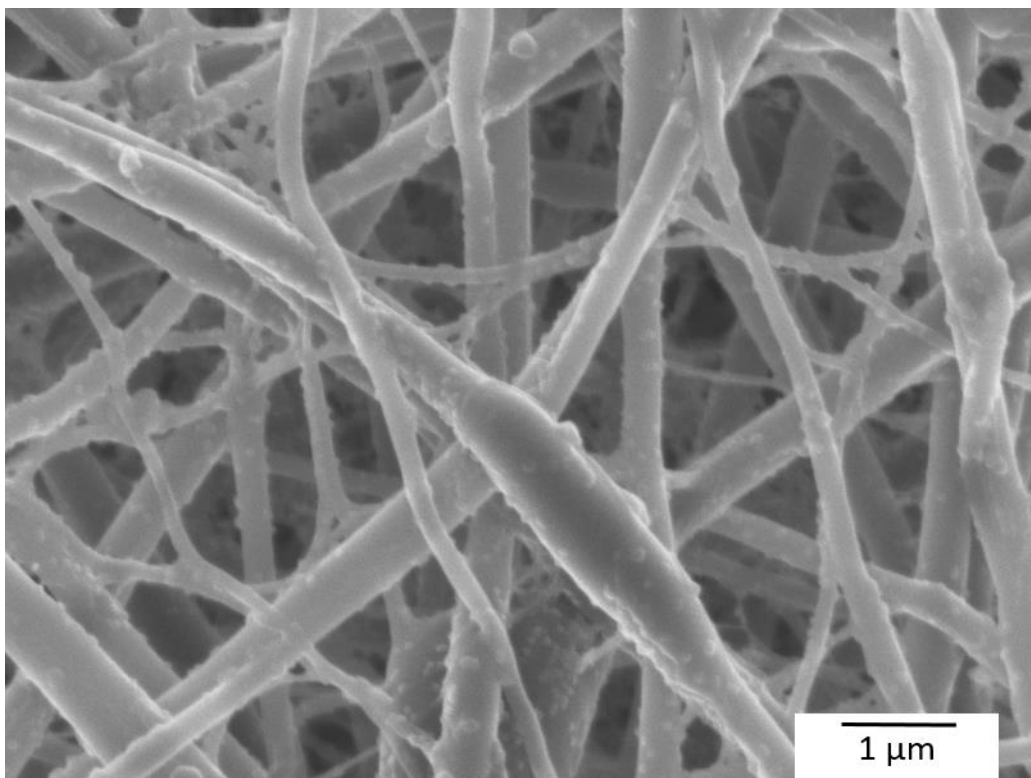


Figure 3.26 Post-washed LbL treated Nylon 6

#### *Chemical Grafting Method*

The membranes washed at  $\text{pH} = 10$  released the greatest amount of Fe via the chemical grafting method, therefore, samples immersed in  $\text{pH} = 10$  baths for 60 minutes were examined. The FESEM image confirms an unchanged, round, uniform fiber morphology (Figure 3.27). NPs appear to still be present in the washed sample.



**Figure 3.27 Post-washed grafted Nylon 6**

### ***Post-Washing Results via CIELAB Evaluation***

The tan color on the nanomembranes in the post-washing experiments indicates that NPs are still significantly present on all the nanomembranes. The same post-washed samples used for FESEM analysis were evaluated via CIELAB.

### ***Electrospray, LbL, Grafting Methods***

Comparative analysis of the CIELAB values before and after washing the electrosprayed membranes suggests that an observable amount of NPs were released (Figure 3.28). The membranes became lighter and less yellow by a greater magnitude in color change compared to the grafted membranes (Figure 3.30).

These results deviate from the NP release observations from ICP-AES. ICP-AES results displayed low NP release from electrosprayed membranes and highest NP release from the grafted membranes. The deviation can be attributed to the NP deposition process and the

ColorEye Spectrophotometer only detects color at the surface of the material. The NPs were introduced three-dimensionally by the electrospin/spray method throughout the thickness of the membrane while the NPs were applied as a surface treatment with the grafting method. The level of NP saturation on the grafted membranes can contribute to the color consistency before/after washing.

The magnitude of color change on the LbL membranes changed observably and can be attributed to the non-homogeneity of the treatment (Figure 3.29).

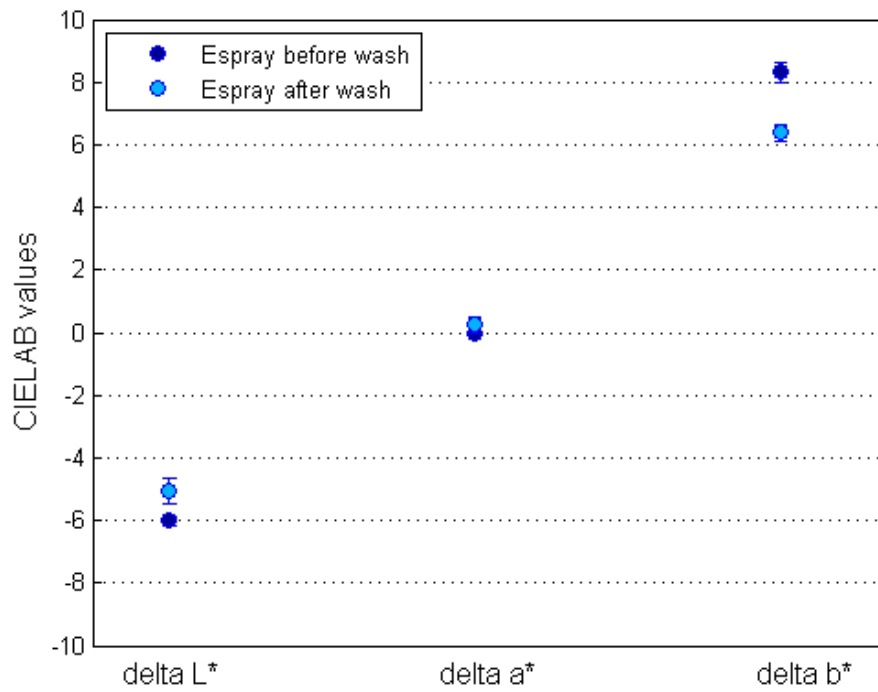
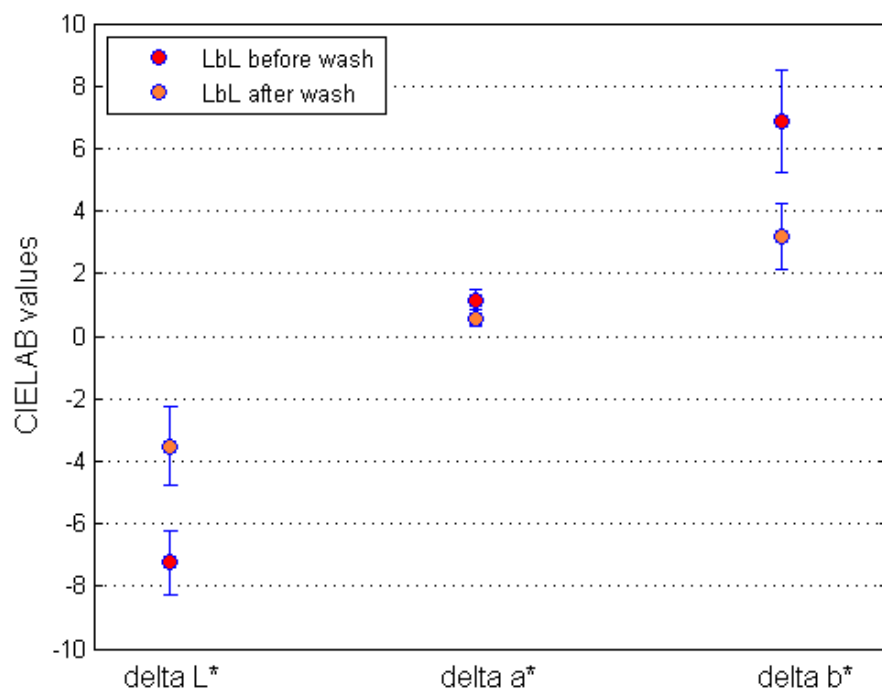
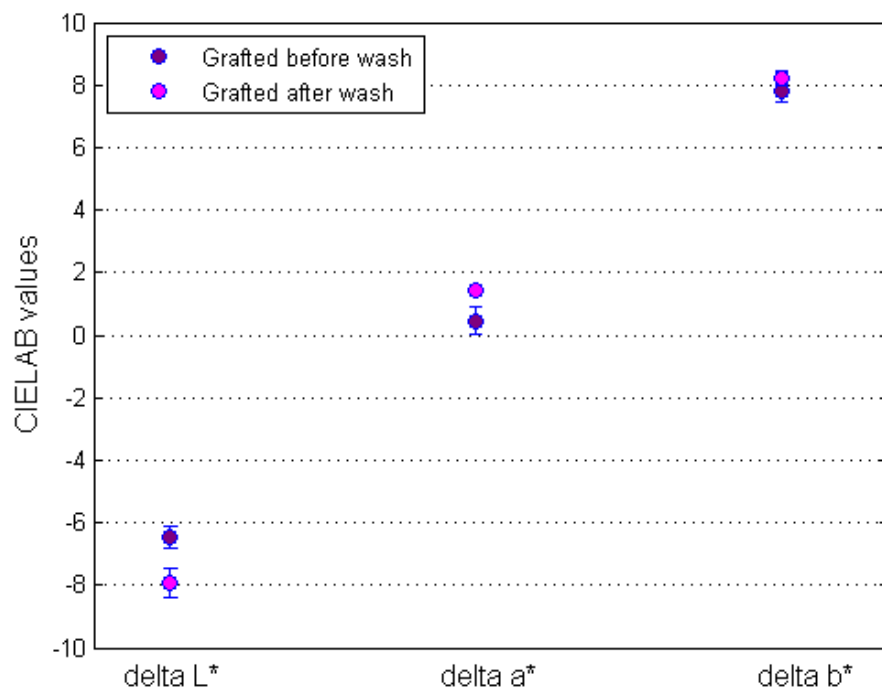


Figure 3.28 Electrospayed membranes with highest Fe release before/after washed



**Figure 3.29** LbL membranes with highest Fe release before/after washed



**Figure 3.30** Grafted membranes with highest Fe release before/after washed

## TGA/DTG Results

Overall based on DTG results, the nanoparticle treatment reduces the thermal stability or has no significant effect on Nylon 6 (Figure 3.31). Several samples were run to determine the thermal degradation of Nylon 6 occurs in a temperature range between 442°C to 457°C. The thermal degradation temperature of membranes treated with NPs via electrospraying, LbL assembly, and chemical grafting varied between 431°C to 452°C. An overlap of 10°C exists between the degradation temperatures of the nanoparticle treated and pristine Nylon 6 samples, therefore, there may be no significant effect on thermal stability within that range.

The reduction in the degradation temperature of polyamides may be due to perturbation of the polymeric chain from iron ions or particles.  $\text{Fe}^{3+}$  ions in  $\text{Fe}_3\text{O}_4$  can cause lower thermal stability of the Nylon 6 polymer because of a loss of van der waal interactions between the polymer chains or the formation of a coordinate bond between  $\text{Fe}^{3+}$  and the oxygen of the amide's carbonyl group and/or a coordinate bond between  $\text{Fe}^{3+}$  and N-H of Nylon 6.<sup>108-109,110</sup> Several studies also indicate that the  $\text{Fe}^{3+}$  ion may have a catalytic effect on the degradation of polyamides, interfering with its crystallization because of disruption in the hydrogen bonded network.<sup>111-112, 113</sup> Although some researchers may argue that a hydrogen bond network between NPs and polymers improves the thermal stability of thermoplastic polymers, the disruption from the iron ions eventually occurs throughout the polymer chain.

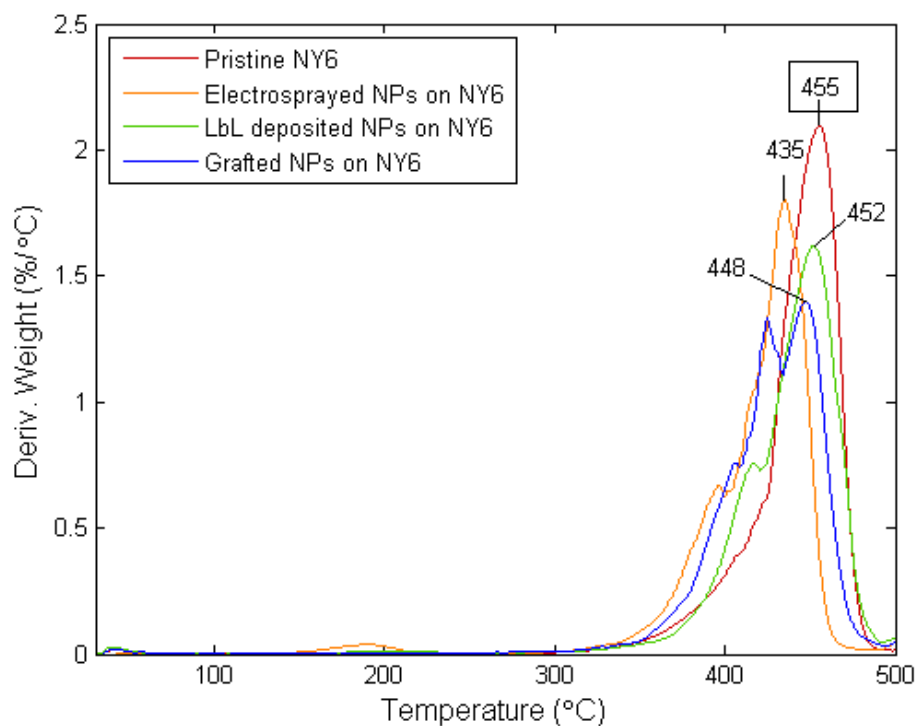


**Figure 3.31 DTG graph of pristine Nylon 6 and CA-Fe<sub>3</sub>O<sub>4</sub> NP treated Nylon 6**

The TGA curve for the pristine Nylon 6 and the NP treated membranes displays one step degradation (Figure 3.32). The thermal degradation of the electrospayed Nylon 6 sample was altered the most significantly due to the absence of bonds stronger than van der Waals and hydrogen bonding in the treatment. The weight loss % varied greatly between sample runs, so the NP loadings were not analyzed quantitatively by TGA.

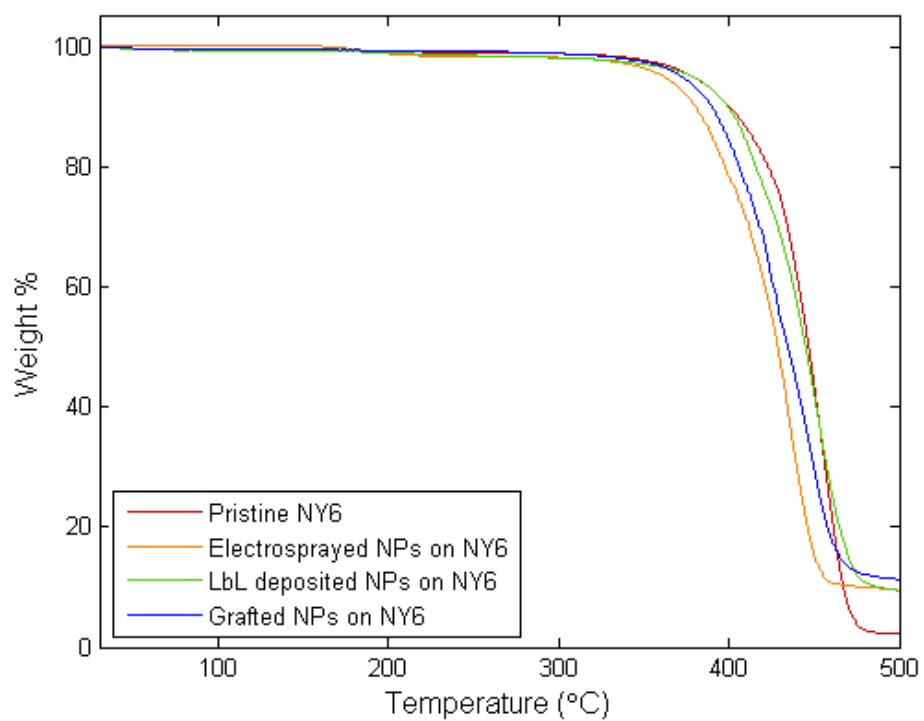


**Figure 3.32 TGA curves of pristine Nylon 6 and CA-Fe<sub>3</sub>O<sub>4</sub> NP treated Nylon 6**

## CHAPTER 4: CONCLUSIONS

In comparing the three preparation methods, the electrospray and grafting method are the simplest based on NP loading, good dispersion and homogeneity on the fibrous membranes. Although the NPs are weakly bonded to the membranes via the electrospray method, the particles become physical trapped in the fiber matrix. The entrapment makes them difficult to wash away. Chemical grafting is also viable method to load NPs on the fiber surface, however, further studies are needed to confirm covalent bonding since washing results indicating other types of bonding is occurring. LbL assembly could not provide homogeneous NP distribution, so it will not be studied further.

ICP-AES results displayed NP release from all three methods based on a play of electrostatic and intermolecular forces between the treated membranes and pH environment. NPs incorporated via the electrospray and grafting method released the least NPs at low pH and the LbL method had the lowest particle release under neutral and high pH conditions. Quantitatively, the grafting method exhibited the highest NP release of the three methods, which indicated that other molecular forces beyond covalent bonding were present.

CIELAB post washing results suggest that NPs were still present on the membranes that release the highest Fe with all methods. In comparing the CIELAB values of the membranes before and after the washing treatment, the membranes prepared by the electrospray method had an observable color loss while no color loss was observed on the grafted membranes. These results are not consistent with ICP-AES studies and it highlights a limitation of the CIELAB studies.

It was not clear whether the NP treatment had a significant effect on the thermal properties of Nylon 6.

## **CHAPTER 5: FUTURE WORK**

### **Examine Magnetic Properties of CA-Fe<sub>3</sub>O<sub>4</sub> Treated Membranes**

To further determine the functionality of the NP treated nanomembranes the magnetic properties of the samples treated via electrospraying and the grafting method should be measured. This evaluation would be significant to determine if the desired superparamagnetic property can be achieved with the respective NP loadings on the membranes. A vibrating sample magnetometer (VSM) can be used to confirm the superparamagnetic property of the NP treated samples. Si et al's magnetization studies on Fe<sub>3</sub>O<sub>4</sub> carbon membranes revealed that the saturation magnetization of approximately 10 emu/g was suitable to facilitate membrane separation for water treatment applications.<sup>1</sup> Preliminary tests were conducted with the NP treated membranes prepared by the three methods with simple exposure to an external magnet, however, static cling of Nylon 6 made it difficult to confirm magnetization.

### **Confirm Covalent Bonding in Chemical Grafting Reaction**

The actual graft sites on the membrane can be calculated to determine the degree of covalent bonding that can be achieved between the ester activated Fe<sub>3</sub>O<sub>4</sub> NPs and amine end groups of Nylon 6. This can allow us to calculate the surface area per graft site similar to Michielsen's work on Nylon 66 films and compare the distance per particle on FESEM images.<sup>114</sup> Michielsen determined that the surface area per graft site for NY66 is approximately 90 nm<sup>2</sup>.<sup>114</sup> Since NY66 has more grafting sites this suggests that the surface area per graft site of Nylon 6 would be > 90 nm<sup>2</sup>. If we assume there are four nearest neighbors the average distance between NPs would be  $D > \sqrt{90 \text{ nm}^2}$  (> 9.5 nm).

The amount of amine end groups in Nylon 6 can be calculated based on a titration method following the protocol of Wang et al. A Nylon 6 nanomembrane can be dissolved in

70:30 phenol/methanol solvent at room temperature. A 0.02 N HCl solution can be used for the titration with thymol blue as the indicator between pH = 1.2 - 2.8.<sup>115</sup>

It may also be significant to further study the thermal degradation mechanisms between the pristine and chemically treated samples because TGA may provide indirect evidence of chemical bonding. Further studies are needed to determine whether chemical bonding via electrostatic and covalent bonds may allow the polyamide chains to improve their initial thermal stability and whether the NP treatments are affecting the thermal degradation of Nylon 6.

### **Wastewater Treatment Performance & Potential Recyclability/Reuse of Composite Nanomembranes**

A model pollutant, such as a metal ion or a cationic dye, can be selected to evaluate the composite membranes performance. The kinetics of pollutant absorption under varied pH environments and time intervals can be evaluated. These studies would allow us to determine the optimal environment in which adsorption can occur on the composite nanomembranes. Additionally, since wastewater can be composed of a complex system of compounds it is important to investigate how pollutant adsorption can be affected by additives, such as surfactants or competing anions.<sup>116</sup>

It would be highly desirable to reuse the composite fabrics for water treatment applications. The pollutant adsorption would be pH specific, therefore, the water treatment studies can inform the desorption protocol. Zhang et al suggests recyclability and renewed, high adsorption capabilities of PAA/GO/Fe<sub>3</sub>O<sub>4</sub> NPs is possible by washing adsorbed metals on the materials in a weak acid, such as acetic acid to initiate desorption.<sup>79</sup> Alternative desorption strategies can be used to alter the ionic strength and pH environment of the solution for reuse of the materials.

The electrosprayed and grafted composite membranes prepared in this study revealed low NP release under acidic conditions, which suggests that the NP treatment is most durable under those conditions. The Nylon 6 membrane may begin to degrade under extended exposure to acidic conditions and the adsorption potential of the membrane itself are additional topics to consider.

### **Green Route to NP Synthesis**

A few limitations to the use of superparamagnetic iron oxide NPs in real world applications are the production cost and potential toxicity to aquatic species and humans. Ways to overcome these limitations are to explore the use of naturally abundant waste materials for use during NP synthesis. Food waste materials that are rich in polyphenols are viable capping agents for NPs, which can reduce production costs and toxicity. Hoag et al has demonstrated that spherical, zero-valent iron NPs with a size range of 5 - 15 nm can be synthesized with several iron salts and tea polyphenols.<sup>117</sup> Venkateswarlu et al explored the use of fruit waste material, plantain peels to prepare spherical, ferromagnetic Fe<sub>3</sub>O<sub>4</sub> NPs that were 30 - 50 nm in size.<sup>118</sup> The polyphenols can act both as a reducing agent and capping group, they are water soluble, have low toxicity, and would not produce hazardous waste.<sup>117</sup> These characteristics make polyphenols appealing as an alternative to the use of costly and potentially hazardous nonpolar capping groups typically used in the thermal decomposition, bottom up approach.<sup>3, 101</sup>

For further studies, polyphenols from pecan shells can be extracted to explore the viability of producing Fe<sub>3</sub>O<sub>4</sub> NPs with superparamagnetic properties. The particle size can be affected by the amounts of the solvent, iron salt, polyphenol concentration, and the time allowed for the reaction. It would be intriguing to explore if certain polyphenols in the pecan shells have

greater affinity toward the metal particles. Additionally, to explore the pollutant pick-up potential of these NPs capped with polyphenols.

## CHAPTER 6: REFERENCES

1. Si, Y.; Ren, T.; Ding, B.; Yu, J.; Sun, G., Synthesis of mesoporous magnetic Fe<sub>3</sub>O<sub>4</sub>@carbon nanofibers utilizing in situ polymerized polybenzoxazine for water purification. *Journal of Materials Chemistry* **2012**, *22* (11), 4619-4622.
2. Lee, W. Y.; Cheng, W. Y.; Yeh, Y. C.; Lai, C. H.; Hwang, S. M.; Hsiao, C. W.; Huang, C. W.; Chen, M. C.; Sung, H. W., Magnetically directed self-assembly of electrospun superparamagnetic fibrous bundles to form three-dimensional tissues with a highly ordered architecture. *Tissue Eng Part C Methods* **2011**, *17* (6), 651-61.
3. Hu, H.; Jiang, W.; Lan, F.; Zeng, X.; Ma, S.; Wu, Y.; Gu, Z., Synergic effect of magnetic nanoparticles on the electrospun aligned superparamagnetic nanofibers as a potential tissue engineering scaffold. *RSC Advances* **2013**, *3* (3), 879-886.
4. Wang, L.; Yu, Y.; Chen, P. C.; Zhang, D. W.; Chen, C. H., Electrospinning synthesis of C/Fe<sub>3</sub>O<sub>4</sub> composite nanofibers and their application for high performance lithium-ion batteries. *Journal of Power Sources* **2008**, *183* (2), 717-723.
5. Barrera, C.; Gould, T.; Hyde, K.; Montero, G.; Hinestroza, J. P.; Rinaldi, C., Electrospun magnetic nanofibers with anti-counterfeiting applications. **2005**.
6. Zhu, M. T.; Wang, B.; Wang, Y.; Yuan, L.; Wang, H. J.; Wang, M.; Ouyang, H.; Chai, Z. F.; Feng, W. Y.; Zhao, Y. L., Endothelial dysfunction and inflammation induced by iron oxide nanoparticle exposure: Risk factors for early atherosclerosis. *Toxicol Lett* **2011**, *203* (2), 162-71.
7. Wu, X.; Tan, Y.; Mao, H.; Zhang, M., Toxic effects of iron oxide nanoparticles on human umbilical vein endothelial cells. *Int J Nanomedicine* **2010**, *5*, 385-99.
8. Anton, F., Process and apparatus for preparing artificial threads. Google Patents: 1934; Anton, F., Method and apparatus for spinning. Google Patents: 1944.
9. Darrell, H. R. a. I. C., Nanometre diameter fibres of polymer, produced by electrospinning. *Nanotechnology* **1996**, *7* (3), 216.
10. Reneker, D. H.; Yarin, A. L., Electrospinning jets and polymer nanofibers. *Polymer* **2008**, *49* (10), 2387-2425.
11. Wang, D.; Sun, G.; Chiou, B.-S., A High-Throughput, Controllable, and Environmentally Benign Fabrication Process of Thermoplastic Nanofibers. *Macromolecular Materials and Engineering* **2007**, *292* (4), 407-414.
12. Li, H.; Ke, Y.; Hu, Y., Polymer nanofibers prepared by template melt extrusion. *Journal of Applied Polymer Science* **2006**, *99* (3), 1018-1023.
13. Lyons, J.; Li, C.; Ko, F., Melt-electrospinning part I: processing parameters and geometric properties. *Polymer* **2004**, *45* (22), 7597-7603.
14. Ellison, C. J.; Phatak, A.; Giles, D. W.; Macosko, C. W.; Bates, F. S., Melt blown nanofibers: Fiber diameter distributions and onset of fiber breakup. *Polymer* **2007**, *48* (11), 3306-3316.
15. Liu, R.; Cai, N.; Yang, W.; Chen, W.; Liu, H., Sea-island polyurethane/polycarbonate composite nanofiber fabricated through electrospinning. *Journal of Applied Polymer Science* **2010**, *116* (3), 1313-1321.
16. Kamiyama, M.; Soeda, T.; Nagajima, S.; Tanaka, K., Development and application of high-strength polyester nanofibers. *Polymer Journal* **2012**, *44* (10), 987-994.
17. Badrossamay, M. R.; Mcllwee, H. A.; Goss, J. A.; Parker, K. K., Nanofiber Assembly by Rotary Jet-Spinning. *Nano Letters* **2010**, *10* (6), 2257-2261.
18. Sarkar, K.; Gomez, C.; Zambrano, S.; Ramirez, M.; de Hoyos, E.; Vasquez, H.; Lozano, K., Electrospinning to Forcespinning™. *Materials Today* **2010**, *13* (11), 12-14.
19. Yoon, K.; Hsiao, B. S.; Chu, B., Functional nanofibers for environmental applications. *Journal of Materials Chemistry* **2008**, *18* (44), 5326-5334.

20. Um, I. C.; Fang, D.; Hsiao, B. S.; Okamoto, A.; Chu, B., Electro-Spinning and Electro-Blowing of Hyaluronic Acid. *Biomacromolecules* **2004**, *5* (4), 1428-1436.
21. Theron, S. A.; Yarin, A. L.; Zussman, E.; Kroll, E., Multiple jets in electrospinning: experiment and modeling. *Polymer* **2005**, *46* (9), 2889-2899.
22. Ding, B.; Kimura, E.; Sato, T.; Fujita, S.; Shiratori, S., Fabrication of blend biodegradable nanofibrous nonwoven mats via multi-jet electrospinning. *Polymer* **2004**, *45* (6), 1895-1902.
23. Gorga, N. M. T. a. J. R. B. a. L. I. C. a. R. E., Edge electrospinning for high throughput production of quality nanofibers. *Nanotechnology* **2011**, *22* (34), 345301.
24. Niu, H.; Lin, T., Fiber Generators in Needleless Electrospinning. *Journal of Nanomaterials* **2012**, *2012*, 13.
25. Taylor, G., Disintegration of Water Drops in an Electric Field. *Proceedings of the Royal Society of London. Series A. Mathematical and Physical Sciences* **1964**, *280* (1382), 383-397.
26. Li, D.; Xia, Y., Electrospinning of Nanofibers: Reinventing the Wheel? *Advanced Materials* **2004**, *16* (14), 1151-1170.
27. Zhang, D.; Karki, A. B.; Rutman, D.; Young, D. P.; Wang, A.; Cocke, D.; Ho, T. H.; Guo, Z., Electrospun polyacrylonitrile nanocomposite fibers reinforced with Fe<sub>3</sub>O<sub>4</sub> nanoparticles: Fabrication and property analysis. *Polymer* **2009**, *50* (17), 4189-4198.
28. Sill, T. J.; von Recum, H. A., Electrospinning: Applications in drug delivery and tissue engineering. *Biomaterials* **2008**, *29* (13), 1989-2006.
29. Bin Ding and Chunrong Li and Yasuhiro Miyauchi and Oriha Kuwaki and Seimei, S., Formation of novel 2D polymer nanowebs via electrospinning. *Nanotechnology* **2006**, *17* (15), 3685.
30. Tsou, S.-Y.; Lin, H.-S.; Wang, C., Studies on the electrospun Nylon 6 nanofibers from polyelectrolyte solutions: 1. Effects of solution concentration and temperature. *Polymer* **2011**, *52* (14), 3127-3136.
31. Kara, M. O. P.; Frey, M. W., Effects of solvents on the morphology and conductivity of poly(3,4-ethylenedioxythiophene):Poly(styrenesulfonate) nanofibers. *Journal of Applied Polymer Science* **2014**, *131* (11), n/a-n/a.
32. You, Y.; Lee, S. J.; Min, B.-M.; Park, W. H., Effect of solution properties on nanofibrous structure of electrospun poly(lactic-co-glycolic acid). *Journal of Applied Polymer Science* **2006**, *99* (3), 1214-1221.
33. Joshi, P.; Zhang, L.; Davoux, D.; Zhu, Z.; Galipeau, D.; Fong, H.; Qiao, Q., Composite of TiO<sub>2</sub> nanofibers and nanoparticles for dye-sensitized solar cells with significantly improved efficiency. *Energy & Environmental Science* **2010**, *3* (10), 1507-1510.
34. Sahay, R.; Kumar, P. S.; Sridhar, R.; Sundaramurthy, J.; Venugopal, J.; Mhaisalkar, S. G.; Ramakrishna, S., Electrospun composite nanofibers and their multifaceted applications. *Journal of Materials Chemistry* **2012**, *22* (26), 12953-12971.
35. Xin, J. H.; Daoud, W. A.; Kong, Y. Y., A New Approach to UV-Blocking Treatment for Cotton Fabrics. *Textile Research Journal* **2004**, *74* (2), 97-100.
36. Abidi, N.; Aminayi, P.; Cabrales, L.; Hequet, E., Super-Hydrophobic Cotton Fabric Prepared Using Nanoparticles and Molecular Vapor Deposition Methods. In *Functional Materials from Renewable Sources*, American Chemical Society: 2012; Vol. 1107, pp 149-165.
37. Ye, S.; Zhang, D.; Liu, H.; Zhou, J., ZnO nanocrystallites/cellulose hybrid nanofibers fabricated by electrospinning and solvothermal techniques and their photocatalytic activity. *Journal of Applied Polymer Science* **2011**, *121* (3), 1757-1764.
38. Dixit, V.; Tewari, J. C.; Obendorf, S. K., Identification of degraded products of aldicarb due to the catalytic behavior of titanium dioxide/polyacrylonitrile nanofiber. *Journal of Chromatography A* **2009**, *1216* (36), 6394-6399.
39. Wang, W.; Zhang, L.; Tong, S.; Li, X.; Song, W., Three-dimensional network films of electrospun copper oxide nanofibers for glucose determination. *Biosensors and Bioelectronics* **2009**, *25* (4), 708-714.

40. Xiaofeng Song and Zhaojie Wang and Yongben Liu and Ce Wang and Lijuan, L., A highly sensitive ethanol sensor based on mesoporous ZnO–SnO<sub>2</sub> nanofibers. *Nanotechnology* **2009**, *20* (7), 075501.
41. Ahn, B. W.; Kang, T. J., Preparation and characterization of magnetic nanofibers with iron oxide nanoparticles and poly(ethylene terephthalate). *Journal of Applied Polymer Science* **2012**, *125* (2), 1567-1575.
42. Dominghaus, H., *Plastics for Engineering*. 3rd edition ed.; New York, 1988.
43. Bose, G., *Recherches sur la cause et sur la veritable theorie del'electricite*. Wittenberg, 1745.
44. Zeleny, J., Instability of Electrified Liquid Surfaces. *Physical Review* **1917**, *10* (1), 1-6.
45. Cloupeau, M.; Prunet-Foch, B., Electrostatic spraying of liquids: Main functioning modes. *Journal of Electrostatics* **1990**, *25* (2), 165-184.
46. Rayleigh, L., XX. On the equilibrium of liquid conducting masses charged with electricity. *Philosophical Magazine Series 5* **1882**, *14* (87), 184-186.
47. Rietveld, I. B.; Kobayashi, K.; Yamada, H.; Matsushige, K., Morphology control of poly(vinylidene fluoride) thin film made with electrospray. *Journal of Colloid and Interface Science* **2006**, *298* (2), 639-651.
48. Gupta, D.; Venugopal, J.; Mitra, S.; Giri Dev, V. R.; Ramakrishna, S., Nanostructured biocomposite substrates by electrospinning and electro spraying for the mineralization of osteoblasts. *Biomaterials* **2009**, *30* (11), 2085-2094.
49. Jaworek, A.; Sobczyk, A. T., Electro spraying route to nanotechnology: An overview. *Journal of Electrostatics* **2008**, *66* (3–4), 197-219.
50. Yu, D.-G.; Williams, G. R.; Wang, X.; Liu, X.-K.; Li, H.-L.; Bligh, S. W. A., Dual drug release nanocomposites prepared using a combination of electro spraying and electro spinning. *RSC Advances* **2013**, *3* (14), 4652-4658.
51. Jaworek, A.; Krupa, A.; Lackowski, M.; Sobczyk, A. T.; Czech, T.; Ramakrishna, S.; Sundarrajan, S.; Pliszka, D., Nanocomposite fabric formation by electro spinning and electro spraying technologies. *Journal of Electrostatics* **2009**, *67* (2–3), 435-438.
52. Pliszka, A. J. a. A. K. a. M. L. a. A. T. S. a. T. C. a. S. R. a. S. S. a. D., Electrostatic method for the production of polymer nanofibers blended with metal-oxide nanoparticles. *Journal of Physics: Conference Series* **2009**, *146* (1), 012006.
53. Ariga, K.; Hill, J. P.; Ji, Q., Layer-by-layer assembly as a versatile bottom-up nanofabrication technique for exploratory research and realistic application. *Physical Chemistry Chemical Physics* **2007**, *9* (19), 2319-2340.
54. Decher, G., Polyelectrolyte Multilayers, an Overview. In *Multilayer Thin Films*, Wiley-VCH Verlag GmbH & Co. KGaA: 2003; pp 1-46.
55. Joanny, J.-F.; Castelnovo, M., Polyelectrolyte Adsorption and Multilayer Formation. In *Multilayer Thin Films*, Wiley-VCH Verlag GmbH & Co. KGaA: 2003; pp 87-97.
56. Dobrynin, A. V., Theory and simulations of charged polymers: From solution properties to polymeric nanomaterials. *Current Opinion in Colloid & Interface Science* **2008**, *13* (6), 376-388.
57. Dubas, S. T.; Kumlangdudsana, P.; Potiyaraj, P., Layer-by-layer deposition of antimicrobial silver nanoparticles on textile fibers. *Colloids and Surfaces A: Physicochemical and Engineering Aspects* **2006**, *289* (1–3), 105-109.
58. Park, J. H.; Kim, B. S.; Yoo, Y. C.; Khil, M. S.; Kim, H. Y., Enhanced mechanical properties of multilayer nano-coated electro spun nylon 6 fibers via a layer-by-layer self-assembly. *Journal of Applied Polymer Science* **2008**, *107* (4), 2211-2216.
59. Pieper, J. S.; Hafmans, T.; Veerkamp, J. H.; van Kuppevelt, T. H., Development of tailor-made collagen–glycosaminoglycan matrices: EDC/NHS crosslinking, and ultrastructural aspects. *Biomaterials* **2000**, *21* (6), 581-593.

60. Bartczak, D.; Kanaras, A. G., Preparation of Peptide-Functionalized Gold Nanoparticles Using One Pot EDC/Sulfo-NHS Coupling. *Langmuir* **2011**, *27* (16), 10119-10123.
61. Humphrey, J. M.; Chamberlin, A. R., Chemical Synthesis of Natural Product Peptides: Coupling Methods for the Incorporation of Noncoded Amino Acids into Peptides. *Chemical Reviews* **1997**, *97* (6), 2243-2266.
62. Sapsford, K. E.; Algar, W. R.; Berti, L.; Gemmill, K. B.; Casey, B. J.; Oh, E.; Stewart, M. H.; Medintz, I. L., Functionalizing Nanoparticles with Biological Molecules: Developing Chemistries that Facilitate Nanotechnology. *Chemical Reviews* **2013**, *113* (3), 1904-2074.
63. Nakajima, N.; Ikada, Y., Mechanism of Amide Formation by Carbodiimide for Bioconjugation in Aqueous Media. *Bioconjugate Chemistry* **1995**, *6* (1), 123-130.
64. Orelma, H.; Filpponen, I.; Johansson, L. S.; Osterberg, M.; Rojas, O. J.; Laine, J., Surface functionalized nanofibrillar cellulose (NFC) film as a platform for immunoassays and diagnostics. *Biointerphases* **2012**, *7* (1-4), 61.
65. Tobiesen, F. A.; Michielsen, S., Method for grafting poly(acrylic acid) onto nylon 6,6 using amine end groups on nylon surface. *Journal of Polymer Science Part A: Polymer Chemistry* **2002**, *40* (5), 719-728.
66. Benn, T. M.; Westerhoff, P., Nanoparticle Silver Released into Water from Commercially Available Sock Fabrics. *Environmental Science & Technology* **2008**, *42* (11), 4133-4139.
67. Geranio, L.; Heuberger, M.; Nowack, B., The Behavior of Silver Nanotextiles during Washing. *Environmental Science & Technology* **2009**, *43* (21), 8113-8118.
68. Ritchie, S. M. C.; Bhattacharyya, D., Membrane-based hybrid processes for high water recovery and selective inorganic pollutant separation. *Journal of Hazardous Materials* **2002**, *92* (1), 21-32.
69. Dąbrowski, A.; Hubicki, Z.; Podkościelny, P.; Robens, E., Selective removal of the heavy metal ions from waters and industrial wastewaters by ion-exchange method. *Chemosphere* **2004**, *56* (2), 91-106.
70. Ögütveren, Ü. B.; Koparal, S., Color removal from textile effluents by electrochemical destruction. *Journal of Environmental Science and Health . Part A: Environmental Science and Engineering and Toxicology* **1994**, *29* (1), 1-16.
71. Grimm, J.; Bessarabov, D.; Sanderson, R., Review of electro-assisted methods for water purification. *Desalination* **1998**, *115* (3), 285-294.
72. Wan Ngah, W. S.; Teong, L. C.; Hanafiah, M. A. K. M., Adsorption of dyes and heavy metal ions by chitosan composites: A review. *Carbohydrate Polymers* **2011**, *83* (4), 1446-1456.
73. Kyzas, G. Z.; Deliyanni, E. A.; Matis, K. A., Graphene oxide and its application as an adsorbent for wastewater treatment. *Journal of Chemical Technology & Biotechnology* **2014**, *89* (2), 196-205.
74. O'Hern, S. C.; Boutilier, M. S. H.; Idrobo, J.-C.; Song, Y.; Kong, J.; Laoui, T.; Atieh, M.; Karnik, R., Selective Ionic Transport through Tunable Subnanometer Pores in Single-Layer Graphene Membranes. *Nano Letters* **2014**, *14* (3), 1234-1241.
75. Qu, X.; Alvarez, P. J. J.; Li, Q., Applications of nanotechnology in water and wastewater treatment. *Water Research* **2013**, *47* (12), 3931-3946.
76. Zeng, G.; Pang, Y.; Zeng, Z.; Tang, L.; Zhang, Y.; Liu, Y.; Zhang, J.; Lei, X.; Li, Z.; Xiong, Y.; Xie, G., Removal and Recovery of Zn<sup>2+</sup> and Pb<sup>2+</sup> by Imine-Functionalized Magnetic Nanoparticles with Tunable Selectivity. *Langmuir* **2011**, *28* (1), 468-473.
77. Shin, S.; Jang, J., Thiol containing polymer encapsulated magnetic nanoparticles as reusable and efficiently separable adsorbent for heavy metal ions. *Chemical Communications* **2007**, (41), 4230-4232.
78. Guo, L.; Li, J.; Zhang, L.; Li, J.; Li, Y.; Yu, C.; Shi, J.; Ruan, M.; Feng, J., A facile route to synthesize magnetic particles within hollow mesoporous spheres and their performance as separable Hg<sup>2+</sup> adsorbents. *Journal of Materials Chemistry* **2008**, *18* (23), 2733-2738.

79. Zhang, W.; Shi, X.; Zhang, Y.; Gu, W.; Li, B.; Xian, Y., Synthesis of water-soluble magnetic graphene nanocomposites for recyclable removal of heavy metal ions. *Journal of Materials Chemistry A* **2013**, *1* (5), 1745-1753.
80. Liu, J.; Du, X., Fast removal of aqueous Hg(II) with quaternary ammonium-functionalized magnetic mesoporous silica and silica regeneration. *Journal of Materials Chemistry* **2011**, *21* (19), 6981-6987.
81. Cornell, R. M.; Schwertmann, U., Electronic, Electrical and Magnetic Properties and Colour. In *The Iron Oxides*, Wiley-VCH Verlag GmbH & Co. KGaA: 2004; pp 111-137.
82. Cornell, R. M.; Schwertmann, U., Characterization. In *The Iron Oxides*, Wiley-VCH Verlag GmbH & Co. KGaA: 2004; pp 139-183.
83. Egerton, R., *Physical Principles of Electron Microscopy: An Introduction to TEM, SEM, and AEM* 1st ed.; Springer: New York, 2005; p 202.
84. Butt, H. J.; Graf, K.; Kappl, M., *Physics and chemistry interfaces*. Wiley-VCH: Weinheim, Germany, 2003; p 361.
85. Wang, Z. L., Transmission Electron Microscopy of Shape-Controlled Nanocrystals and Their Assemblies. *The Journal of Physical Chemistry B* **2000**, *104* (6), 1153-1175.
86. Williams, D. B.; Barry Carter, C., *Transmission Electron Microscopy: A Textbook for Material Science*. 2nd ed.; Springer: New York, 2009; p 760.
87. Kalantar-zadeh, K.; Fry, B., *Nanotechnology-Enabled Sensors*. Springer: 2008; p 492.
88. Color Handbook. <http://www.specialchem4coatings.com/tc/color-handbook/index.aspx> (accessed June 7, 2014).
89. Ding, B.; Wang, X.; Yu, J.; Wang, M., Polyamide 6 composite nano-fiber/net functionalized by polyethyleneimine on quartz crystal microbalance for highly sensitive formaldehyde sensors. *Journal of Materials Chemistry* **2011**, *21* (34), 12784-12792.
90. Pant, H. R.; Bajgai, M. P.; Yi, C.; Nirmala, R.; Nam, K. T.; Baek, W.-i.; Kim, H. Y., Effect of successive electrospinning and the strength of hydrogen bond on the morphology of electrospun nylon-6 nanofibers. *Colloids and Surfaces A: Physicochemical and Engineering Aspects* **2010**, *370* (1-3), 87-94.
91. Wang, X.; Ding, B.; Sun, G.; Wang, M.; Yu, J., Electro-spinning/netting: A strategy for the fabrication of three-dimensional polymer nano-fiber/nets. *Progress in Materials Science* **2013**, *58* (8), 1173-1243.
92. Andradý, A. L., *Science and technology of polymer nanofibers*. Wiley: Hoboken, N.J., 2008.
93. Carmen Bautista, M.; Bomati-Miguel, O.; del Puerto Morales, M.; Serna, C. J.; Veintemillas-Verdaguer, S., Surface characterisation of dextran-coated iron oxide nanoparticles prepared by laser pyrolysis and coprecipitation. *Journal of Magnetism and Magnetic Materials* **2005**, *293* (1), 20-27.
94. Guo, Z.; Henry, L. L.; Palshin, V.; Podlaha, E. J., Synthesis of poly(methyl methacrylate) stabilized colloidal zero-valence metallic nanoparticles. *Journal of Materials Chemistry* **2006**, *16* (18), 1772-1777.
95. Guan, X.-h.; Chen, G.-h.; Shang, C., ATR-FTIR and XPS study on the structure of complexes formed upon the adsorption of simple organic acids on aluminum hydroxide. *Journal of Environmental Sciences* **2007**, *19* (4), 438-443.
96. Waldron, R. D., Infrared Spectra of Ferrites. *Physical Review* **1955**, *99* (6), 1727-1735.
97. Yu, B. Y.; Kwak, S.-Y., Assembly of magnetite nanocrystals into spherical mesoporous aggregates with a 3-D wormhole-like pore structure. *Journal of Materials Chemistry* **2010**, *20* (38), 8320-8328.
98. Robinson, D. B.; Persson, H. H. J.; Zeng, H.; Li, G.; Pourmand, N.; Sun, S.; Wang, S. X., DNA-Functionalized MFe<sub>2</sub>O<sub>4</sub> (M = Fe, Co, or Mn) Nanoparticles and Their Hybridization to DNA-Functionalized Surfaces. *Langmuir* **2005**, *21* (7), 3096-3103.
99. Sun, Z.; Deitzel, J. M.; Knopf, J.; Chen, X.; Gillespie, J. W., The effect of solvent dielectric properties on the collection of oriented electrospun fibers. *Journal of Applied Polymer Science* **2012**, *125* (4), 2585-2594.

100. Smallwood, I. M., Handbook of Organic Solvent Properties. Elsevier.
101. Murray, C. B.; Kagan, C. R.; Bawendi, M. G., SYNTHESIS AND CHARACTERIZATION OF MONODISPERSE NANOCRYSTALS AND CLOSE-PACKED NANOCRYSTAL ASSEMBLIES. *Annual Review of Materials Science* **2000**, *30* (1), 545-610.
102. Wang, Y.; Herron, N., Nanometer-sized semiconductor clusters: materials synthesis, quantum size effects, and photophysical properties. *The Journal of Physical Chemistry* **1991**, *95* (2), 525-532.
103. Richert, L.; Lavallo, P.; Payan, E.; Shu, X. Z.; Prestwich, G. D.; Stoltz, J.-F.; Schaaf, P.; Voegel, J.-C.; Picart, C., Layer by Layer Buildup of Polysaccharide Films: Physical Chemistry and Cellular Adhesion Aspects. *Langmuir* **2003**, *20* (2), 448-458.
104. Lavallo, P.; Gergely, C.; Cuisinier, F. J. G.; Decher, G.; Schaaf, P.; Voegel, J. C.; Picart, C., Comparison of the Structure of Polyelectrolyte Multilayer Films Exhibiting a Linear and an Exponential Growth Regime: An in Situ Atomic Force Microscopy Study. *Macromolecules* **2002**, *35* (11), 4458-4465.
105. Elbakry, A.; Wurster, E.-C.; Zaky, A.; Liebl, R.; Schindler, E.; Bauer-Kreisel, P.; Blunk, T.; Rachel, R.; Goepferich, A.; Breunig, M., Layer-by-Layer Coated Gold Nanoparticles: Size-Dependent Delivery of DNA into Cells. *Small* **2012**, *8* (24), 3847-3856.
106. Zhou, J.; Pishko, M. V.; Lutkenhaus, J. L., Thermoresponsive Layer-by-Layer Assemblies for Nanoparticle-Based Drug Delivery. *Langmuir* **2014**, *30* (20), 5903-5910.
107. Erogbogbo, F.; Tien, C.-A.; Chang, C.-W.; Yong, K.-T.; Law, W.-C.; Ding, H.; Roy, I.; Swihart, M. T.; Prasad, P. N., Bioconjugation of Luminescent Silicon Quantum Dots for Selective Uptake by Cancer Cells. *Bioconjugate Chemistry* **2011**, *22* (6), 1081-1088.
108. Abu-Much, R.; Meridor, U.; Frydman, A.; Gedanken, A., Formation of a Three-Dimensional Microstructure of Fe<sub>3</sub>O<sub>4</sub>-Poly(vinyl alcohol) Composite by Evaporating the Hydrosol under a Magnetic Field. *The Journal of Physical Chemistry B* **2006**, *110* (16), 8194-8203.
109. Dunn, P.; Sansom, G. F., The stress cracking of polyamides by metal salts. Part I. Metal halides. *Journal of Applied Polymer Science* **1969**, *13* (8), 1641-1655.
110. Chao, L.-C.; Chang, E.-P., Interaction of anhydrous ferric chloride with nylon 6. *Journal of Applied Polymer Science* **1981**, *26* (2), 603-610.
111. Cai, Y.; Huang, F.; Wei, Q.; Wu, E.; Gao, W., Surface functionalization, morphology and thermal properties of polyamide6/O-MMT composite nanofibers by Fe<sub>2</sub>O<sub>3</sub> sputter coating. *Applied Surface Science* **2008**, *254* (17), 5501-5505.
112. Liu, J.; Hu, Y.; Wang, S.; Song, L.; Chen, Z.; Fan, W., Preparation and characterization of nylon 6/Cu<sup>2+</sup>-exchanged and Fe<sup>3+</sup>-exchanged montmorillonite nanocomposite. *Colloid and Polymer Science* **2004**, *282* (3), 291-294.
113. Allen, N. S.; Harrison, M. J.; Ledward, M.; Follows, G. W., Thermal and photo-chemical degradation of nylon 6,6 polymer: Part III—Influence of iron and metal deactivators. *Polymer Degradation and Stability* **1989**, *23* (2), 165-174.
114. Michielsen, S., The effect of grafted polymeric lubricant molecular weight on the frictional characteristics of nylon 6,6 fibers. *Journal of Applied Polymer Science* **1999**, *73* (1), 129-136.
115. Wang, H.-H.; Wang, C.-C., Dyeing mechanism and model of nylon 6 fiber dyeing in low-temperature hydrogen peroxide-glyoxal redox system. *Journal of Applied Polymer Science* **2006**, *100* (5), 4197-4207.
116. Kanel, S. R.; Manning, B.; Charlet, L.; Choi, H., Removal of Arsenic(III) from Groundwater by Nanoscale Zero-Valent Iron. *Environmental Science & Technology* **2005**, *39* (5), 1291-1298.
117. Hoag, G. E.; Collins, J. B.; Holcomb, J. L.; Hoag, J. R.; Nadagouda, M. N.; Varma, R. S., Degradation of bromothymol blue by 'greener' nano-scale zero-valent iron synthesized using tea polyphenols. *Journal of Materials Chemistry* **2009**, *19* (45), 8671-8677.
118. Venkateswarlu, S.; Rao, Y. S.; Balaji, T.; Prathima, B.; Jyothi, N. V. V., Biogenic synthesis of Fe<sub>3</sub>O<sub>4</sub> magnetic nanoparticles using plantain peel extract. *Materials Letters* **2013**, *100* (0), 241-244.

## CHAPTER 7: APPENDIX

### Upscaled Electrospinning System – Before and After

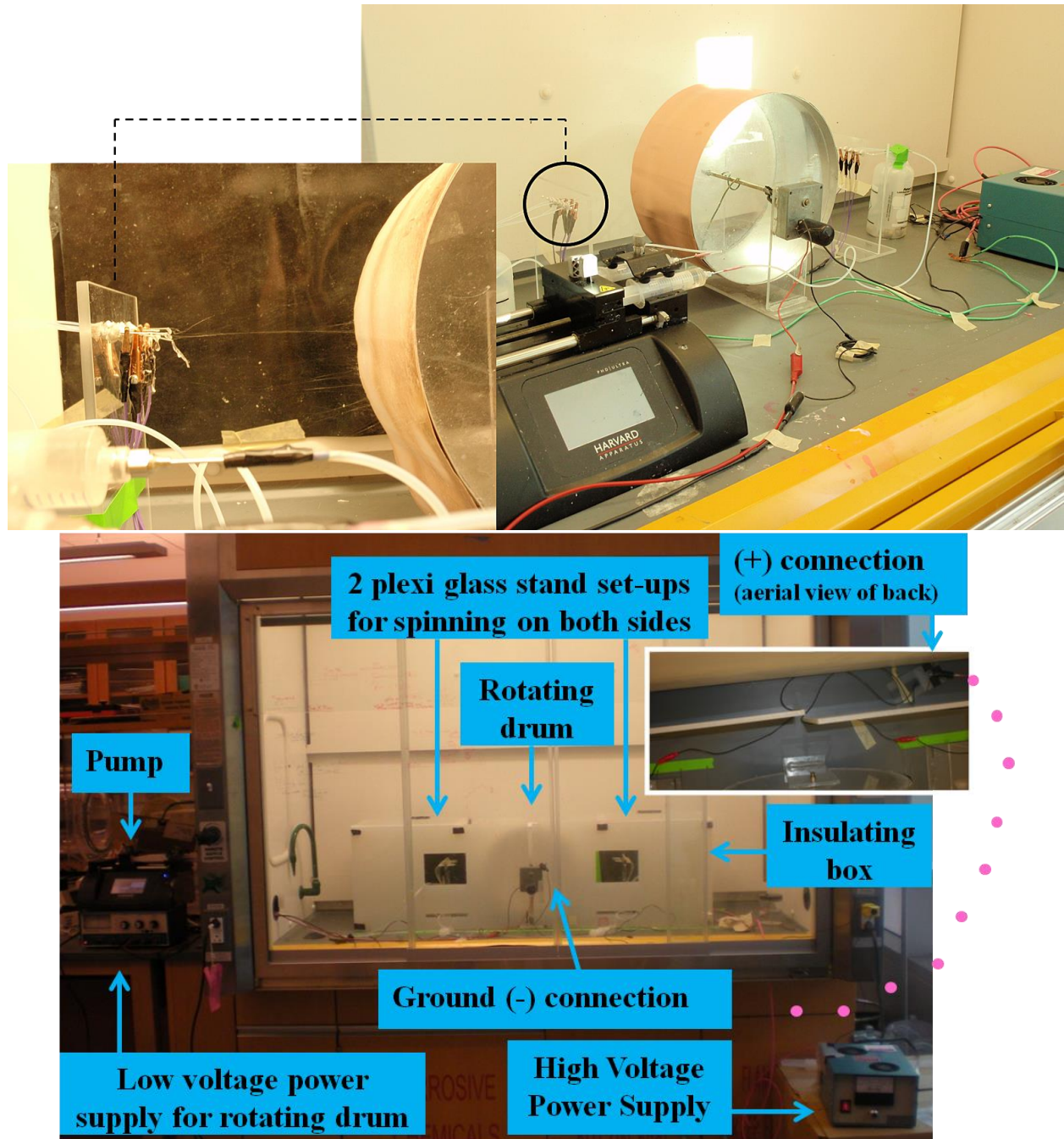


Figure 7.1 Photograph of electrospinning system in Frey lab before adjustments (top) and after (bottom)

## Additional Grafting Reaction Data

### FTIR Data

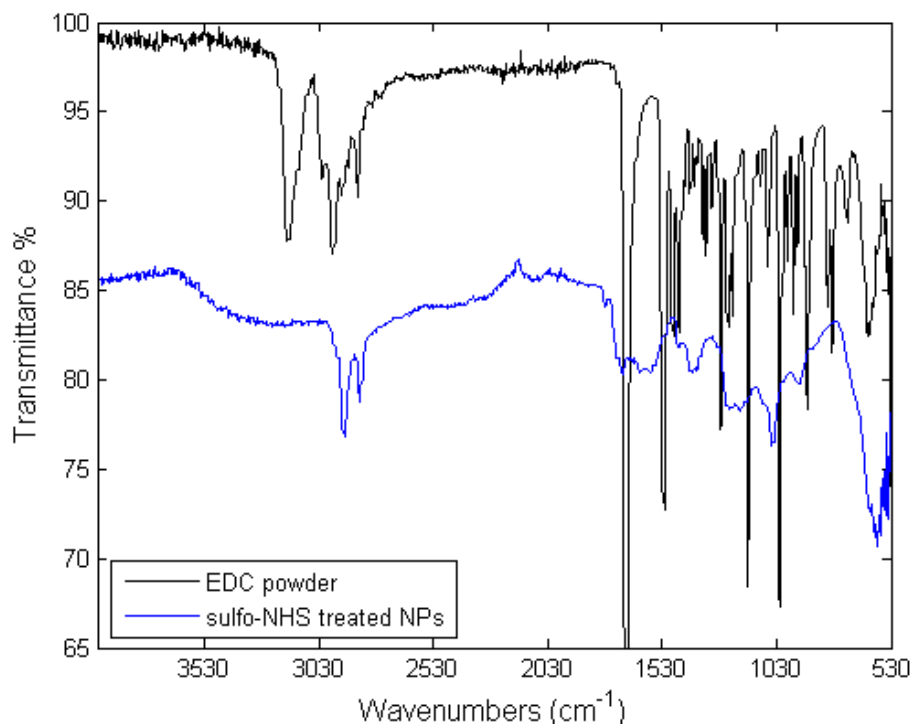


Figure 7.2 ATR-FTIR spectra of pristine EDC powder/ester-activated NPs

### XPS Data

A control sample of CA-Fe<sub>3</sub>O<sub>4</sub> NPs and a sulfo-NHS activated CA-Fe<sub>3</sub>O<sub>4</sub> NP sample were examined with XPS in attempt to confirm the formation of an ester bond between the NPs and sulfo-NHS (Figure 7.3). However, the data for the sulfo-NHS activated CA-Fe<sub>3</sub>O<sub>4</sub> NPs did not display the distinct Fe, N, or S peaks belonging to sulfo-NHS NPs. This suggests that XPS was unable to detect the elements in the sample at that concentration.

XPS samples were analyzed with a monochromatic AlK- $\alpha$  X-ray (1486. eV) source, an operating pressure of  $2 \times 10^{-9}$  Torr, and a beam diameter of 1 mm (Surface Science Instruments SSX-100). The take-off angle was of 35° (emission angle of 55°) and the penetration depth was approximately 10 nm. Wide survey scans were collected from 0 to 1200 eV. A hemispherical

analyzer determined electron kinetic energy with a pass energy of 150 V for wide/survey scans and 50 V for high resolution scans. A flood gun was used for charge neutralization of insulating samples. The data was edited with CasaXPS software. The NP samples were drop cast onto carbon tape.

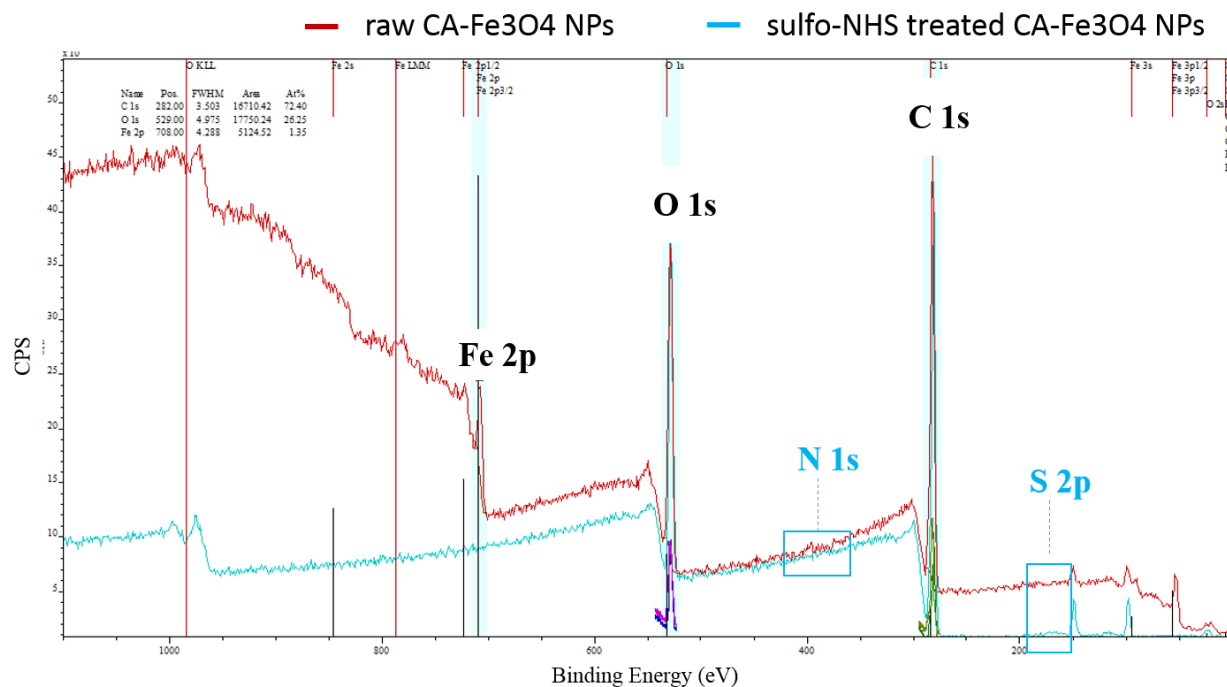


**Figure 7.3 XPS spectra of nanoparticle drop cast samples**

Nanomembranes treated via the grafting reaction were also analyzed via XPS. 3 wt% NP membranes displayed Fe peaks under more vigorous experimental conditions. The reaction between the activated NPs and Nylon 6 occurred for 24 hrs and in a buffer of higher ionic strength (250 mM, pH = 8) (Figure 7.4). The NPs were detectable due to significant agglomeration on the fiber surface and no C1s or N1s chemical shifts were detected that could confirm covalent bonding in the high resolution scan.

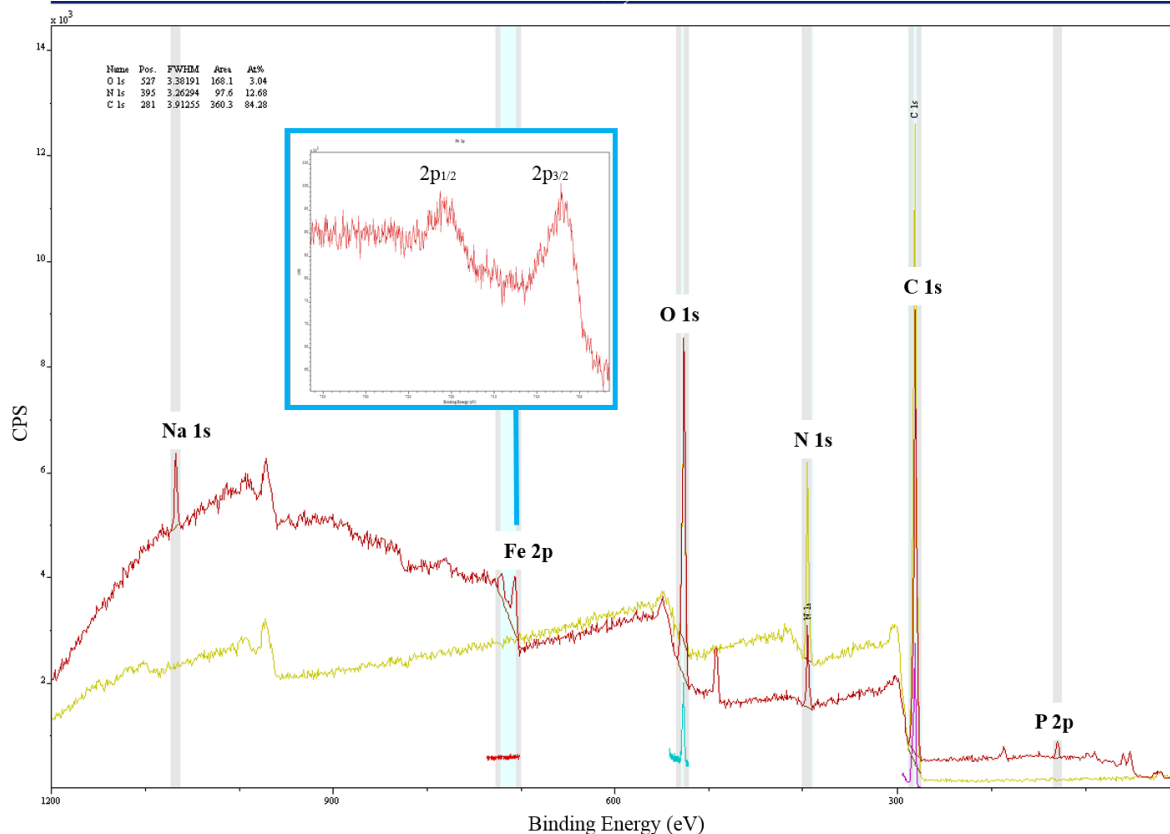


**Figure 7.4 XPS spectra of Nylon 6 nanomembranes treated via the grafting method for extended time**

Tobiesen et al used XPS to confirm covalent bonding with NY66 films, but it may not work well for nanofibers because they are not anatomically smooth samples and the structural conformation of colloidal NPs the polymer functionalization Tobiesen studied differ greatly.

### *Fiber Morphology*

A SEM image of a representative sample displays high NP agglomeration and competing chemical affinity such as ionic and hydrogen bonding (Figure 7.5).

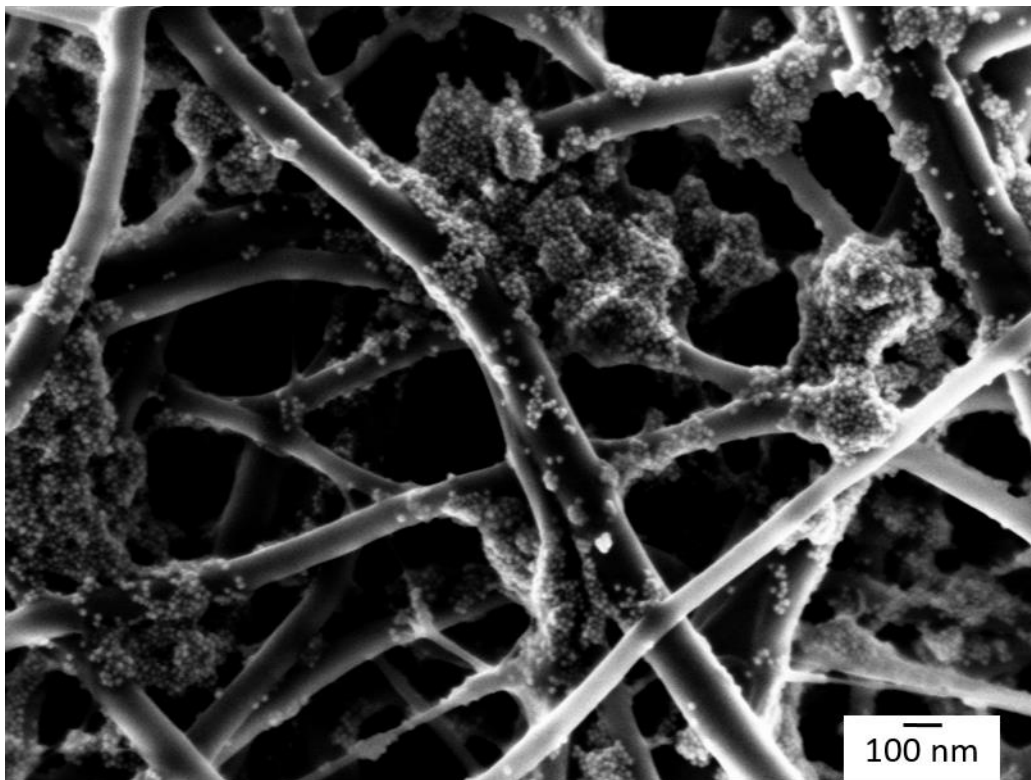


Figure 7.5 FESEM image of representative fiber morphology/NP distribution by grafting conditions

### CIELAB Values for Post-Washed Membranes

Table 7.1 Color coordinates of post-washed electrospayed, LbL, and grafted membranes

Treatment	Sample	L*	a*	b*	$\Delta L^*$	$\Delta a^*$	$\Delta b^*$
Electrospayed	Pristine NY6	96.584	-0.250	-0.0915	n/a	n/a	n/a
	Area I	91.106	0.267	6.528	-5.478	0.517	6.6195
	Area II	91.952	-0.266	6.042	-4.632	-0.016	6.1335
LbL	Area I	91.811	0.576	4.137	-4.773	0.826	4.2285
	Area II	94.335	0.057	2.024	-2.249	0.307	2.1155
Grafted	Area I	88.165	1.304	8.378	-8.419	1.554	8.4695
	Area II	89.130	1.117	7.905	-7.454	1.367	7.9965

### CIELAB Measurement Standards

Table 7.2 displays CIELAB values of Pantone color cards (blue, red, yellow, green) with values that correspond to the 3D color coordinate system. The Princess Blue card helped confirm the level of precision and reproducibility of values provided by the ColorEye spectrophotometer to the tenths place for comparative analysis.

**Table 7.2 CIELAB values of Pantone color cards**

<b>Pantone Color</b>	<b>L*</b>	<b>a*</b>	<b>b*</b>
Princess Blue	60.628	-1.022	-17.791
Haute Red	59.475	17.822	8.689
Solar Power	83.210	5.900	38.119
Hunter Green	60.280	-6.558	4.140